UNIVERSITY OF CAPE TOWN
IYUNIVESITHI YASEKAPA • UNIVERSITEIT VAN KAAPSTAD

The impact of submesoscales on the stratification dynamics in the Southern Ocean

Marcel David du Plessis

Thesis submitted for the degree of Doctor of Philosophy

Department of Oceanography
University of Cape Town
South Africa

July 2018

"It always seems impossible until it is done."

Nelson Mandela

Abstract

Submesoscale dynamics $\mathcal{O}$(1-10 km, hours to days) are considered to strongly affect the stratification of the upper ocean. In the Southern Ocean, studies of submesoscale dynamics are biased to regions preconditioned for strong frontal activity and topographical influence. This dissertation considers the role of submesoscales on the evolution of mixed layer depth and upper ocean stratification in the open-ocean Subantarctic Ocean. First, we present autonomous ocean glider measurements from spring to late-summer to show that transient increases in stratification within the mixed layer during spring result in rapid mixed layer shoaling events. A realistically-forced simulation using a one-dimensional mixed layer model fails to explain these observed stratification events. We show that during this time, baroclinic mixed layer instabilities periodically induce a restratification flux of over 1000 W. m^{-2}, suggesting that the unexplained restratification is likely a result of submesoscale flows.

Second, we study four separate years of seasonal-length (mid-winter to late-summer) glider experiments to define how submesoscale flows may induce inter-annual variations in the onset of spring/summer mixed layer restratification. Sustained temporal increases of stratification above the winter mixed layer, which defines the onset of seasonal restratification, can differ by up to 28 days between the four years studied. To explain this discrepancy, equivalent heat fluxes of baroclinic mixed layer instabilities (restratification) and Ekman buoyancy flux (restratification or mixing) are parameterized into a one-dimensional mixed layer model. Simulations including the parameterizations reveal a seasonal evolution of mixed layer stratification which is significantly more comparable to the glider observations than model simulations using heat and freshwater fluxes alone. Furthermore, the parameterization dramatically improves the sub-seasonal variability of mixed layer stratification, particularly during the onset of seasonal restratification when the mixed layer remains deep despite a positive surface heat flux.

Following this, we characterize the full seasonal cycle of submesoscale flows using

a realistically-forced 1/36° NEMO simulation of the Atlantic Southern Ocean. We show that deep winter mixed layers enhance the upper ocean available potential energy, which through the release of baroclinic mixed layer instabilities drive increased vertical buoyancy flux and potential to kinetic energy. These processes are associated with strong vertical velocities within the mixed layer characterized by large instantaneous upwelling and downwelling fluxes at the location of fronts. The insights from the glider observations propose that baroclinic mixed layer instabilities lead to increased near surface restratification in winter to spring, but are regulated by the synoptic-scale increases in Ekman buoyancy flux, which can keep the mixed layer deep for up to a month after surface warming. We propose the balance between restratification by baroclinic mixed layer instabilities and strong Ekman buoyancy flux driven by the passing of Southern Ocean storms is key in setting the large inter-annual variations of seasonal mixed layer restratification in the Subantarctic Ocean.

Finally, we constrain the ability of gliders to represent regional submesoscale dynamics to provide context to current observations and inform future field work operations. Virtual gliders simulated within the 1/36° simulation show that horizontal buoyancy gradients in the Subantarctic are largely isotropic. We show that increasing the number of gliders sampling simultaneously over one month from one to a swarm of six results in improving the representation of the total distribution of horizontal buoyancy gradients across the Subantarctic from 10% to 42%. Similarly, by having a single glider sampling for six consecutive months, the distribution of horizontal buoyancy gradients observed increases to 47% of the total distribution.

The insights presented in this dissertation enhance our understanding of submesoscale flows in the open-ocean Southern Ocean. These results are likely to have direct implications for physical and biological processes related to the ocean's role on climate.

Supervisors

Assoc. Prof. Sebastiaan Swart

Department of Marine Sciences, University of Gothenburg, Sweden

Assoc. Prof. Isabelle Ansorge

Department of Oceanography, University of Cape Town, South Africa

Dr. Amala Mahadevan

Physical Oceanography, Massachusetts Institute of Technology/Woods Hole Oceanographic Institute, United States

Funding

Financial support for this study has been attained from the following sources:

- South African National Antarctic Programme (NRF) grant of S. Swart (SNA14071475720).
- Department of Science and Technology grant of CSIR-SOCCO.
- South African National Antarctic Programme (NRF) grant of I.J. Anosrge (South Atlantic Meridional Overturning Circulation).
- Wallenberg Academy Fellowship of S. Swart (WAF 2015.0186) for four research visits to the University of Gothenburg, Sweden.
- Guest studenships at Woods Hole Oceanographic Institute through A. Mahadevan for two research visits to WHOI, United States.
- The South African ocean glider program is supported by the Department of Science and Technology through the Sustainability and Innovation in Southern Ocean Observational Infrastructure grant of P.M.S. Monteiro and S. Swart.

Declaration

I declare that this thesis is my own unaided work, both in concept and execution, and that apart from the normal guidance from my supervisors, I have received no assistance except as acknowledged. I declare that none of the work included in this thesis has been submitted in the past, or is being, or is to be submitted for a degree at this University or at any other. Chapter 3 of this manuscript has been published in *Journal of Geophysical Research: Oceans*. I confirm that this above declaration holds true for this publication too, and authorship of my three supervisors represents their assistance with improving style and grammar and advice in managing the paper through the peer-review process.

Inclusion of Publication

I confirm that I have been granted permission by the University of Cape Town's Doctoral Degrees Board to include the following publication in my PhD thesis, and where co-authorships are involved, my co-authors have agreed that I may include the publication:

du Plessis, M, Swart, S, Ansorge I.J. and Mahadevan A. (2017) Submesoscale processes promote seasonal restratification in the Subantarctic Ocean. *J. Geophys. Res.* 122(4).

Signed by candidate

Marcel David du Plessis Date: 11/07/2018

Student number: DPLMAR020

Acknowledgements

I would like to thank Associate Professor Isabelle Ansorge for the never ending support to travel and broaden my scientific horizons as well as the countless opportunities presented to me beyond my PhD. Any student would be lucky to have your support, thank you. To Amala Mahadevan, thank you for welcoming me into your research group during my three visits to Woods Hole and for all your mentorship over the past 5 years. I have learned so much from you and your group. Seb and Gualtiero, thanks for looking out for me during my time on the east coast.

I would like to thank some people who have helped me along the way. To Andy Thompson, for the scientific discussions and sharing your knowledge with me. To Pedro Monteiro, for the opportunity to be part of a wonderful research group. To those at the Southern Ocean Carbon and Climate Observatory, Sandy, Tommy, Luke, Sarah, Nicollete, Emma, Marjo et al. thanks for the great company along the way. I am grateful to Luke and Sarah for always lending an ear and willing to share your scientific knowledge. I want to mention Nicollete Chang for all the help regarding the access and running of the model data in this thesis, your help has been instrumental.

I want to give thanks to the University of Gothenbug for hosting me during four seperate visits totalling about half a year. My visits to GU have been a catalyst for my PhD and I am grateful for that. To the Polar Gliders (Swart Lab) group at GU, Seb, Louise, Iss and Martin, I am lucky to be a part of research group with such enjoyable people. I look forward to many more insightful discussions and research visits to Bornö in the future.

I would like to extent an appreciation to the Barking Toads, running with you guys has been a huge stress relief for me and I look forward to many more hours in your company somewhere in the mountains, see you in Addo.

To my family, Mom, Dad and Rox, your support for me over my life has been instrumental in giving me the tools to do this PhD. Thank you for always being there for me and providing the motivation to help me succeed. I could not ask for any more,

thank you.

To my supervisor and friend, Seb Swart. This has been an unforgettable journey. The opportunities you have provided to me are those any PhD student would grab in a moment. But more than that, you have become a friend, welcoming me into your home when you had no need to, making my trips to Sweden a home away from home. Thank you for the continuous emotional support and providing perspective to life outside of science, I am better for that. Kate, Josh, thank you for allowing me into your family and adopting me as a brother, it is a privilege to watch the naughty rat growing up.

Jen, I am blessed to have your love and support. Thank you for taking an interest in my work and always lending an ear. Your understanding and patience for all my travels and late nights over the course of my PhD is not unnoticed. I have enjoyed many of life's milestones with you and it is these events that make me most happy, this is another step along that road and I look forward to what is to come.

M.d.P.

Contents

List of Figures

List of Tables

CHAPTER 1

Introduction

Since the 18th century, the concentration of carbon dioxide (CO_2) in the atmosphere has risen from 280 ppm to over 400 ppm (Le Quéré et al., 2016). This has been attributed to the increase in anthropogenic carbon in the atmosphere via industrial sources and is the primary contributor to climate change. The oceans have played, and continue to play a major role in mitigating climate change by storing large amounts of heat and carbon (Sabine et al., 2004; Khatiwala et al., 2009). The reservoir of inorganic carbon in the ocean is about 50 times that of the atmosphere. It is estimated that the ocean is responsible for absorbing over 30% of the total CO_2 released into the atmosphere by anthropogenic sources (Sabine et al., 2004). Therefore, small changes in the ocean reservoir can lead to potentially important impacts in the atmospheric concentrations.

The oceanic mixed layer is defined here as the volume of water residing from the ocean surface downward, which has uniform properties of density. The mixed layer is a turbulent environment which varies across a range of scales from the millimeter to over 1000 km. As such, the evolution of the mixed layer can be affected by a wide range of mechanisms (Brainerd and Gregg, 1995; Hosegood et al., 2008; Taylor and Ferrari, 2009; Sallée et al., 2010b; Thomas et al., 2015). Air-sea exchange of gases occur between the mixed layer and above and is, therefore, an important precursor for the storage of carbon and heat in the oceans. It serves as the medium through which heat, momentum, and gases (such as CO_2) are exchanged between the atmosphere and the ocean. Therefore, we require an accurate understanding of the processes which drive mixed layer variability to understand the how the ocean and atmosphere interact.

1.1 The Southern Ocean mixed layer

The Southern Ocean mixed layer is a particularly important component of the Earth's climate system. Strong winds coupled with atmospheric cooling enhance turbulent mixing which deepens the mixed layer (Dong et al., 2008). The deep mixed layers of the Southern Ocean can reach beyond 500 m depth, which connects the atmosphere to Antarctic Intermediate Water (AAIW) and Subantarctic Mode Water (SAMW) formation

(Hanawa and Talley, 2001). This process connects the upper and lower limbs of the global overturning circulation (Sloyan and Rintoul, 2001). The subsequent capping of the mixed layer closes the connection between the atmosphere and the deeper water masses. By this formation mechanism, SAMW and AAIW carry the characteristics of air-sea interactions and CO_2 from the surface to the ocean interior. In particular, the formation of these water masses is considered a strong indicator of anthropogenic climate change (Banks et al., 2002; Sabine et al., 2004). Therefore, deep mixing in the Southern Ocean has significant ramnifications for long-term climate signals. On shorter time scales, the evolution of the mixed layer directly influences biogeochemical phenomena (Thomalla et al., 2011; Taylor and Ferrari, 2011) through the availability of light and nutrients to support phytoplankton growth. In particular, primary production in the Southern Ocean is responsible for a third of the global organic carbon flux (Schlitzer, 2002). The prediction of climate on seasonal, decadal, and longer timescales, therefore, requires accurate knowledge of the dynamics which impact the evolution of the mixed layer.

1.1.1 Dominant mode of variability: the seasonal cycle

From Argo floats, we are now able to resolve the large-scale structure, and seasonality of the Southern Ocean mixed layer depth (MLD) (Dong et al., 2008). The seasonal cycle is considered the dominant mode of variability, accounting for 88% of the variance (Sallée et al., 2010a). The deepest mixed layers occur north of the Antarctic Circumpolar Current (ACC) during August/September and the shallowest during January/February (Figure 1.1). The seasonal range of the MLD is large, reaching around 500 m at the deepest locations during winter before shallowing to around 100 m in summer. Simply, the deep mixed layers are a response to surface cooling which provides a convective mixing within the mixed layer as well as strong winds which erode the stratification at the mixed layer base (Dong et al., 2008). A circumpolar view of a monthly MLD climatology for summer (Figure 1.1a) and winter (1.1b) reveals seasonal differences in MLDs for the Indian, Atlantic and Pacific basins. Zonal asymmetry exists during

winter, where MLDs are shallower by approximately 200 m in the Atlantic basin. This is due to zonal departures in the Southern Annular Mode (SAM) that generate anomalies in heat flux and explain the observed zonal asymmetry (Sallée et al., 2010b). The limited SAMW formation in the Atlantic is one of the main reasons the MLD dynamics of this region has received relatively less attention than the Pacific and Indian.

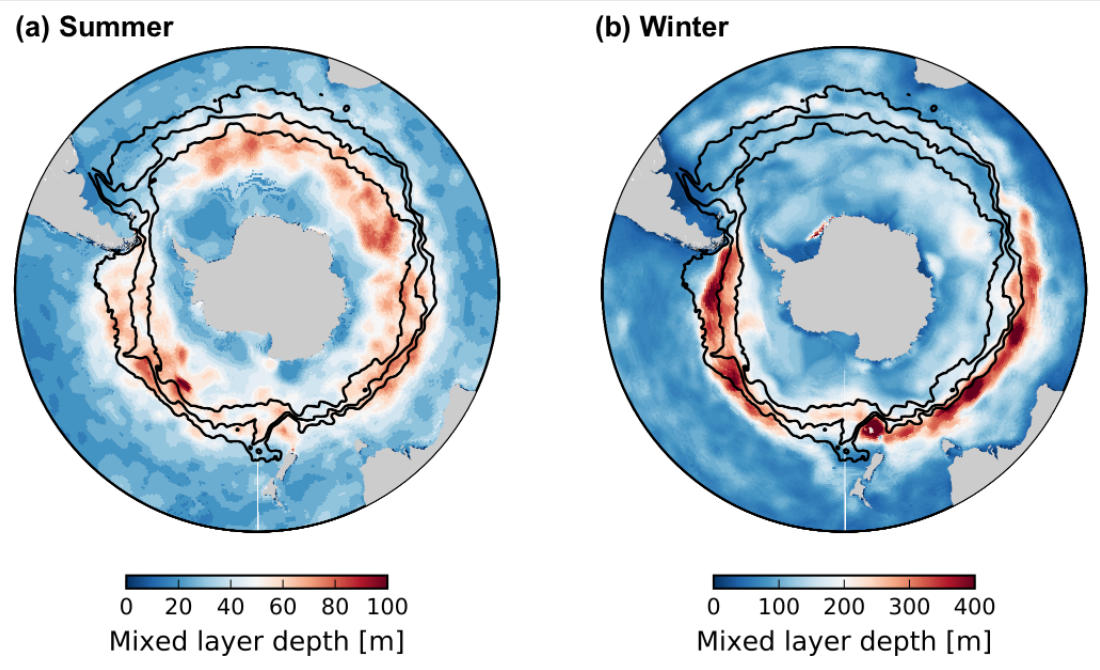

Figure 1.1: (a) Summer (January) and (b) winter (September) mean mixed layer depth for the Southern Ocean. Data is a climatology using CTD profiles from Argo floats, Ice Tethered Profilers and shipboard data (Schmidtko et al., 2013).

1.1.2 Southern Ocean fronts

The Southern Ocean is dominated by the eastward flowing ACC driven by large-scale wind forcing, buoyancy forcing, and the interaction of eddies with the mean flow, which transports 137 ± 9 *Sv* south of Africa (Rintoul et al., 2001; Cunningham et al., 2003; Swart and Speich, 2010). This flow is primarily constrained by five major frontal boundaries characterized by deep-reaching eastward flowing geostrophic jets (Gille,

1994; Orsi et al., 1995; Sokolov and Rintoul, 2007). These jets are often referred to as fronts, which include the Subtropical Front (STF), Subantarctic Front (SAF), Antarctic Polar Front (APF), Southern ACC Front (sACCf) and the Southern Boundary of the ACC (SBdy). The STF is circumpolarly non-continuous as it is broken at the Drake Passage and occasionally south of Africa. Zonal asymmetry exists in the latitudinal location of the fronts due to topographical steering, such as at the Kerguelen (80 °E) and Campell Plateaus (175 °E).

A key aspect in understanding the dynamics of the ACC is the role of mesoscale eddies. Intense westerly winds drive an equatorward Ekman flow known as the Deacon cell (Hogg et al., 2008; Abernathey et al., 2011; Langlais et al., 2015), which leads to instabilities that maintain high levels of eddy activity in the Southern Ocean. These eddies are mesoscale in size $\mathcal{O}$(100 km) which transport heat poleward across the zonal axis of the ACC (Marshall and Speer, 2012). Meredith and Hogg (2006) show that the mesoscale poleward moving eddies compensate for the equatorward Ekman flow by revealing an increase in the eddy kinetic energy in response to an increase in the wind stress.

1.1.3 The Subantarctic Zone

The Subantarctic Zone (SAZ) is the region which resides between the STF and SAF. The SAZ acts as a transitional zone between the subtropical domain and the core jet of the ACC being the SAF. The characteristics of the SAZ mixed layer is influenced from both the northern and southern boundaries, where a poleward progression of intense mesoscale activity from the subtropical domain leads to the diffusion of warmer and saltier into the mixed layer. Sallée et al. (2008) propose that a warming of the SAZ mixed layer through diffusion of subtropical waters south of Africa contributes to the relatively shallow winter mixed layers in the Atlantic basin of the Southern Ocean. In particular, Dencausse et al. (2011) show that the turbulent mesoscale action allows the STF boundary south of Africa to be porous compared to the other longitudes. The southern boundary of the SAZ is largely density-compensated and characterized by an

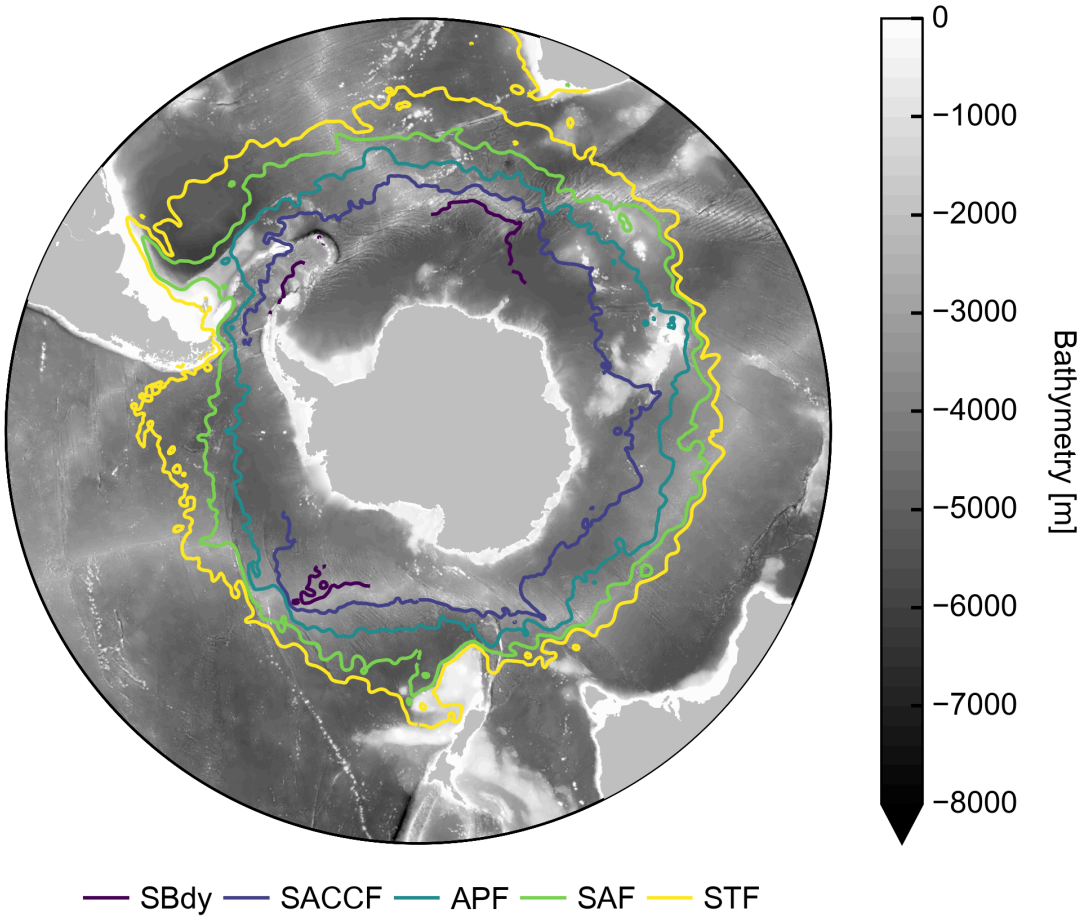

Figure 1.2: Antarctic Circumpolar Current frontal positions as defined by AVISO absolute dynamic topography (ADT) in Swart et al. (2010). Gray shading shows the ETOPO bathymetry (m). Fronts from north to south are as follows: Subtropical Front (STF), Subantarctic Front (SAF), Antarctic Polar Front (APF), Southern ACC Front (SACCF) and the Southern Boundary of the ACC (SBdy). Note the SBdy is spatially omitted as the ADT signal is likely affected by the presence of sea ice.

equatorward inflow of colder and fresher Antarctic Surface Water via an Ekman-driven flow (Faure et al., 2011). The contrasting inflow across the northern and southern boundaries of the SAZ, therefore, are likely to set up large horizontal gradients physical properties within the mixed layer.

1.1.4 Bio-physical interactions in the Subantarctic

Warming of the surface ocean during the summer months increases the vertical stratification of the water column. The associated shallowing of the mixed layer leads to rapid growth of phytoplankton due to the alleviation of light limitation (Arrigo et al., 1998, 2008; Thomalla et al., 2011). Phytoplankton blooms in the Southern Ocean are limited by iron limitation and are thus quickly eroded in early summer (Tagliabue et al., 2014). However, in the SAZ, chlorophyll concentrations are sustained into late summer, as sub-seasonal mixing by storms is a proposed mechanism which generates a vertical supply of iron into the euphotic zone (Swart et al., 2015). Nicholson et al. (2016) propose this impact of storm mixing increases net primary production by up to 60%. This has crucial implications for CO_2 uptake in the Southern Ocean. The seasonal cycle is one of the strongest modes of variability in the SAZ, coupling ecosystem responses physical forcing mechanisms (Monteiro et al., 2011). Thomalla et al. (2011) show that large regions of the Southern Ocean, including the SAZ, are associated with heterogeneous spatio-temporal distribution of seasonal biomass production (Figure 1.3) where the seasonal onset of phytoplankton blooms exhibit large inter-annual variability.

There is increasing evidence that processes occurring at fine spatial (meso- to submesoscales) and temporal (sub-seasonal) scales play an important role in bio-physical interactions. In particular, submesoscale features (baroclinic instabilities from enhanced horizontal buoyancy density gradients) have been shown to account for up to 50% of the variance observed in primary production estimates (Lévy et al., 2001, 2012). Satellites are an effective way to observe the spatial gradients of chlorophyll concentration. A surface chlorophyll image from the MODIS satellite with a spatial resolution of approximately 1 km displays localized fronts and eddies ranging from 10 - 100 km. These eddies contain frontal filaments a few km's in size (Figure 1.4). The figure demonstrates patchiness in elevated chlorophyll over a range of these meso- to submesoscales scales. Taylor and Ferrari (2011) indicate that enhanced stratification in regions of strong fronts can lead to elevated chlorophyll concentrations, while

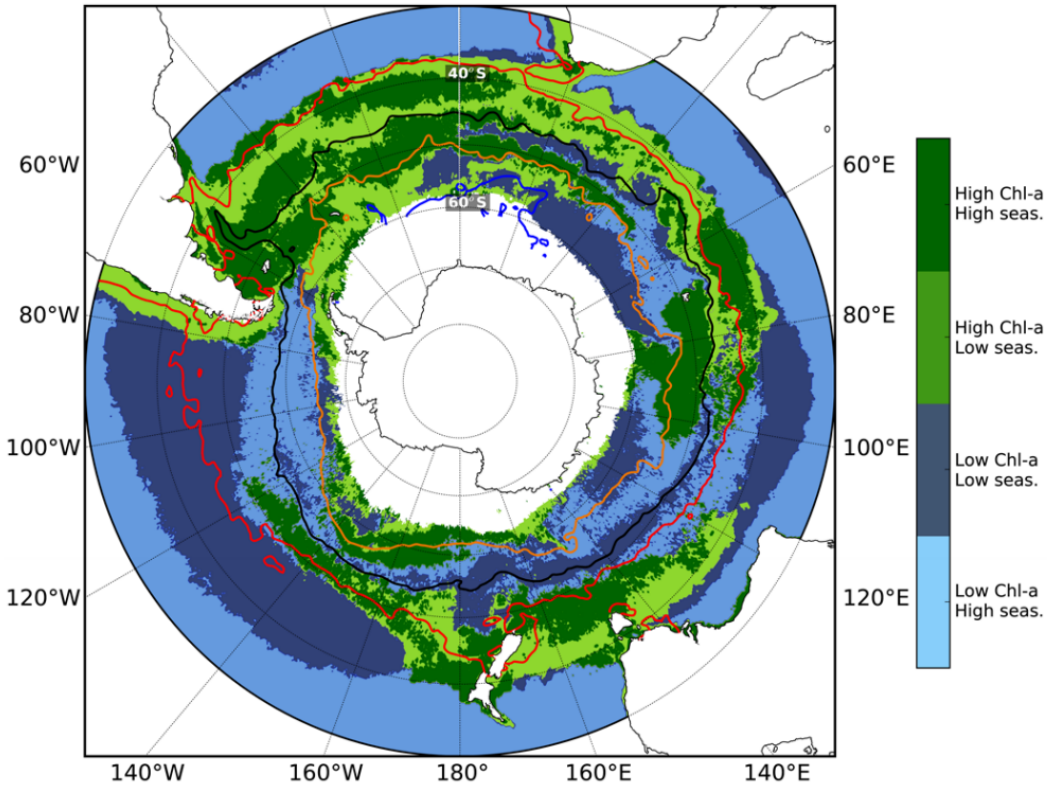

Figure 1.3: Seasonal cycle reproducibility of chlorophyll biomass from Thomalla et al., 2011. Seasonal reproducibility is calculated as the correlation between the mean annual seasonal cycle and the observed chlorophyll time series. A correlation of 0.4 distinguishes between regions of high and low seasonality, while a threshold of 0.25 mg. m^{-3} distinguishes between low or high chlorophyll. Black lines indicate the Southern Ocean fronts.

Mahadevan et al. (2012) show that submesoscale eddy-induced restratification can drive a shallowing of the mixed layer and lead a favorable light environment. Little et al. (2018) demonstrate from a study within the SAZ that patichness in the sea surface temperature (SST) and chlorophyll concentration are primarily driven by submesoscale ocean physics, while Swart et al. (2015) link periods of elevated mixed layer chlorophyll to meso- to submesoscale features during early spring in the SAZ. This thesis is an effort to expand our knowledge and understanding of the fine-scale physics (namely submesoscales) occurring within the mixed layer in the SAZ region of the Southern

Ocean.

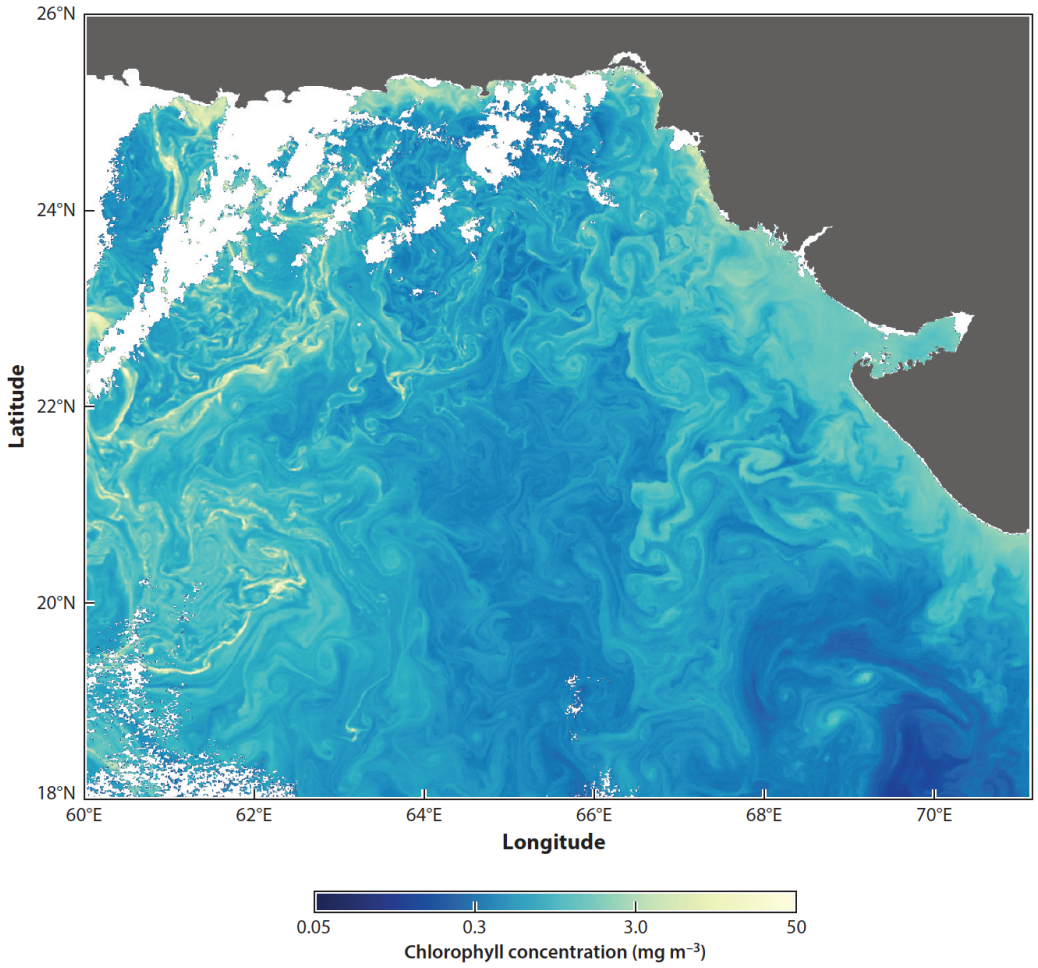

Figure 1.4: Sea surface chlorophyll concentration in the Arabian Sea on February 22, 2005. Image was acquired by the Moderate Resolution Imaging Spectroradiometer (MODIS) from NASA's Aqua satellite, with an approximate resolution of the data is 1 km. White spaces are where data were flagged or missing because of cloud cover. Figure obtained from Mahadevan (2016).

1.2 Meso- and submesoscale dynamics

Mesoscale flows are relatively well understood and can easily be detected from satellite observations (Figure 1.5, Stammer, 1997). Flows occurring within these scales are

associated with horizontal velocities $\mathcal{O}(0.1\ \text{m s}^{-1})$. The Southern Ocean is rich in mesoscale activity generated by instabilities in the baroclinic and barotropic frontal flows (Chelton et al., 1998). These mesoscale structures are characterized by strong frontal jets and sharp horizontal buoyancy fronts at horizontal scales $\mathcal{O}(100\ \text{km})$, which stir around the large-scale buoyancy field. Mesoscale eddies are considered to be in geostrophic balance so that the pressure gradient across the frontal flow is in balance with the Coriolis force. These mesoscale eddies are key to meridional heat and tracer transport (Dufour et al., 2015).

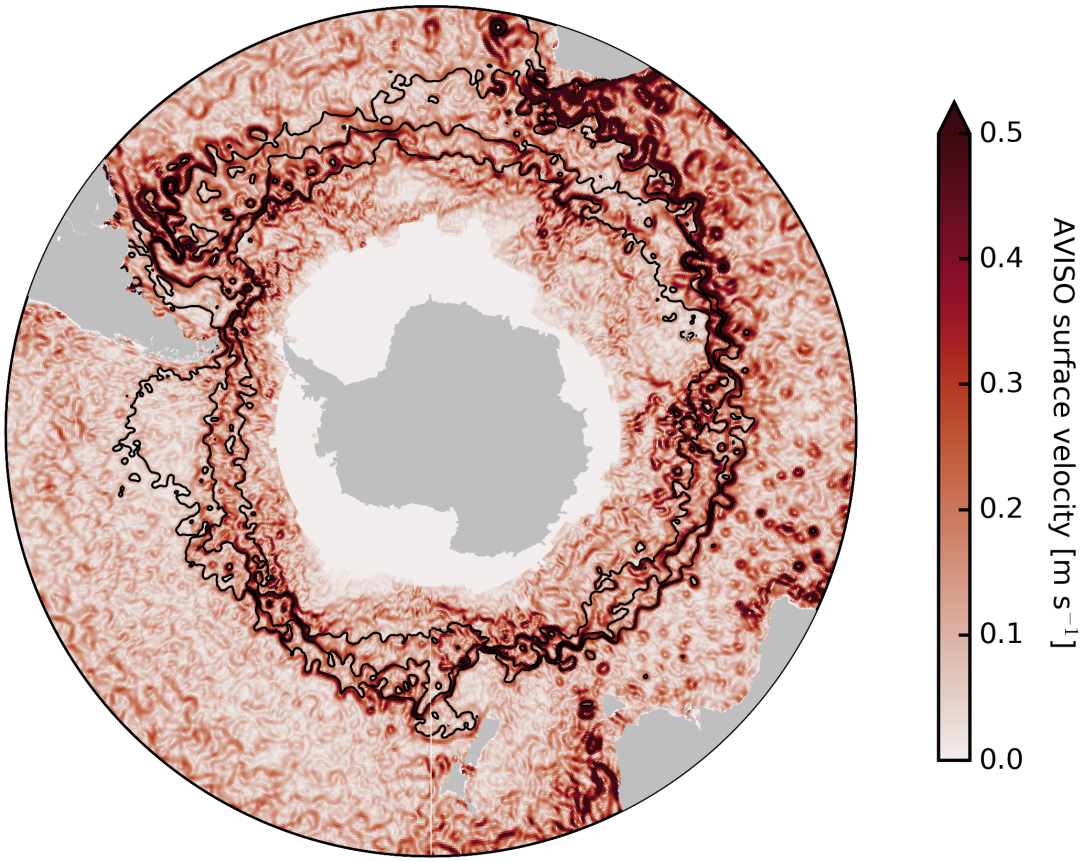

Figure 1.5: Snapshot of the AVISO geostrophic surface velocity field (m s^{-1}) for the Southern Ocean on August 8, 2015. Image has an approximate horizontal resolution of 0.25°. Black lines indicate the Subtropical, Subantarcic and Antarctic Polar Fronts as in Figure 1.2.

However, a potentially important and less understood class of dynamics is the

submesoscale. Submesoscale flows have spatial scales of $\mathcal{O}$(1 - 10 km) and evolve over timescales of hours to days. Submesoscale flow differs from the mesoscale due to the straining of the weak planetary buoyancy gradient and are expected to be significantly ageostrophic. This thesis will focus on the development of submesoscale fronts, which refers to the processes that have smaller length scales than the mixed layer Rossby radius of deformation $L = NH/f$. Submesoscale processes preferentially develop within the mixed layer, and thus N is the mixed layer buoyancy frequency, and H is the MLD. L generally scales at 1 km in the mid-latitude oceans (Thomas et al., 2008). Dynamically, submesoscale flows are characterized by a relative vorticity which is normalized by the planetary vorticity, such that the Rossby number $Ro = |\zeta|/f > 1$. $\zeta = v_x - u_y$, where u and v are the horizontal velocity and x and y are the spatial distance (subscripts denote differentials). If a bulk Rossby number is introduced $Ro_b = U/fL$, where U is the characteristic velocity, then a mixed layer of 100 m and $f = 10^{-4}$ s^{-1} would require a horizontal velocity of 0.1 m. s^{-1} for the flow to be susceptible to ageostrophic effects.

About 70% of the global energy input into the ocean by wind occurs in the Southern Ocean (Wunsch, 1998), which provides the main energy source for the general ocean circulation. The associated kinetic energy (KE) is contained in the eddy fluxes created by baroclinic and barotropic instabilities of this flow. These eddies undergo an inverse cascade of energy as the turbulence within the mesoscale eddies are strongly constrained by the Coriolis force. Therefore, other routes to dissipation are required to balance the energy input by winds. This indicates the enormous importance of the Southern Ocean in the general circulation energy budget. A large component of this energy dissipation happens at the ocean bottom by flow over rough, small-scale topography (Nikurashin et al., 2012). However, recent work indicates that submesoscale overturning instabilities at ocean fronts of scale L can drive an energy cascade from the mesoscale down to dissipation scales (Molemaker et al., 2010; Ferrari, 2011; D'Asaro et al., 2011).

1.3 Submesoscale generation

Mechanisms that energize submesoscale flows and are thus involved in the cascade of energy occur at narrow horizontal currents with strong horizontal buoyancy gradients. These include frontogenesis (Hoskins and Bretherton, 1972), baroclinic mixed layer instability (Molemaker et al., 2005; Boccaletti et al., 2007); and forced motion, such as flows affected by friction at boundaries (Thomas and Lee, 2005). These mechanisms are explored within the analysis of this thesis.

1.3.1 Baroclinic instability

Baroclinic mixed layer instability (MLI) is an ageostrophic instability whereby a stratified flow in thermal wind balance becomes horizontally sheared as to have a strong rotation with a horizontal buoyancy gradient. In the ocean, stable stratification under the influence of the Earth's rotation drives a balanced flow. MLIs lead to a loss of balance of the geostrophic flow, which drives a forward cascade of energy (Molemaker et al., 2005). Boccaletti et al. (2007) show that a baroclinic instability arises at the Rossby radius L, results in swirling eddies the size of 1-10 km which are termed mixed layer eddies (MLE) as in Mahadevan et al. (2012). A photographic example of MLEs off the northern coast of Africa is illustrated in Figure 1.6. A large motivation for studying MLI is that at localized regions where Ro approaches 1, vertical velocities are $\mathcal{O}$(100 m d^{-1}) (Lapeyre and Klein, 2006; Capet et al., 2008b). These are typically an order of magnitude larger than the vertical velocities associated with the mesoscale. Owing to the large vertical velocities, submesoscale processes can transfer properties and tracers vertically between the mixed layer and the ocean interior. This vertical transport is an important process in determining phytoplankton production by supplying nutrients to the euphotic zone as well as the vertical exchange of gases, such as CO_2 and the exchange of properties between the air-sea interface. MLIs arise when the Ro and $Ri = N^2 \,/\, |U_z|^2$ are $\mathcal{O}(1)$. This instability is the geostrophic mode instability of Molemaker et al. (2005) and corresponds to the Eady mode for large values of Ro. The Eady

model was described by Eady (1949) as a prototype to quasi-geostrophic baroclinic instabilities. Stone (1966) used this work to study ageostrophic instabilities which set the foundation for the Fox-Kemper et al. (2008) parameterization of MLEs.

Figure 1.6: Fully developed spirals in the Mediterranean off the coast of Egypt. These are characteristic of horizontal shear associated with baroclinic instability. Picture photographed by P. Scully-Power on 7 October 1984 during Mission STS41-G (Scully-Power, 1986). Location 32 °N, 26 °E. Spiraling eddies have a characteristic length scale of about 6 km (Munk et al., 2000).

In the Southern Ocean, large-scale horizontal buoyancy gradients across ACC are therefore a reservoir of APE which through MLIs can be released into KE. Weak

stratification and large horizontal buoyancy gradients across the strong eastward flowing ACC are conditioned for MLIs susceptible to a large vertical tracer flux $\overline{w\prime c\prime}$, where w is the vertical velocity and c is the tracer concentration. The overbar denotes an average and the primes denote the deviation about the average. MLI has a vertical buoyancy flux denoted $\overline{w\prime b\prime}$, where b is the buoyancy ($b = -g\ (\rho - \rho_0)/\rho_0$) which satisfies $\overline{w\prime b\prime} > 0$. $\overline{w\prime b\prime}$ is the circulation of an ageostrophic secondary circulation (ASC) cell, upward on the lighter side of the front and downward on the denser side, with connecting opposite-sign horizontal flows in the upper and lower parts of the surface layer.

1.3.2 Ekman buoyancy flux

In an Arctic expedition in 1893, F. Nansen allowed his ship, the *Fram*, to freeze into the pack and drift to determine how the currents impact the movement of the ice. Nansen noticed that the direction of drift of the ice and the ship were consistently at an angle to the right of the wind. He spoke with his colleague V. Bjerknes who arranged for his student, V. W. Ekman, to investigate the problem. Ekman produced a preliminary solution in a matter of hours, where he took into account the assumption of a constant turbulent vertical eddy viscosity. The results of his work are known today as the 'Ekman spiral.' The key characteristic of the Ekman spiral is that the net transport is to the left of the wind in the Southern Hemisphere, and to the right in the Northern Hemisphere. In the case that the winds are aligned with the direction of the geostrophic front, a cross-frontal transport occurs. In much of the ocean and indeed the Southern Ocean, the winds are mainly directed in the same direction as the frontal flow. This case is called down-front, while winds aligned against the direction of the flow are known as up-front winds. The effect of down and up-front winds is to destratify and restratify the ocean, respectively (Thomas and Ferrari, 2008). The cross-front advection of density during down-front winds advects dense water over light water. At these fronts, the Ekman advection will lead to gravitational instability which drives an ASC (Thomas, 2005). Thomas and Lee (2005) define this as a surface

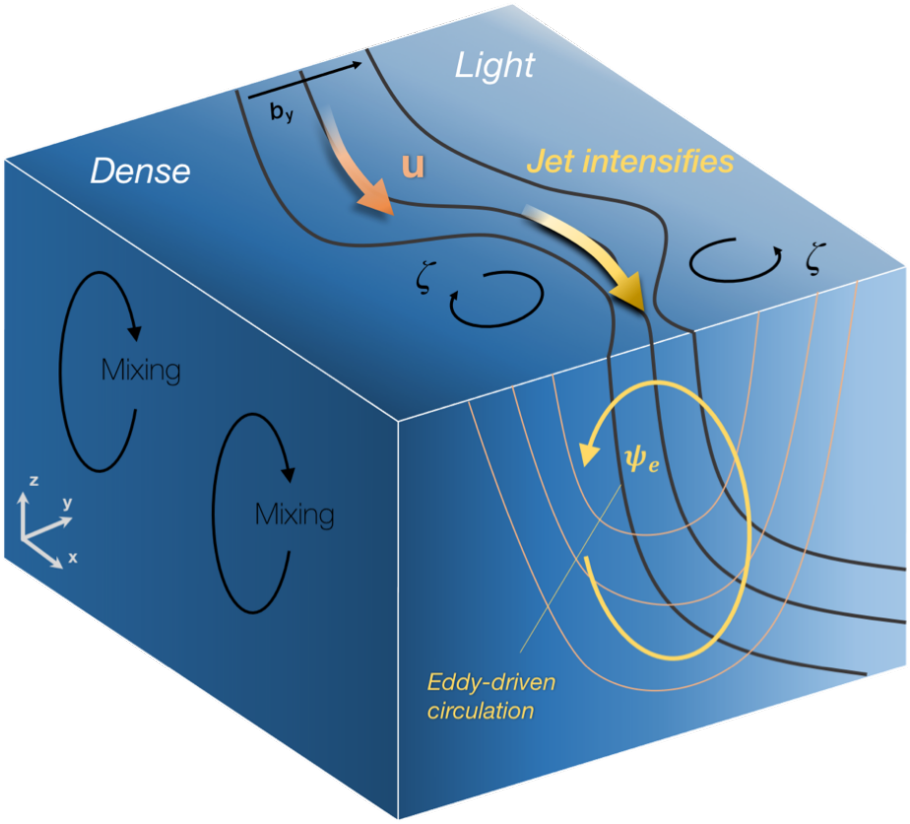

Figure 1.7: Schematic of an upper-ocean front, showing isopycnals (black lines) separating dense water from light water. The flow is ageostrophic, as indicated by u, due to the onset of baroclinic instability, which causes it to meander and lose geostrophic balance. An ASC indicated by ψ_e acts to restore balance by upwelling on the light side of the front and downwelling on the dense side. The vertical motion induced by the ageostrophic overturning circulation changes horizontal gradients of buoyancy to vertical gradients. The vertical motion becomes particularly large when the magnitude of the vorticity ζ associated with the front is $\mathcal{O}(f)$.

adiabatic flux called Ekman buoyancy flux (EBF). The strength of EBF is set by the magnitude of the horizontal buoyancy gradient of the front and the strength of the along-front component of the wind stress. The ACC is subject to powerful wind stress blowing mostly in the direction of the geostrophic currents, yielding large, positive kinetic energy input (Oort et al., 1994). Rintoul and England (2002) found that surface heat and freshwater fluxes alone are not able to explain the temperature and salinity variations of the SAZ and that a direct correlation between enhanced

meridional Ekman transport and cooler and fresher waters exist. They indicate that these cooler and fresher waters in the SAZ have been advected equatorward across the SAF boundary. It is important to note that EBF is not the only mixing term competing against restratification. Surface wave processes such as Langmuir turbulence enhance small-scale vertical mixing and transport, where Hamlington et al. (2014) indicate that submesoscale eddies and large-scale motions are weakened in the presence of Langmuir turbulence. Taylor and Ferrari (2010) provide evidence that turbulence can be also generated by a symmetric instability of the lateral density gradient, where enhanced mixing can be driven below the depth to which atmospheric forcing can generate mixing. Furthermore, Whitt and Taylor (2017) perform numerical simulations to reveal that persistent and strong mean stratification in the mixed layer occurs during the presence of high winds despite the mean dissipation rate remaining elevated throughout the mixed layer.

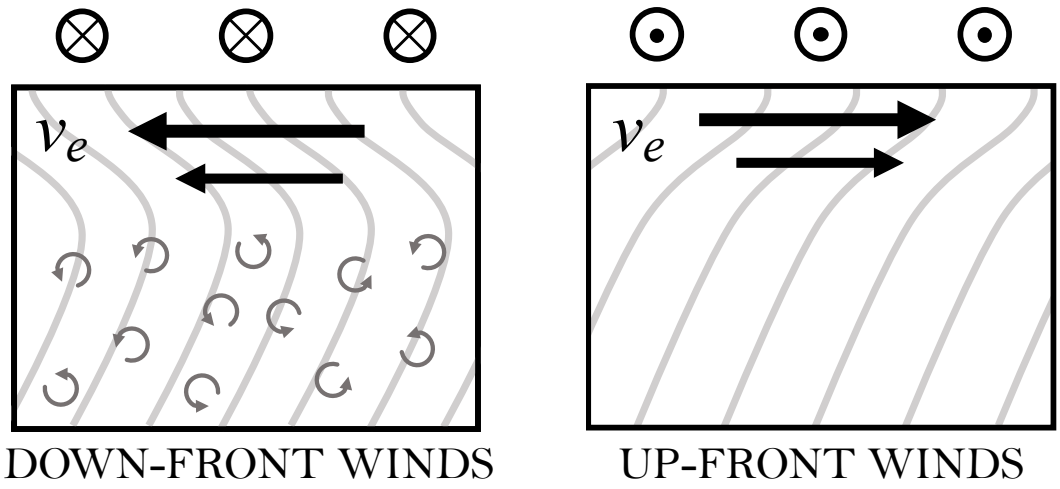

Figure 1.8: Diagram illustrating frictional mixing (left) and restratification (right) at a baroclinic fronts in the upper ocean. Down-front winds (left) blowing along the geostrophic flow will drive an Ekman advection (v_e) that moves denser water over lighter water, setting up convective mixing. Up-front winds restratifies the upper ocean by flattening the isopycnals (gray). Adapted from Thomas and Ferrari (2008).

1.3.3 Frontogenesis

Frontogenesis was first understood by Hoskins and Bretherton (1972) from an atmospheric perspective as the manner in which a confluent geostrophic flow intensifies an initially weak baroclinic zone via its horizontal deformation field. It can be more commonly described as the formation or intensification of a frontal zone (Schulz, 2015), where the measure of the intensity of a front is the horizontal buoyancy gradient. By this definition, frontogenesis is the process which acts to increase the horizontal buoyancy gradients over a given spatial scale. This explains the physical definition of frontogenesis, which can also be expressed in the mathematical framework as the Lagrangian increase in the horizontal buoyancy gradient. A key signature in the identification of frontogenesis is the production of sharp elongated fronts and filaments, which evolve from the large strain from mesoscale eddies and currents. A configuration of the flow at a region of enhanced strain-induced frontogenesis is illustrated in Figure 1.9. The buoyancy gradient is intensified at the surface jet (v) and associated with a current shear along the front (*i.e.* $v_z = b_x / f$). Across the frontal axis is a sub-surface ASC generated by the deformation flow. This is represented as a single overturning cell with upwelling on the light side of the front, and downwelling on the heavier side resulting in a $\overline{w'b'}$ flux. In the Southern Ocean, frontogenesis might represent the confluence of mesoscale eddy circulations. It would be intuitive to think that frontogenesis and MLI will act together in the Southern Ocean to generate submesoscale flows. To separate the two process, MLI is identified as a kinetic energy source, while frontogenesis characterizes the advective evolution towards fronts and filaments. MLI is the baroclinic instability which drives the growth of instabilities in the surface ocean, while frontogenesis characterizes the advective interaction of the MLI deformed flow.

Another key interaction between the atmosphere and the ocean is the impact of wind and waves. Wave generation at more strongly strained fronts has recently been investigated by Shakespeare and Taylor (2013) to show internal waves are generated

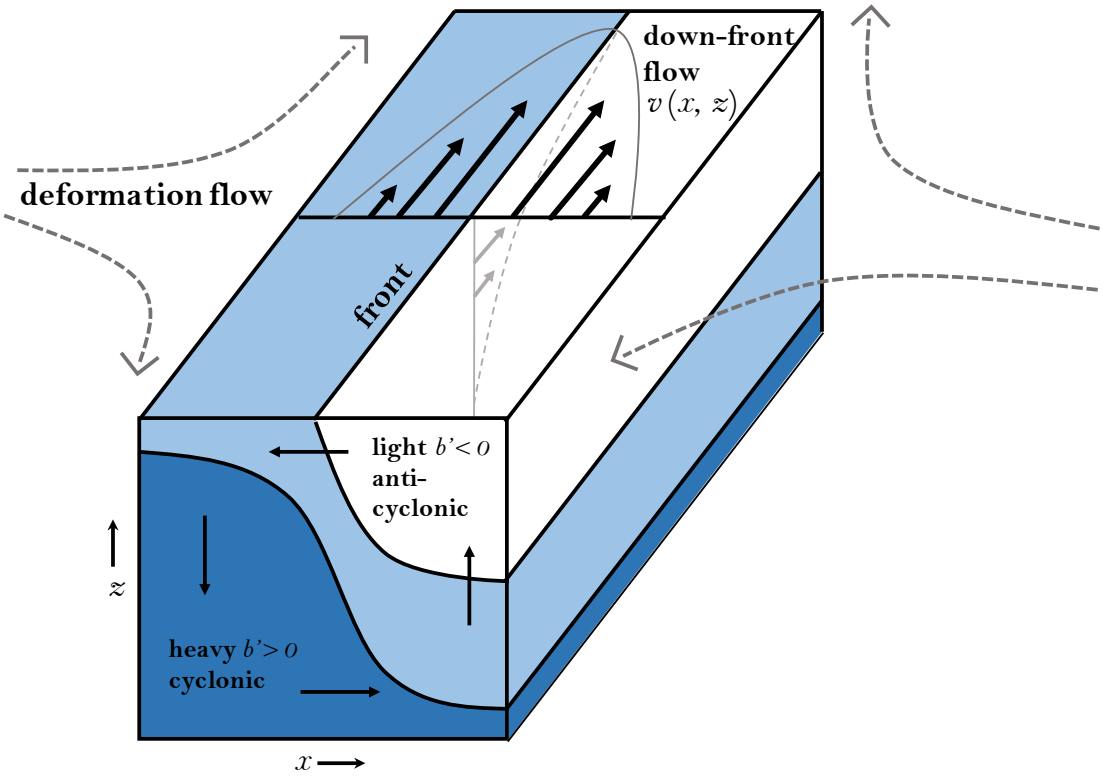

Figure 1.9: Surface frontogenesis caused by a large-scale deformation flow at a front. The along-axis flow is partly geostrophic, and the secondary circulation is ageostrophic. As the frontal gradient sharpens in time, *Ro* grows. With finite Ro, downwelling ($w < 0$) and cyclonic ($\zeta/f > 0$) flow occurring on the heavy side of the front dominate their opposite-sign counterparts.

due to unbalanced motions of the front. This may impact the temporal evolution of the stratification and shear reminiscent of geostrophic adjustment. Furthermore, as a result of Stokes drift vortex force during wind-wave interactions, turbulent energy and mixing may enhance the entrainment of heat flux into the mixed layer by a factor of 2-5 (McWilliams and Fox-Kemper, 2013), while the interactions between the surface waves and submesoscale instabilities and frontogenesis show that Stokes shear force and momentum transfer from submesoscale eddies significantly energize the frontal secondary circulation (Suzuki et al., 2016).

Recent observations made in the Southern Ocean indicate the submesoscale eddy

field is found to be highly spatially variable, with pronounced hot spots of submesoscale activity associated with high mesoscale strain (Bachman et al., 2017). Adams et al. (2017) find vertical velocities of $\mathcal{O}(100 \text{ m day}^{-1})$ along the edges of a mesoscale eddy with favourable conditions for submesoscale instabilities within the mixed layer, while observations from the same research project indicate that submesoscale disturbances can develop along dense filaments and are transformed into submesoscale Rossby waves propagating upstream relative to the eastward flowing ACC (Taylor et al., 2018).

1.4 Description of Chapters

The objectives of this thesis are to improve our understanding of mixed layer submesoscale dynamics in the open ocean from observational and numerical perspectives. Chapter 3 is a published article in *Journal of Geophysical Research: Oceans* where we determined the role of one-dimensional atmospheric forcing on the seasonal evolution of mixed layer stratification. Much of the theory of this work stemmed from my M.Sc. thesis. However, the analysis regarding the mixed layer restratification phase, particularly the use of the PWP model and the majority of the writing of the paper, was performed during my Ph.D. time. This publication is, therefore, an extension of previous work and not a repetition. The research chapters of this thesis are described as follows:

Chapter 3: Submesoscale processes promote seasonal restratification in the Subantarctic Ocean

Chapter 3 compares five months of glider data in the SAZ to a one-dimensional mixing model. It shows that the magnitude of seasonal mixed layer restratification cannot be explained by heat, freshwater, and momentum fluxes alone. The timing of seasonal restratification is consistent with the model simulation, however, during up-front winds and enhanced vertical buoyancy fluxes by submesoscale MLEs, the strength of vertical stratification can be 2 times larger than what the model predicts. Furthermore, it is shown that the stratification can be further modified during phases of strong down-front EBF, which coincide with a reduction in stratification and a deepening of the mixed layer.

Chapter 4: Southern Ocean seasonal restratification delayed by submesoscale wind-front interactions

Chapter 4 investigates the role of submesoscale processes on sub-seasonal to interannual variability of the mixed layer stratification using four years of high-resolution

glider data in the Southern Ocean. Embedded within the mixed layer seasonal cycle are transient decreases of stratification lasting days to weeks, which result in inter-annual variability in the seasonal onset of mixed layer restratification by up to a month. Parameterization of EBF as an equivalent heat flux in a one-dimensional mixed layer model shows that (1) the model mixed layer stratification that develops from the start of each season is more comparable to the glider observations than when the model is run using heat and freshwater fluxes alone and, (2) the parameterization dramatically improves the sub-seasonal variability of mixed layer stratification, particularly during the onset of seasonal restratification.

Chapter 5: Seasonality of submesoscales in the Subantarctic Ocean

Chapter 6 investigates the seasonality of submesoscale flows in the Subantarctic using a 1/36° three-dimensional NEMO model simulation. Submesoscale flows are shown to be more vigorous during winter due to the enhanced APE generated by the seasonal deepening of the mixed layer. The increase of APE promotes MLI generation and enhanced vertical buoyancy flux within the mixed layer. The seasonality of frontogenesis contrasts MLI, where enhanced values during the summer are associated with a seasonal maximum of horizontal buoyancy gradients and shallow mixed layers.

Chapter 6: Horizontal scales of variability in the Subantarctic: optimizing sampling techniques using ocean gliders

Chapter 6 simulates virtual gliders over a full annual cycle in the 1/36° NEMO model to understand the impact different glider sampling modes have on the observed distribution of horizontal buoyancy gradients. Gliders are able to successfully represent the distribution of horizontal buoyancy gradients over the annual cycle, with a slight under-estimation of the strong fronts. However, the variance of the glider observed buoyancy gradients only represent about 60% of the variance of the SAZ for meridional and box-shaped transects. Zonal and mooring mode sampling modes indicate a weak representation of horizontal buoyancy gradient variance (about 30%). Correlations

between the distribution of horizontal buoyancy gradients observed using a varying amount of gliders (one to six) sampling for varying amounts of time (a month to a year) provides the representative measure of the distribution of submesoscale gradients gliders will observe.

CHAPTER 2

Methods, data sources and models

2.1 Underwater gliders in ocean research

A glider is a buoyancy-driven autonomous underwater vehicle originally conceived in 1989 by Henry Stommel (1989). Stommel wrote a science fiction article where he described "a small fleet of neutrally-buoyant floats" that "migrate vertically through the ocean by changing ballast... steered horizontally by gliding on wings at about a 35 degree angle". At that time, data collection of large-scale ocean systems was primarily obtained by ship transects. His idea was to change the way that scientists observe the ocean. Stommel's visionary article proved to be the blueprint for future glider technology when in the mid-90s, the US Office of Naval Research provided funding for the development of gliders to three competing and cooperating groups: Spray, developed by Scripps Institution of Oceanography and Woods Hole Oceanographic Institution (Sherman et al., 2001); Seaglider, developed by University of Washington (Eriksen et al., 2001) and Slocum, developed by Webb Research (Webb et al., 2001).

This thesis makes use of data acquired by Seagliders. Buoyancy gliders function by changing their buoyancy, which changes the glider's volume and causes vertical motion within the water column. Horizontal movement is acquired by the drag imposed on the wings when the glider moves through the water. A glider dive is nominally from the surface to 1000 m and back, after which the glider then communicates by satellite through the iridium antenna while on site.

This allows for the transmission of data acquired on a previous dive and importantly, to receive new piloting commands from the shore. Global Positioning System (GPS) is acquired on the ocean surface, while below the surface gliders rely on a dead-reckoning to estimate location. Gliders use dead-reckoning to estimate a depth-averaged current for a particular dive. This is calculated by determining the difference between the actual surfacing location from a dive and the location where the glider should have surfaced given the direction and slope of the dive. Although gliders can be programmed to dive at various depths, in standard use, they dive to 1000 m where a typical dive cycle lasts $\sim$6 hours. A glider travels approximately 5 km horizontally

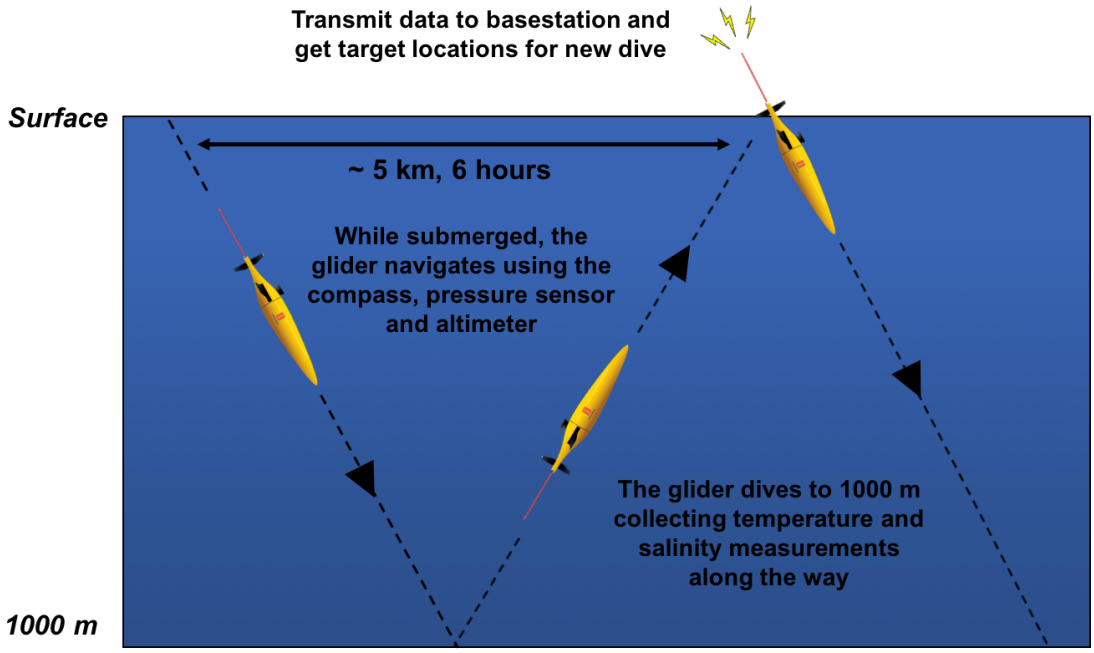

Figure 2.1: Schematic indicating a sawtooth diving pattern of the Seaglider. Gliders dive continuously from the surface to 1000 m and back, collecting variables at 0.2 *Hz* with a nominal horizontal spatial resolution of 5 km and a temporal resolution of 5 hours per dive. At the surface, Seagliders transmit data to the basestation via Iridium satellite and acquire target locations for the next dive.

per dive, depending on the background flow and the sampling mode chosen. This gives the glider a velocity of about 0.1 m s^{-1} and 0.25 m s^{-1} for vertical and horizontal motion, respectively. Gliders use lithium primary batteries for power, which translates to mission durations of up to a year, depending on how often the battery is called upon to use for flight adjustments and sensor operations. The deeper the dives, the less frequent the glider is required to undergo surface and apogee maneuvers, which is where most of the battery usage is expended. Therefore, the deeper dives require fewer requirements of surface and apogee operations and thus result in more battery efficiency.

2.2 Southern Ocean Seasonal Cycle Experiment

This work forms part of the Southern Ocean Seasonal Cycle Experiment (SOSCEx) under auspices of the Southern Ocean Carbon and Climate Observatory (SOCCO). SOSCEx represents a combined observational and modeling effort to address sub-seasonal and submesoscale questions which link the carbon cycle to climate variability in the Southern Ocean (Swart et al., 2012). This thesis attempts to understand how submesoscales impact mixed layer stratification dynamics through an *in-situ* and modeling approach in the SAZ. The observational component of the experiment takes place over the time period of September 2012 to December 2016, where a series of Seagliders (Section 2.1) were deployed from the South African Antarctic Research Vessels *S.A. Agulhas I* and *II*.

This thesis makes use of glider deployments in the SAZ region south of Africa. The initial analysis is performed on a glider deployed in austral spring south of Gough Island in the South Atlantic and piloted eastward toward the Greenwich Meridian for approximately five months (Chapter 3. This deployment represents a mostly zonal transect mode of sampling, covering approximately 8 degrees of longitude (11 °W to 3 °W). Chapter 4 makes use of glider deployments spanning over four years (2012 - 2016), with the aim to constrain the glider horizontal movement to a pseudo monitoring site at 43 °S, 8 °E. This location overlaps with the GoodHope monitoring line (AX25) that runs between Cape Town, South African and Antarctica. At this location, gliders were maintained in a box-shaped sampling pattern (∼20 km each side) throughout their deployment. A summary of the glider deployments is shown in Table 2.1.

2.2.1 Seaglider data flagging and binning

Gliders travel at a nominal vertical velocity of 0.1 m s^{-1} and sample at a rate of 0.2 *Hz*, providing a nominal vertical resolution of 0.5 m. Raw values of temperature and salinity are initially filtered by removing data outside of plausible limits. Temperature

Figure 2.2: Two Seagliders in their handling cradles being prepared for launch in the Southern Ocean as a part of the Southern Ocean Seasonal Cycle Experiment. The location of the conductivity, temperature and depth sensor (CT Sail) and the Iridium antenna is shown.

and salinity profiles are vertically binned to 1 m intervals and then individually smoothed by using a running mean filter across a 5 m depth interval. The data is not binned horizontally. Comparison of raw profiles to the interpolated data is shown in Figure 2.3. Refer to the methods sections of Chapters 3 and 4 and Swart et al. (2015) that provide details on the glider data handling and quality control.

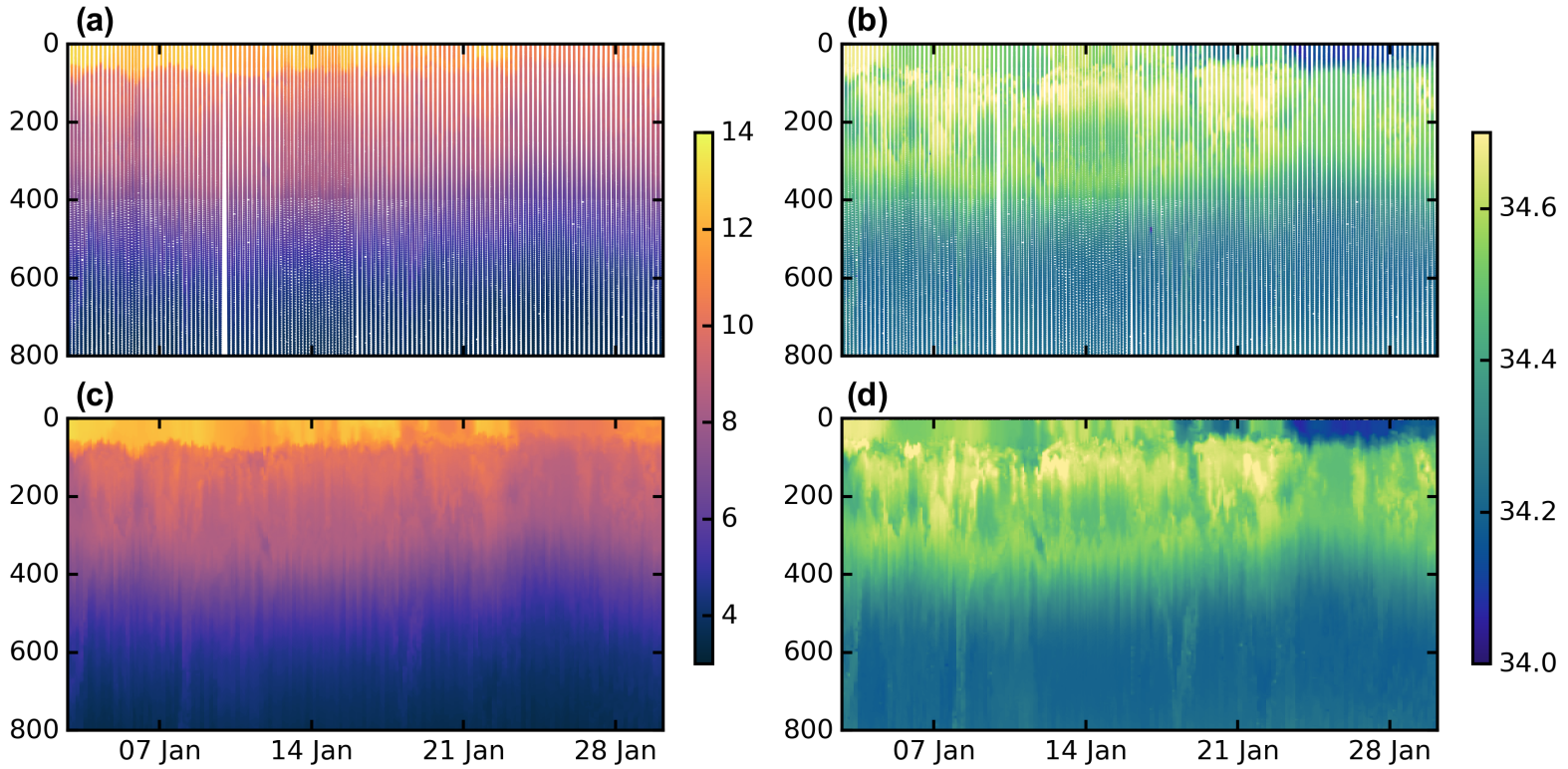

Figure 2.3: Raw observations of (a) temperature (°C) and (b) salinity as a function of time (days) and depth (m) for a glider deployed for a period during summer in 2012. (c) Temperature and (d) salinity gridded to 1 m and vertically smoothed using a running mean filter across a 5 m interval.

Deployment no.	1	2	3	4	5
Chapter used	3	4, 5, 6	4, 5, 6	4, 5, 6	4, 5, 6
Deployment date	26 Sep 2012	8 Dec 2012	10 Oct 2013	28 Jul 2015	16 Jul 2016
Retrieval date	15 Feb 2013	7 Mar 2013	8 Feb 2014	9 Feb 2016	22 Dec 2016
Duration (days)	143	90	119	198	160
Deploy location	42.9 °S, 11 °W	42.5 °S, 8 °E	43 °S, 8.5 °E	43 °S, 8.3 °E	43 °S, 8.4 °E
Retrieve location	41.6 °S, 3.2 °W	42.7 °S, 8.8 °E	42.9 °S, 7.8 °E	43 °S, 8.5 °E	42.5 °S, 9 °E

Table 2.1: Data coverage of Southern Ocean Seasonal Cycle Experiment glider deployments. Refer to the individual chapters used for the geographical maps and glider sampling patterns employed.

2.3 Price Weller Pinkel (PWP) mixed layer model

2.3.1 One-dimensional mixed layer model

In this thesis, the use of a one-dimensional mixed layer model is used to investigate the role of atmospheric forcing (momentum, heat, and precipitation) impacting the seasonal evolution of the mixed layer (PWP, Price et al., 1986). Destratification in the PWP model arrives via a momentum flux induced by winds, cooling from the ocean surface and evaporation due to high latent heat flux. Vertical mixing in the model will occur to satisfy the stability criteria which requires that

$$\rho_z \geq 0 \tag{2.1}$$

for static stability,

$$R_b = \frac{g\Delta\rho H}{\rho_0(\Delta U)^2} \geq 0.65 \tag{2.2}$$

for mixed layer stability, and

$$R_g = \frac{g\rho_z}{\rho_0(U_z)^2} \geq 0.25 \tag{2.3}$$

for shear flow stability. H is the MLD, U is a velocity of the water column and $\Delta()$ is the difference from the mixed layer base and just below.

These fluxes induce convective instability, entrainment from the pycnocline and a mixing term generated by vertical current shear. Increases in stratification in PWP occurs within the mixed layer where surface heating warms from the top and therefore creates vertical temperature stratification, while precipitation at the surface generates vertical salinity stratification. The surface heat flux term, $Q_{surface}$ is composed of the combination shortwave and longwave radiation, as well as latent and sensible heat fluxes. An additional term in PWP is an evaporation minus precipitation term, where evaporation is calculated directly from the latent heat flux. $Q_{surface}$ is absorbed into

the water column with a double exponential depth dependence. As the best fit to our study site, we use the e-folding penetrative depth of an open ocean water type determined by Paulson and Simpson (1977) where red light penetrates to 0.6 m and blue-green light to 20 m. Individual simulations of the PWP model are explained in Chapters 3 and 4.

2.4 NEMO model

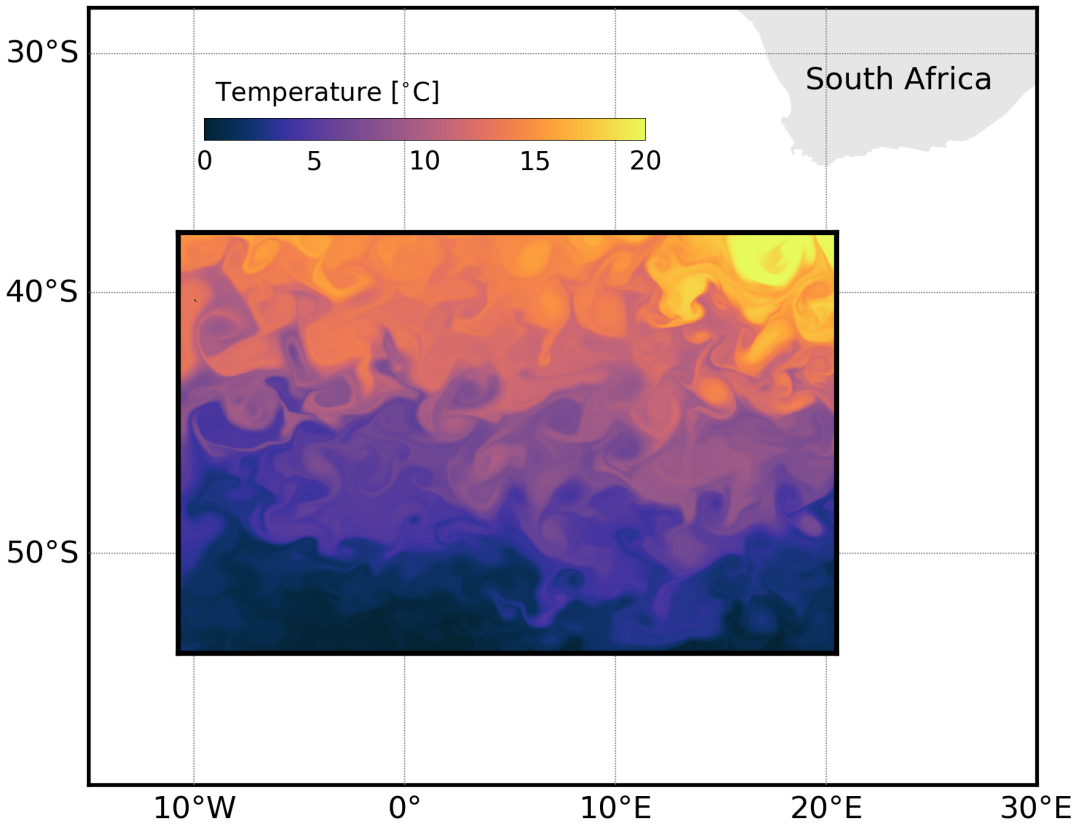

Figure 2.4: NEMO-SOSCEX36 model domain showing the sea surface temperature values on 1 January 2007.

Outputs from a NEMO model are used in this thesis. NEMO (Nucleus for European Modelling of the Ocean) forms the framework in which the models for various spheres of modeling operate (Madec, 2008). The configuration used in this thesis is the OPA

(Océan Parallélisé) ocean dynamics and thermodynamics model, which is a primitive equation model. It forms the base of the NEMO framework with which other models can be interfaced, such as LIM and PISCES (Madec et al., 1998). The model output used is a submesoscale resolving Regional South Antarctic Southern Ocean NEMO 3.4 configuration (NEMO-SOSCEX36, Figure 2.4).

The NEMO-SOSCEX36 simulation is run with a 1/36°resolution resulting in a horizontal spatial resolution range of 1.83 km to 2.4 km. NEMO-SOSCEX36 domain spans 10.1° W to 20° E and 53° to 38° S. There are 46 vertical levels with 14 levels within the upper 200 m and 20 levels within the upper 500 m. The simulation is realistically forced with ERA-Interim winds (3-hour temporal resolution), and surface fluxes (24-hour temporal resolution) interpolated to a time step of 3 minutes to force the model. The model was initialized from the January 2005 monthly-mean temperature and salinity, allowed a spin-up time of 1.5 years and then run for a further 4 years. This thesis makes use if a full seasonal cycle (1 January 2007 - 31 December 2007). Further details of the simulation can be found in Table 2.2 and in Chapters 6 and 5.

NEMO SOSCEX36 simulation			
Domain	Regional	38°S - 53°S 10°W - 10°E	
Horizontal grid	Resolution 1/36°	x=1089 y=784	
Vertical grid	46 vertical levels z coordinate	above 200 m below 200 m	14 levels 32 levels
Bathymetry	STRM30 30 bathymetry		
Initial conditions	BIOSATLANTIC 1/12°	Jan 2005 mean T and S No ice in model	
Time step	180s (3 minutes)		
Run duration	Spin up: 1.5 years Run: 4 years	Jan 2005 - June 2006 Jan 2005 - Dec 2008	
Lateral boundary	4 open boundaries Partial slip	BIOSATLANTIC 1/12°	
Surface boundary	Atmospheric forcing	ERA Interim	
		10m u and v	3 hours
		swrad, lwrad	24 hours
		tair, thumi (t2, q2)	3 hours
		precip, snow	24 hours
	Damping	Includes damping with Gouretski annual mean	
	Runoff	No rivers in domain	
	Sea surface restoring	Salinity only - using Levitus monthly climatology	
Bottom boundary	Nonlinear bottom friction calculated No geothermal heating Diffusive and advective BBL schemes activated.		

Table 2.2: Specifications of the NEMO-SOSCEX36 configuration.

CHAPTER 3

Submesoscale processes promote seasonal restratification in the Subantarctic Ocean

This chapter is published as M. du Plessis, S. Swart, I.J. Ansorge and A. Mahadevan (2017) Submesoscale processes promote seasonal restratification in the Subantarctic Ocean. J. Geophys. Res. 122(4).

3.1 Introduction

3.1.1 The Subantarctic mixed layer

This work follows the seasonal restratification of Subantarctic mixed layer. Classical thinking depicts that summertime restratification within the Subantarctic Zone (SAZ) is driven by the onset of warming, restratifying deep winter mixed layers, which often extend over 400 m (Sallée et al., 2010b) to shallower than 100 m during summer (Rintoul and Trull, 2001; Swart et al., 2015). A fundamental implication of the seasonal restratification is the extended availability of light to phytoplankton, which photosynthetically fix carbon at globally important rates. The Southern Ocean alone contributes to about one-third of the global organic carbon flux (Schlitzer, 2002), making seasonal variations of the mixed layer a critical component of the global carbon system. However, climate models are unable to accurately represent Southern Ocean mixed layer depth (MLD, Sallée et al., 2013a). Furthermore, Thomalla et al. (2011) indicate evident inconsistencies in the timing of enhanced seasonal phytoplankton growth and heat fluxes. Recently, Swart et al., 2015 use a high-resolution glider data set to show that spring and summer MLD variations can be separated into two distinct regimes. The springtime mixed layer undergoes large vertical migrations between the surface and the deep seasonal pycnocline (200-300 m), while during summer the MLD is consistently bound to a shallower (<100 m) seasonal pycnocline. Importantly, they show that during spring, periodic restratification events occur in the presence of horizontal density gradients, suggesting that seasonal variations of stratification in the SAZ are not solely driven by air-sea fluxes as these restratification events occur too rapidly to be attributed to surface heating alone. Swart et al. (2015) also reveal that spring restratification is concurrent with enhanced primary production, while Thomalla et al. (2015) apply the same data set to show this bloom initiation to be associated with increased light availability due to these periods of enhanced restratification. Both studies elude the spring restratification and bloom initiation to submesoscale processes based on numerical model studies and Northern Hemisphere observations. This study aims to elucidate

the role of submesoscale processes during seasonal restratification of the SAZ ML, which is particularly important in the context of coupled physical-biological dynamics, and therefore for the climate.

3.1.2 Restratification by submesoscale mixed layer eddies

Developments in numerical modeling have greatly enhanced our understanding of ocean processes occurring at the submesoscale (Haine and Marshall, 1998; Thomas and Lee, 2005; Boccaletti et al., 2007; Fox-Kemper et al., 2008; Mahadevan et al., 2010). Submesoscale flows develop in localized regions of the surface ocean where the vertical component of the relative vorticity attains a magnitude as large or larger than the planetary vorticity. These often occur due to mesoscale straining and frontogenic processes which lead to an intensification of the frontal jet due to enhanced thermal wind shear. Submesoscale flows develop within horizontal scales of the mixed layer deformation radius (typically around 10 km) (Hosegood et al., 2008) where the flow is no longer influenced by the Earth's rotation. Frontally geostrophic flow with weak stratification can spontaneously become baroclinically unstable (Boccaletti et al., 2007) and lead to the formation of mixed layer eddies (MLEs). MLEs apply a thermally direct overturning circulation within the mixed layer that draws on the potential energy stored in the upright front. MLEs move the lighter water of the front up and over the heavier water to tilt isopycnals toward the horizontal, restratifying the mixed layer. MLEs are difficult to observe due to their small spatial (0.1–10 km) and rapidly evolving (few days) scales. However, owing to their ability to observe the ocean at high spatial and temporal resolutions, ocean gliders are beginning to reveal the role of MLEs on the restratification of the ocean mixed layer (Mahadevan et al., 2012; Swart et al., 2015; Thompson et al., 2016). Mahadevan et al. (2012) provide observational evidence of MLE processes driving a springtime restratification of the mixed layer affecting the timing of the North Atlantic seasonal phytoplankton bloom initiation. Thompson et al. (2016) show a distinct seasonal cycle in mixed layer instabilities and highlight the role MLEs have on periodic restratification during the boreal winter.

Both studies are North Atlantic focused, while the Southern Ocean has received limited consideration. However, Southern Ocean focused models are beginning to suggest that submesoscale processes may be important in upper ocean dynamics (Nikurashin et al., 2012; Rosso et al., 2014; Forryan et al., 2015). Additionally, a study by Monteiro et al. (2015) use hourly observations of CO_2 fluxes in the SAZ to indicate the necessity of sub-daily sampling to resolve intraseasonal upper ocean dynamics which have potentially important biogeochemistry related variability. These results place an important emphasis on the need for ocean observations at the right space and time scales in the Southern Ocean.

3.1.3 The impact of winds on mixed layer eddies

Work done by wind on the stratification (Thomas and Ferrari, 2008; Thomas and Taylor, 2010; Mahadevan et al., 2010) has shown that winds aligned with the geostrophic current inputs energy into the upper ocean and drives a horizontal Ekman advection across the front. Mahadevan et al. (2010) examined MLE-driven restratification in the presence of winds. They show when the direction of the wind is downstream of the frontal current (down-front) and is sufficiently strong, a surface Ekman flow occurs from the dense side of the front to the light side, keeping the isopycnals of the front upright and preventing MLEs from restratifying the mixed layer. D'Asaro et al. (2011) use observations at a front in the Kuroshio Current to show that down-front winds impart an Ekman buoyancy flux (EBF) to catalyze a release of energy in the front, enhancing the turbulence by one to two orders of magnitude. They postulate these processes to be important in regions such as the Antarctic Circumpolar Current (ACC). However, should the wind direction be reversed, it will effectively hasten the restratification process by driving a flow of lighter water over the heavier side of the front. We postulate that the role of the intense westerly winds of the Southern Ocean may be important in opposing any mixed layer restratification flux imposed by MLEs.

3.1.4 Focus of this study

Following Swart et al. (2015) and Thomalla et al. (2015), the deployment of an autonomous ocean glider during the Southern Ocean Seasonal Cycle Experiment (SOSCEx, Swart et al., 2012) is used to study the seasonal restratification in the SAZ. This study presents almost five months of continuous, *in-situ* water column observations from the early austral spring in 2012 to the late summer of 2013 (Figure 3.1). This work aims to provide more detail of the observed submesoscale field of the SAZ and characterize the role of horizontal buoyancy gradients and MLEs in setting the mixed layer restratification observed in Swart et al. (2015). We use a one-dimensional vertical mixing model to separate the stratification driven by air-sea heat and momentum fluxes from the glider-observed ocean stratification. Following this, we compare the restratifying flux by MLEs, the wind-driven EBF and the surface heat fluxes of the region. In summary, we characterize the processes that set the seasonal stratification in the SAZ and provide unique observational evidence of submesoscale flows in the open ocean Southern Ocean.

3.2 Data and methods

3.2.1 Glider sampling strategy

Ocean gliders have proven to be effective platforms in acquiring high spatial and temporal mixed layer variability (*e.g.* Ruiz et al., 2012). The glider used in this work (Seaglider 573) continuously sampled in a 'V-shaped' pattern from the surface to a nominal depth of 1000 m and back to the surface. The horizontal and temporal resolution of a given dive is dependent on the slope of the V-shape pattern, where during this experiment, an average horizontal resolution of 1.4 ± 0.9 km and an average temporal resolution of 2h $\pm$ 56 min per profile (two profiles per dive) was obtained. A total of 1164 profiles were obtained with a mean horizontal velocity of 0.3 m. s^{-1} and a nominal vertical velocity of 0.1 m s^{-1} for the period. The hydrographic data were obtained using a Sea-Bird Electronics SBE41 unpumped conductivity (salinity),

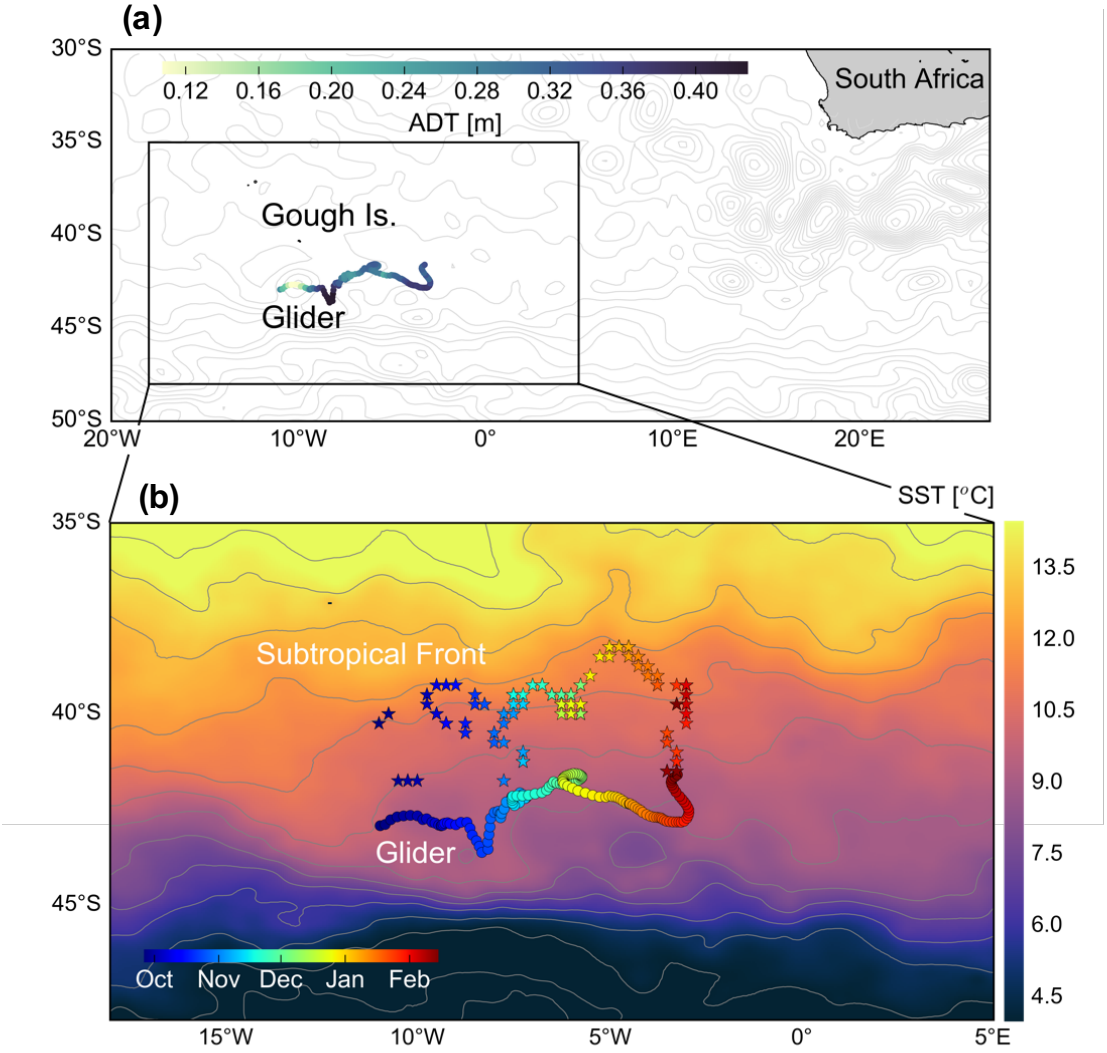

Figure 3.1: (a) The trajectory covered by the Seaglider (SG573) for the duration of our field campaign SOSCEx (25 September 2012 to 15 February 2013). Colors represent the Absolute Dynamic Topography (ADT) value at each daily mean glider dive location acquired from AVISO. The backdrop represents the ADT contours of the day of deployment separated by 0.1 dyn m. (b) Circles show the SG573 transect, while the stars show the location of the Subtropical Front. Both are colored to represent the date of each respective daily location so that the date of the SG573 dive and the location of the Subtropical front are comparable. Background color indicates the SST from the OSTIA product for the date of deployment. Contours of SST are colored gray and separated by 1°C.

temperature, and depth profiler (CT-Sail), which sampled with an average rate of 0.2 Hz, attaining a vertical resolution of approximately 0.5 m. At the deployment and retrieval of the glider, ship-based CTD casts were completed, together with salinity, dissolved oxygen, and chlorophyll-a bottle collections, to calibrate the glider sensors. Salinity measurements were checked and corrected for conductivity sensor drift, while glider salinity accuracy was calculated to be within 0.03 [see Swart et al. (2015), for further detail]. SG573 was deployed on 25 September 2012, south of Gough Island in the South Atlantic Ocean (42.98 °S, 11.8 °W) and steered predominantly eastward and remained within the frontal bounds of the SAZ. The glider was retrieved on 15 February 2013 (41.68 °S, 3.28 °W), spending a total of 143 days within the SAZ (Figure 3.1).

3.2.2 PWP model analysis

The PWP model used in this work is described in Section 2.3. The PWP model was initiated with an average of the first 25 glider profiles of temperature and salinity and run for the duration of SOSCEx (143 days). Wind stress and $Q_{surface}$ were applied at 6-hourly intervals to match the resolution of the satellite products. The MLD was determined using the density difference criteria of 0.03 kg m^{-3} from a 10 m reference level (de Boyer Montégut et al., 2004). It is noted within this work that the along-track glider observations may depict a bias due to the effects of advective, submesoscale, or other internal processes. However, this experiment aims to separate the stratification driven by changes in the one-dimensional atmospheric forcing from the regional advancement of *in-situ* stratification. The method provides a basis to characterize temporal changes in mixed layer stratification driven by three-dimensional processes.

3.2.3 Satellite products: local atmospheric forcing

WINDS AND FRESHWATER FLUXES

Wind and rainfall data were obtained from the National Centers for Environmental Prediction (NCEP) taken at 10 m above sea level reference height and the surface, respec-

tively (http://www.esrl.noaa.gov/psd/data/gridded/data.ncep.reanalysis.pressure.html). The amalgamation produces a 1/48 ° gridded field at 6-hourly intervals at UTC/GMT 00, 06, 12, and 18Z. Wind speed was converted to wind stress using the methods from Large and Pond (1981).

SURFACE FLUXES

Due to limited direct observations and a lack of validation studies of solar heat fluxes ($Q_{surface}$) in the Southern Ocean, applying the most accurate reanalysis $Q_{surface}$ presents challenges. In this work, our choice of $Q_{surface}$ was identified from two independent studies which performed a correlation analysis between various reanalysis products and *in-situ* measurements within the Southern Ocean (Caulet et al., 2015) and the Indian Ocean (A. Tandon, personal communication). The Modern-Era Retrospective Analysis for Research and Applications (MERRA) provided stronger correlations in both sites and is therefore used in this work. MERRA reanalysis is produced using the Goddard Earth Observing System atmospheric model and data assimilation system (Rienecker et al., 2011). Observational inputs into MERRA include those from ship and buoy measurements with satellite radiances from the Geostationary Operational Environmental Satellite sounder, Television, and Infrared Observation Satellite, Operational Vertical Sounder, Advanced TOVS instruments, the Atmospheric Infrared Sounder, the Microwave Sounding Unit, the Advanced Microwave Sounding Unit-A, and SSM/I. Further information regarding the system, the input data streams and their sources, and the observation and background error statistics can be found in Rienecker et al. (2011).

SEA SURFACE TEMPERATURE

Maps of sea surface temperature (SST) are used to provide regional scale understanding of the physical environment of the glider observations. The SST data set used in this work is produced at 1 km resolution by Jet Propulsion Laboratory Regional Ocean Modeling group uses satellite data from sensors that include Advanced Very High-

Resolution Radiometer (AVHRR), the Advanced Along Track Scanning Radiometer (AATSR), the Spinning Enhanced Visible and Infrared Imager (SEVIRI), the Advanced Microwave Scanning Radiometer-EOS (AMSRE), the Tropical Rainfall Measuring Mission Microwave Imager (TMI), the Moderate Resolution Imaging Spectroradiometer (MODIS), the Geostationary Operational Environmental Satellite (GOES) Imager, the Multi-Functional Transport Satellite 1R (MTSAT-1R) radiometer, and in situ data from drifting and moored buoys.

3.2.4 Submesoscale mixed layer dynamics

Fox-Kemper et al. (2008) provide a parameterization of the restratification process by MLEs restratification. Mahadevan et al. (2012) showed this parameterization could be represented in terms of a equivalent restratifying heat flux by MLEs comparable to surface heat fluxes (Q_{MLE}, Eq. 3.1). The application of Q_{MLE} is consistent with analysis provided in the Northern Hemisphere studies (Mahadevan et al., 2012; Thompson et al., 2016). As MLEs convert horizontal buoyancy gradients to vertical stratification, Q_{MLE} is dependent on the strength of the horizontal buoyancy gradients and the MLD,

$$Q_{MLE} = C_e \frac{b_x^2 H^2}{f} \frac{C_p \rho}{\alpha g} \mu(z), \tag{3.1}$$

where is f the Coriolis parameter, C_p the specific heat capacity of seawater, α the thermal expansion coefficient of seawater, g the gravitational acceleration, ρ is the density, b_x is the horizontal buoyancy gradient sampled by the glider, and H is the MLD. C_e is an empirically defined coefficient determined by numerical models and taken to be 0.06 (Fox-Kemper et al., 2008). We accept this may not be an accurate representation of the Southern Ocean but is currently our best estimate available. It should be noted that the strength of the restratification process is not uniform throughout the mixed layer, instead it reaches a maximum at the center of the mixed layer and decreases toward zero at the surface and MLD (Fox-Kemper et al., 2008). The vertical structure function $\mu(z)$ defines this relative rate of restratification for Q_{MLE} at the various depths within the mixed layer. For simplicity, we set $\mu(z)$ to 1 to represent

the maximum restratification occurring within the mixed layer for each buoyancy flux parameterization.

Winds directed along the flow of the front will oppose MLE through an Ekman flow of water from the dense side of the front over the lighter side. Therefore, this wind-driven mechanism reduces ocean stratification where the wind stress is aligned with the geostrophic shear (Thomas, 2005). As for Q_{MLE}, an equivalent heat flux for the wind-driven EBF can be expressed as,

$$Q_{EBF} = -\frac{b_x \tau^y}{f} \frac{C_p}{\alpha g}, \tag{3.2}$$

with τ^y the down-front component of the wind stress. The strength of the horizontal buoyancy gradients and the down-front wind stress are the two important varying factors that drive the strength of the wind-driven flux. The zonal orientation of the mean fronts of the ACC (Figure 3.1) is aligned with the westerly component of the wind stress (positive values of τ^y) which is down-front to the mean flow in direction. Similarly, easterly winds are considered up-front (negative values of τ^y) as these winds oppose the direction of the mean geostrophic flow. We acknowledge this is only a representation of the mean sense of the flow where there may be misalignment with our estimates of down-front winds and the true direction of the local front. The glider sampling strategy was to direct the glider toward 0 °E and as such the true strength of the front, when occupying a meridional orientation, is likely underestimated. Importantly, the competition between the restratification processes of MLEs, which are inherently positive, and EBF (Eq. 3.2), which can be positive or negative, sets the equivalent heat fluxes, which compete with solar heating to define the stratification of the mixed layer.

3.3 Results and discussion

3.3.1 *In-situ* observations: Characterizing the seasonal variations of the Subantarctic mixed layer

The five-month glider experiment encompasses two seasonal regimes where the upper ocean temperature environments show distinct differences (Figure 3.2). This is illustrated in Figure 3.2a, where a southward migration of surface warming across the location of the glider occurs as the time series progresses, thus separating the spring and summer periods. Although this is a gradual process, the position of the glider relative to this warming allows a defined date of spring/summer separation, on 28 November (Swart et al., 2015). This date corresponds to where surface warming (indicated by the 11 °C isotherm in Figure 3.2b) drives the development of a thermocline originating from the surface, which merges with the deeper 'seasonal' thermocline (Figures 3 and 4 in Swart et al., 2015) to form the base of the mixed layer for the remainder of the time series.

Figure 3.3 displays the mixed layer temperature and salinity variations scaled to show equal contributions to changes in density. Here, the separation between the spring and summer mixed layer regimes is clear. Mixed layer temperature and salinity variations on density were compensated for extended periods during spring, while surface warming during summer continually increased the buoyancy of the mixed layer more so than mixed layer freshening. The authors propose that the date of the seasonal transition from deep mixed layers during spring to shallow mixed layers during summer is not consistent throughout the SAZ. It is likely that zonal asymmetry in surface heat fluxes and MLDs provide different seasonal restratification dates (Sallée et al., 2010b). During spring, varying phases lasting less than a week, and approximately three weeks show that variations of mixed layer temperature and salinity compensate, having no or little effects on density (see gray shading in Figure 3.3). Meanwhile, interspersing periods have temperature and salinity variations which do not compensate each other (see green shading in Figure 3.3). In such cases, increasing

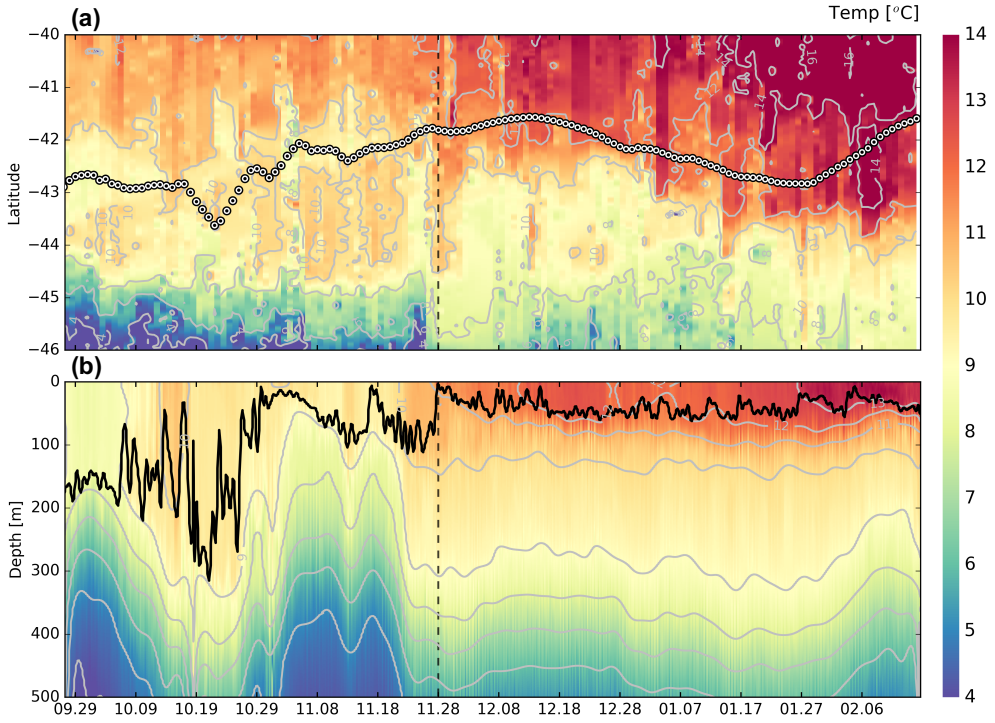

Figure 3.2: (a) Hovmöller representation of the seasonal progression of SST (°C). Black dots indicate the daily mean SG573 location. The first period of sampling (deployment to 28 November, which is indicated by the vertical dashed line) can be characterized by mesoscale, synoptic warming events extending up to 2° latitude southwards, while the second period (latter half of the time series) is dominated by the seasonal southward progression of warming SST. (b) Depth-time temperature section from SG573 where the feature-driven environment during the first half of sampling dominates the mixed layer depth (black line) variability. Gray lines indicate isotherms for the top and bottom plot.

temperature and/or freshening of the mixed layer enhance the buoyancy, changing the density of the mixed layer. Meanwhile, during summer, the near-persistent increase in temperature and gradual decline in salinity indicate a completely different environment where the mixed layer becomes increasingly buoyant with time. In the following two subsections, we separate and examine the spring and summer periods individually to provide intraseasonal evaluations of upper ocean physical variability in the SAZ.

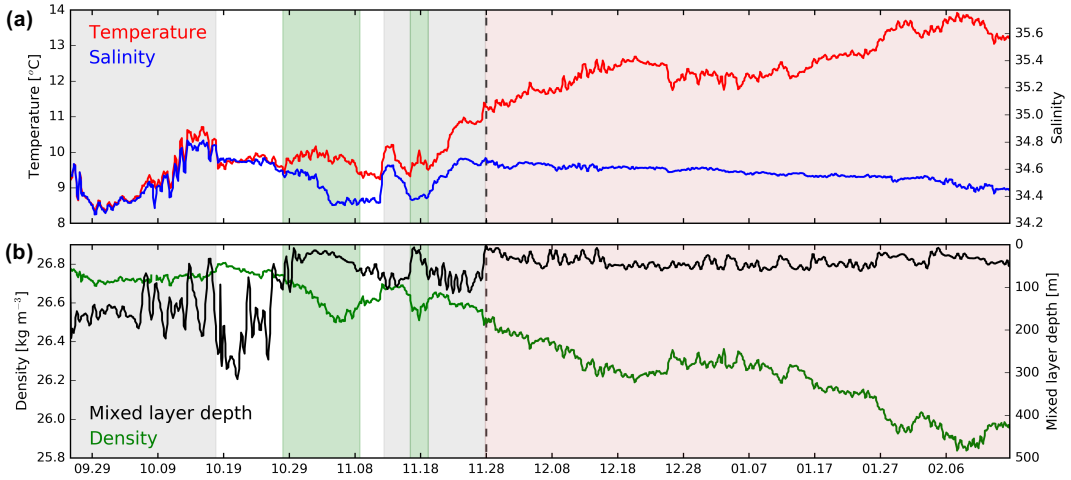

Figure 3.3: (a) Mixed layer temperature (red line) and salinity (blue line) variations throughout the glider time series. The vertical axes are scaled by α (temperature) and β (salinity) so that variations in T and S have equal effects on density. Spring and summer periods are separated on 28 November by the dashed vertical line; hereafter temperature dominates the variations to density. Gray-shaded areas indicate where density-compensated changes in T and S occur while green shading depicts where variations in either T or S alter mixed layer density. White areas represent insignificant variations in T and S. (b) Mixed layer density (green line) and depth (black line). Shading as is in the top plot, where variations in mixed layer density during the green-shaded periods are synonymous with the mixed layer depth below 100 m.

3.3.2 Spring: October-December

Figure 3.2a indicates that the glider was deployed within the zone of 9 °C SST water. As time progressed, episodic events whereby surface waters warmed up to 2 °C were observed. These signatures represent synoptic scale warming extending up to 2° of latitude in the SST. The glider temperature depth section indicated that these warming events extend vertically throughout the mixed layer (Figure 3.2, *e.g.* mid-October and mid-November), driving temperature and salinity ranges of 8.5-11 °C and 34.3-34.8 during spring (Figure 3.3). Mixed layer temperature and salinity varied as rapidly as 0.8 °C d^{-1} and 0.2 d^{-1}, respectively. Longer scale changes of the upper ocean temperature structure spanning many weeks were reflected in the vertical displacement of isotherm

depths by approximately 200 m. This was noticeable in November by a clear doming of the 5-9 °C isotherms (Figure 3.2b). It is likely this type of variability was imparted by a combination of time-varying forcing mechanisms altering the physical properties of the mixed layer and variations of the glider location as a result of the sampling strategy. Therefore, this dataset demonstrates multiscale upper ocean variability, ranging from the rapid daily variations to the longer weekly synoptic scales. Owing to its highly energetic nature, mesoscale eddies in the Southern Ocean are prevalent. The glider was deployed directly west of a cold-core cyclone of diameter 200 km, which may have broken off from a meander of the SAF. The glider performed a direct crossing of the cyclone during the first two weeks of the deployment (Figures 3.4a-c). A vertical section of upper ocean temperature as the glider crossed the eddy is shown in longitudinal space (Figure 3.4d). Classical doming of the isotherms toward the warmer edges of the cyclone were seen, with characteristic upwelling through the eddy core, as seen by a temperature and salinity reduction in the center to the coldest (8-9 °C) and most fresh (34.3-34.4) for the entire experiment. The mixed layer density (26.6-26.7 kg m^{-3}) was characteristic of Subantarctic Mode Water (McCartney, 1977). Despite the temperature and salinity gradients across the eddy, their relative effects on density were mostly compensated and thus horizontal density gradients were weak. Contrasting dynamic exists where variations of mixed layer temperature and salinity were not compensated and thus changes in temperature and/or salinity alter the density of the mixed layer (Figure 3.3). This occurred from 29 October for two weeks (green-shaded areas of Figure 3.3), where warming and freshening resulted in less dense and shallowing mixed layers from > 200 m to above 100 m. The interest of this study is to investigate these processes and identify their role in setting the stratification of the upper ocean, especially during these non-compensated regimes, where horizontal density gradients may play an important role in mixed layer physical dynamics.

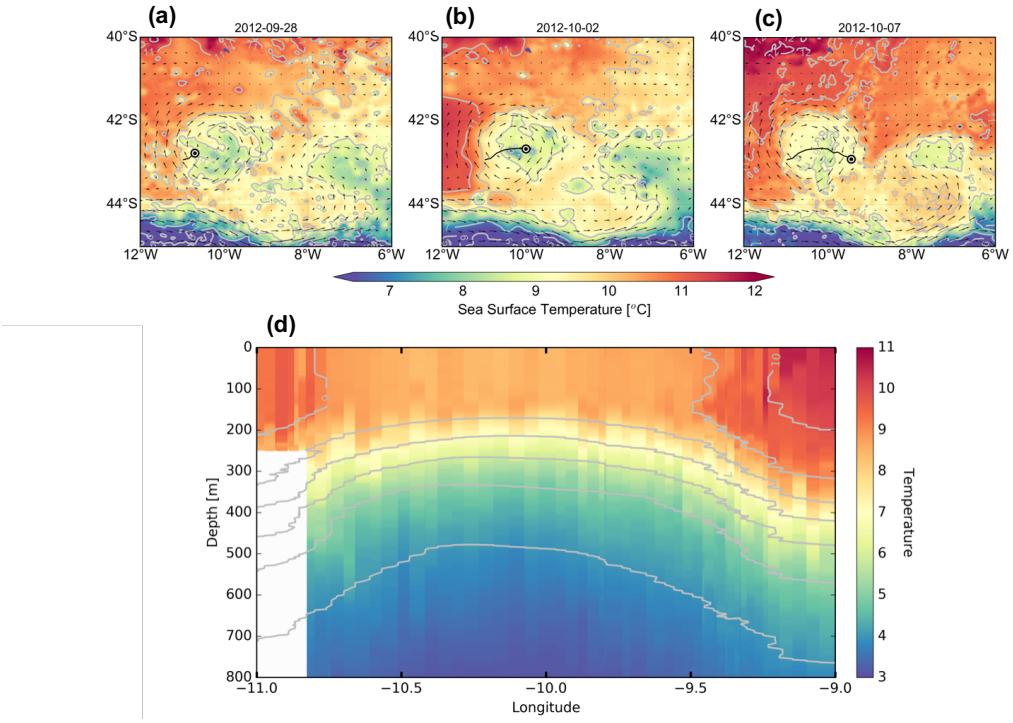

Figure 3.4: (a) Series of three daily sea surface temperature (SST) maps indicating the cyclone (∼43 °S, 10 °W) crossed by the glider track (white-black dots). Arrow indicate AVISO surface velocities. (b) Vertical temperature section of the black glider line shown in the third SST plot (7 October).

3.3.3 Summer: December-February

Regional surface warming and shallow (< 100 m) mixed layers are typical for this region and season (Sallée et al., 2010b). Swart et al. (2015) found a strong connection between mixed layer deepening and enhanced wind stress events related to mid-latitude storms varying at the synoptic scale (4-9 days). Further attention is needed to assess the influence of horizontal submesoscale processes on the MLD variability during this time. Our observations indicate the regional context of the glider's sampling trajectory moving southward for the majority of the summer (December-February) at around the same rate as the southward propagation of surface warming, *i.e.* southward migration of outcropping isotherms (Figure 3.2a). This results in an underestimation of the

seasonal warming which would likely occur at a single location over the season. Nevertheless, a comparison of the seasonally averaged temperature profiles in Figure 3.5 indicates the upper 50 m warmed by approximately 2.5 °C from spring to summer. Additionally, vertical variations of the MLD are indicated in Figure 3.5 by a measure of the standard deviation for each season, where a reduction from 79 m to 16 m occurred from spring to summer.

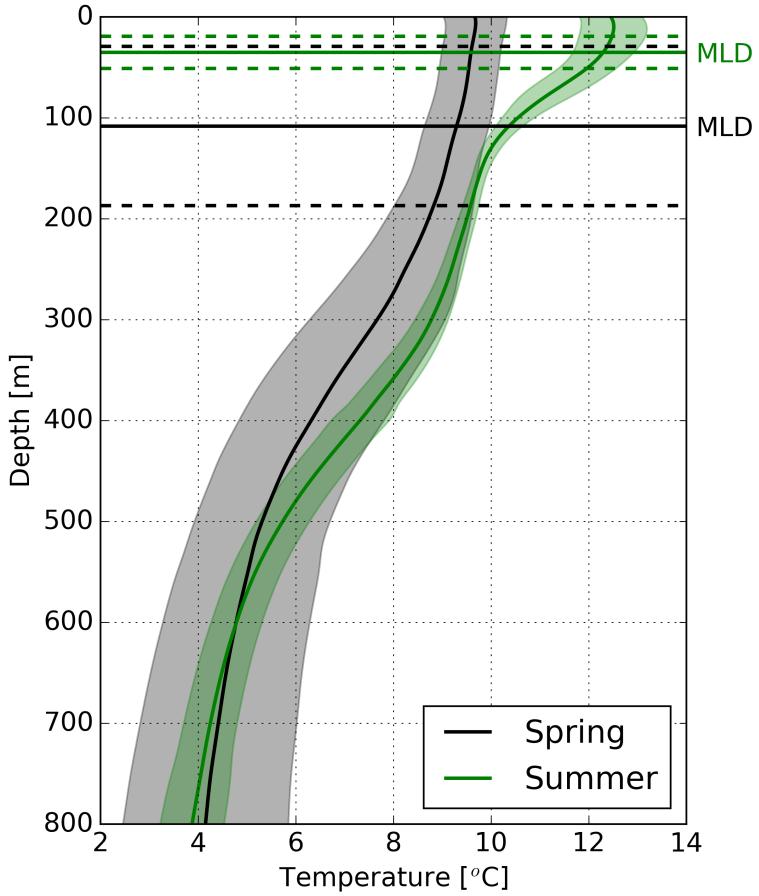

Figure 3.5: Mean temperature profiles for spring (25 September to 28 November) and summer (29 November to 15 February) shown as thick black and green lines, respectively. Standard deviations of the temperature at each depth are represented as the shaded areas. The mean mixed layer depth (MLD) for each season is shown by the horizontally orientated solid lines, with one standard deviation shown above and below the MLD as the dashed lines.

These correspond well to the estimates made for the entire Southern Ocean, which represent the large-scale seasonal variations in heating and its effects on upper ocean variability (Sallée et al., 2010b). Interestingly, despite the shallowing of the mixed layer and its variability during summer, standard deviations of the mixed layer temperature were comparable between spring (0.63 °C) and summer (0.64 °C) (Figure 3.5). This indicates that the processes impacting the sub daily upper ocean temperature variations were present during spring and summer. Sharp variations of mixed layer density occurred during periods where temperature and salinity variations were large (Figure 6). These rapid changes in density were aligned with temporal variations associated with submesoscale variability, *i.e*. within a few days. These can be identified as 'sharp' periods of lighter and denser surface waters which occurred frequently throughout the time series, often resulting in mixed layer density changes up to 0.1 kg m^{-3} d^{-1} (Figure 3.6). At these locations, upper ocean stratification, taken as the average N^2 over the top 100 m, show weakening during phases of denser mixed layers and strengthening during periods of lighter mixed layers. Notably, during green shades areas of Figure 3.6, mixed layers rapidly became less dense while the mixed layer began to restratify. Similarly, the increase of mixed layer density destroyed stratification, *e.g*. during mid-November. As MLEs actively slump vertical isopycnals in the presence of large horizontal density gradients to restratify the water column and EBF advects heavier water over lighter water to mix the upper ocean, it is postulated that submesoscale processes are likely important in altering the upper ocean stratification. However, it needs to be considered that these changes in density and stratification may be the result of air-sea heat and momentum exchange imparting intraseasonal variability on mixed layer temperature through warming (less dense) and mixing (more dense), such as would be modulated by synoptic scale winds. Therefore, to investigate the role of one-dimensional air-sea exchange processes on the observed stratification, such as wind and surface heat flux, we employ the one-dimensional PWP model with the observed one-dimensional forcing parameters. We compare the stratification derived by the one-dimensional processes to the observed ocean stratification to separate the

three-dimensional processes from the one-dimensional domain.

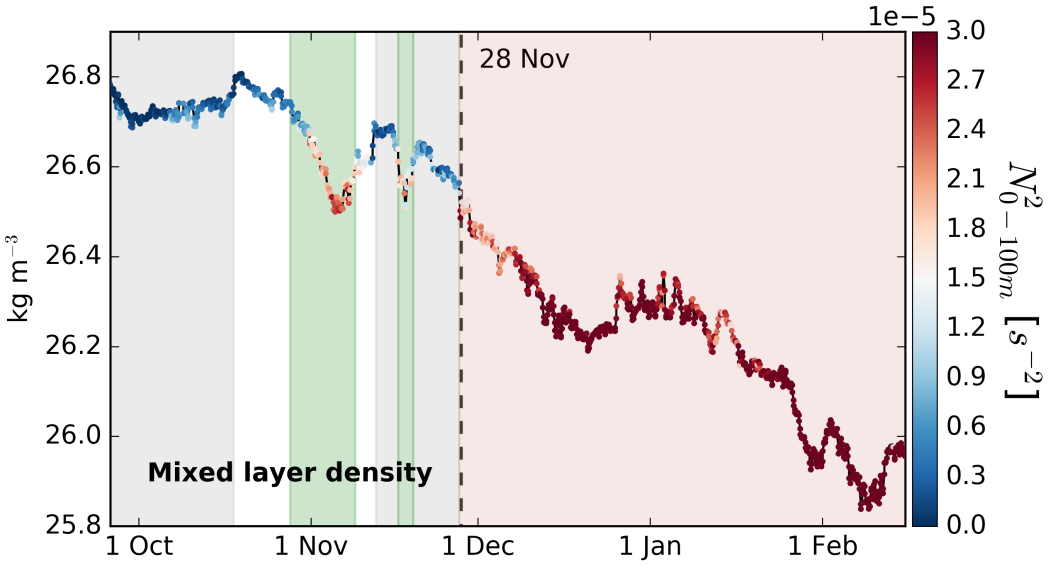

Figure 3.6: Density averaged over the mixed layer for the entire glider data set. The gradual decline in mixed layer density represents the impact of seasonal warming of the upper ocean. Colors are a representation of the stratification (N^2) averaged for the upper 100 m of the ocean. Green shaded areas show where enhanced upper ocean stratification agrees with mixed layer density becoming less dense. Shading as in Figure 3.3.

3.3.4 One-dimensional model comparison: atmospheric parameters

The model is forced with meteorological data acquired at the time and location of the nearest glider profile. Winds varied at the synoptic scale (Figure 3.7a), indicative of the storm-like activity in the Southern Ocean (Trenberth, 1991). This indicates that the glider moves slowly in comparison to the regional trajectory of the Southern Ocean storms and can, therefore, sample the effects of the storms on the water column. A mean wind stress of 0.19 N. m^{-2} was recorded, while two extreme storms intercepted the glider during mid-November and late-December, where wind stress values exceeded 1 N. m^{-2}. Surface heat flux variations (Figure 3.7b) were characterized by a strong diurnal signal. Strong cooling periods (-300 W. m^{-2}) were dominated by

intense heating regularly exceeding 800 W. m^{-2}. A mean positive $Q_{surface}$ (104 $\pm$ 281 W. m^{-2}) indicated a net input of buoyancy to the surface of the mixed layer throughout the model simulation. These heat, momentum (Figures 3.7a and b), and freshwater (not shown) fluxes were used to force the PWP model for 143 model days.

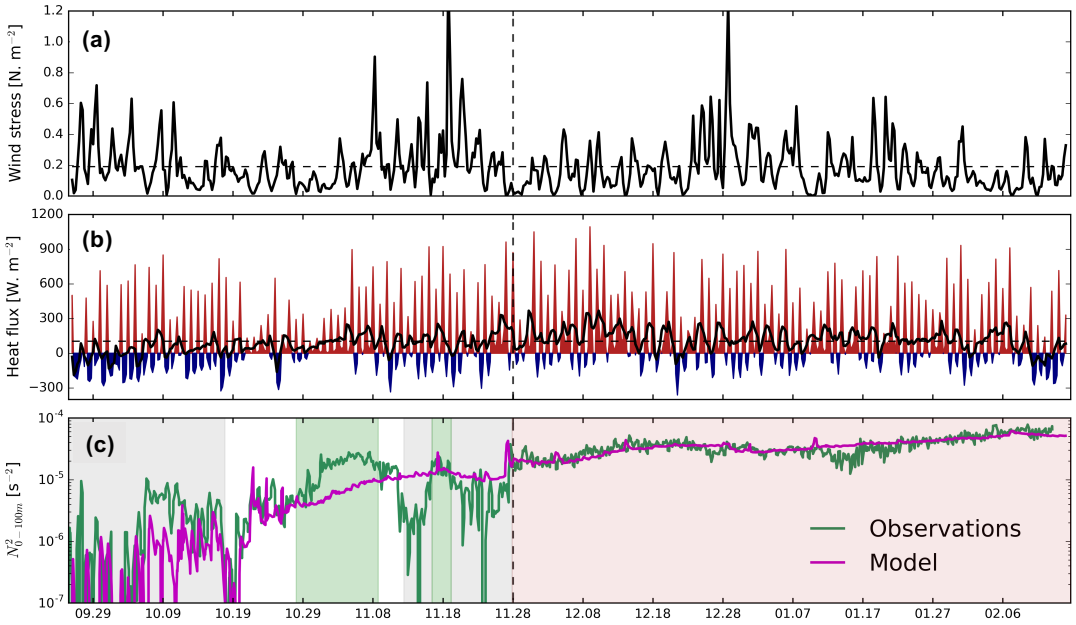

Figure 3.7: (a) NCEP wind stress (N. m^{-2}) colocated to the time and position of glider profiles and used for the PWP model run. (b) MERRA 6-hourly net heat flux ($Q_{surface}$) at the ocean surface (red (blue) indicates ocean heating (cooling)) indicates a strong diurnal structure with a net positive heat flux into the mixed layer. (c) Time series of stratification (N^2) averaged for the upper 100 m for SG573 (green line) and the PWP model (magenta line). Shaded areas are as in Figure 3.3.

Seasonal mixed layer restratification by model and glider observations

In our observations, springtime restratification developed as a stratification emerging from the surface of the ocean. This is distinct from a shoaling of the seasonal pycnocline. The transition into summer was signified by a merging of the seasonal pycnocline with the springtime restratification at approximately 50 m, forming mixed layers for the remainder of summer shallower than 100 m (Figure 3 in Swart et al. (2015)). Therefore,

we use the stratification index N^2, where N^2 is averaged over the top 100 m of the water column (N^2_{0-100m}) to provide an understanding of the development in seasonal restratification. Figure 3.7c shows the direct comparison of the N^2_{0-100m} between the PWP model and the glider observations. The majority of October exhibited weak stratification. However, small, significant increases of glider-observed stratification (N^2_{0-100m} 0.5-1 $\times$ 10^{-5} s^{-2}) were found around 9 October, which remained absent in the model. Weak heating and intermittent wind stress bursts of over 0.6 N. m^{-2} likely provided sufficient near-inertial shear to prevent the upper ocean from stratifying. Additionally, this period coincides with the glider exiting the mesoscale cyclone. Interleaving water masses of the cyclone and ambient water could potentially provide stratification by small density changes between water masses undergoing a release of available potential energy (APE, Figure 3.3). From 28 October to 9 November, low winds often below 0.2 N. m^{-2} and positive surface heat fluxes enhanced the model and observed ocean stratification. However, the ocean restratification increased at a rate much larger than the simulated stratification, whereby within 1 week (4 November), the strength of the observed stratification more than doubled the model estimate, with *in-situ* N^2_{0-100m} reaching $\sim$3 $\times$ 10^{-5} s^{-2} (Figure 3.7c). From 8 November, the observed stratification was readily reduced from $\sim$3 $\times$ 10^{-5} s^{-2} to almost zero in about one week. The model stratification, albeit much weaker, continued to steadily increase despite wind stress increasing to above 0.8 N. m^{-2} (Figure 3.7c). The overlaid shaded areas in Figure 3.7c represent the various regimes of mixed layer temperature and salinity variations found in Figure 3.3. Interestingly, non-compensated temperature and salinity variations resulted in a rapid increase of the observed stratification, greatly exceeding the model estimates, while compensated variations indicated a well-mixed upper ocean with weak observed stratification (gray shading in Figure 3.7c). At the onset of summer (28 November), the modeled and observed stratification were comparable (N^2_{0-100m} $\sim$2 $\times$ 10^{-5} s^{-2}). Strong heating during summer (> 400 W. m^{-2}) far exceeded cooling of the mixed layer surface, which only fell below 2200 W. m^{-2} once in 3 weeks. This resulted in a simultaneous increase of stratification in the model

and observations. From 23 December, a series of storms with elevated wind stress above 0.4 N. m^{-2}, reaching up to 1.2 N. m^{-2} provided sufficient vertical shear-mixing in both the model simulation and the ocean leading to decreased N^2_{0-100m} by 1×10^{-5} s^{-2} in the model and 2×10^{-5} s^{-2} in ocean observations. The freshwater fluxes incorporated in the PWP model influence primarily the summertime stratification. Rainfall in the SAZ occurs periodically with peaks over 6 mm. d^{-1}, reaching up to 12 mm. d^{-1} during the maximum rainfall event. These instantaneous events do not significantly impact the modeled stratification. However, a model simulation with rainfall turned off (not shown) suggests that without rainfall, the summer stratification would be weaker than what the model and glider observations suggest. This could have notable implications for upper ocean stratification should climate variability in rainfall patterns impact precipitation in the SAZ, or if precipitation belts shift meridionally in relation to the Southern Annular Mode (*e.g.* Gillett et al., 2006; Hendon et al., 2014) or other climate modes of variability. To test whether the variability of the observed stratification was a result of the glider moving across gradients of physical properties which exhibit contrasting upper ocean stratification, the model was initiated at three-independent periods throughout the time series. These include prior to the onset of spring restratification, during the period where spring restratification was strongest, and the beginning of summer (not shown). These time were chosen selectively as each one represents contrasting stratification. The stratification for each simulation showed minor differences in magnitude, depending on the strength of the stratification during the model initiation. However, the variability of stratification remained comparable to the model run shown in this work, suggesting that the glider does not sample across horizontal gradients of vertical stratification, and moves at a rate slow enough to capture the evolution of the observed stratification.

Previous work to understand seasonal restratification of the mixed layer has shown that one-dimensional processes may explain springtime increases in stratification such that the onset of seasonal heat gain imparts an immediate shallowing of the MLD, which can be subsequently mixed by a passage of storms acting to vertically homog-

enize the water column (Waniek, 2003). The results shown by the one-dimensional model propose the timing of seasonal restratification in the SAZ can be linked to surface heat, freshwater, and momentum fluxes as stratification goes hand in hand with heating in the late spring. This may have important implications for regions of weak ocean energetics, as is seen in Babu et al. (2004). However, the Southern Ocean is a turbulent environment (Naveira Garabato et al., 2004 fostering well-known frontal regions separating water masses of varying buoyancy characteristics (Orsi et al., 1995) and here we show that shear-driven mixing and entrainment are not solely responsible for the variability of the springtime upper ocean restratification SAZ as the susceptibility of upper ocean stratification to undergo rapid and large variations is under-represented by the model. Therefore, this model experiment provides evidence that our understanding of upper ocean variability in the Southern Ocean requires the implementation of processes not represented in a one-dimensional framework. Our observations were taken in the SAZ south of Africa, where lighter water from the subtropics meets colder, denser water from the Subantarctic-Antarctic. We show this region exhibits various regimes in mixed layer variability. During periods where temperature and salinity do not compensate in their contribution to density, deviations of stratification between the model and observations were greatest. These periods were synonymous with less dense mixed layers and enhanced stratification in the observations (Figure 3.6), whereas the simulated stratification showed a much weaker but more gradual increase with time. Therefore, the results from the PWP model suggest these less dense mixed layer were not solely driven by surface heat fluxes. one-dimensional models cannot be expected to provide complete simulations of Southern Ocean dynamics, as advective fluxes and other three-dimensional processes are important to its upper ocean variability. For example, the PWP model lacks the provision for the vertical displacement of the thermocline due to internal gravity waves and is mainly influenced by bulk and gradient Richardson mixing and not accounting for diffusion occurring between the mixed layer and below (that could still be significant, Nicholson et al., 2016). It is important to understand the processes

which drive these mixed layer changes as they have implicit implications on mixed layer stratification and further biogeochemical responses (Swart et al., 2015). Thus, we propose that the three-dimensional processes not resolved in the model may have large-scale implications across the Southern Ocean where horizontal gradients exist and therefore have a crucial role in explaining the enhanced springtime stratification variability in the Subantarctic Ocean. To investigate the role of submesoscale processes during the seasonal onset of mixed layer restratification, we apply parameterizations developed in numerical studies to estimate the equivalent heat fluxes applied to the mixed layer by submesoscale processes (Fox-Kemper et al., 2008; Mahadevan et al., 2010). We look to scale the potential fluxes imparted by upper ocean instabilities derived by enhanced horizontal buoyancy gradients to explain the departure between our observations and the model.

3.3.5 The impact of submesoscale processes in defining the mixed layer stratification

To better understand the role of submesoscale processes in the seasonal restratification of the SAZ mixed layer, we require observations of the horizontal buoyancy gradients (b_x) sampled between glider dives. It is reasonable to assume the glider sampled the submesoscale as the mean distance between profiles was 1.4 km $\pm$ 0.9 km, well within the typical range of the Rossby radius of deformation (10 km). However, submesoscale processes develop rapidly (within days), and thus we may only observe the result of a process which has already occurred. As the sampling strategy for this experiment was to direct the glider trajectory predominantly eastward to remain in the SAZ, the glider-derived by is a better representation of the meridional-orientated fronts rather than the large zonal fronts of the ACC. Therefore, estimating the equivalent heat fluxes of MLEs and wind-driven surface forcing using a glider may result in over and under-estimations due to variations in the alignment of the glider's path, the front, and the wind direction. Figure 15 of Thompson et al. (2016) estimates the EBF using all possible angles of the glider dive, wind orientation, and horizontal buoyancy gradient. They show that Q_{EBF} will represent almost all, or very little of the actual

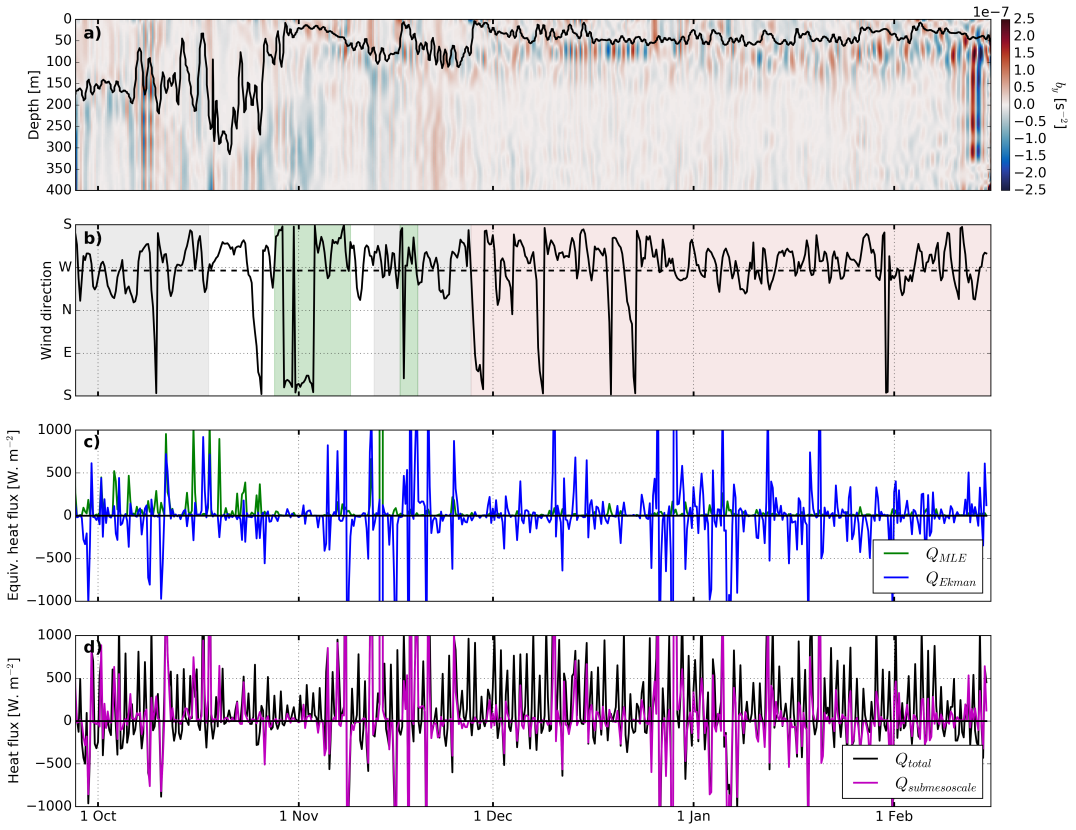

Figure 3.8: (a) Glider observed horizontal buoyancy gradients denoted on the figure as b_y (s^{-2}; color) with mixed layer depth overlaid with a black line. (b) Wind direction obtained at each wind measurement. Shaded areas are as in Figure 3.3. (c) Equivalent heat flux values of Q_{Ekman}, denoted on the figure as Q_{Ekman} (blue line) and Q_{MLE} (green line) indicate the competition between wind-driven EBF and mixed layer eddies. (c) Equivalent heat flux values of $Q_{submesoscale}$ (the sum of Q_{Ekman} and Q_{MLE}), and the combined total of all three fluxes (black line).

equivalent heat fluxes depending on the orientation of the wind, the glider's path, and the front. However, the root-mean-square of observed EBF to the actual EBF is 0.71, indicating that throughout a season, our estimation of submesoscale fluxes is likely to result in an underestimation of the effects of Q_{MLE} and Q_{EBF} on the mixed layer stratification. The meridional direction of each glider dive continually varied during this experiment. Thus, the sign of the horizontal buoyancy gradients sampled is likely to have arbitrary orientation depending on the direction of the dive. This

complication is important when considering front-wind orientation. Therefore, the sign of b_x was modified to represent the meridional orientation of the front. Fronts with lighter water to the north were made positive. Albeit the dominant sampling direction was eastward, the sign of the zonal component of the fronts was chosen to be modified as opposed to the meridional component owing to the wind direction being dominated by the westerlies. This makes it possible to elucidate whether the wind direction was orientated up or down the submesoscale front. For example, a westerly wind with a positive by indicates a down-front wind. We acknowledge this may not provide exact down or up-front wind orientation as meridional-orientated fronts will be underestimated and EBF overestimated, however, it provides some clarity of the direction of the front in relation to the dominant zonal wind orientation. Finally, the impacts of changes in wind stress and wind direction on upper ocean stratification are provided. The time series of glider estimated by along its path is shown in Figure 3.8a. Weaker mixed layer horizontal buoyancy gradients ($b_x < 0.5 \times 10^{-7}$ s^{-2}) were observed during the first month of the time series, particularly when the mixed layer was deep (> 200 m). Meanwhile, within shallow mixed layers (< 100 m) during spring, periodic fluctuations of enhanced horizontal buoyancy gradients were observed ($b_x > 0.5 \times 10^{-7}$ s^{-2}). During spring, these were often far-reaching, extending down to 400 m. However, during summer, elevated by at the base of the mixed layer was limited to the depth of the pycnocline. This is likely an artifact of an internal wave process vertically displacing the pycnocline and the glider sampling as a function of space and time (Thompson et al., 2016).

Equivalent heat flux estimates of Q_{EBF} and Q_{MLE} are calculated by Eq 3.2 and 3.1, respectively, and are depicted in Figure 3.8c. Q_{MLE} is observed to be largest during the spring when the MLD is deeper than 100 m, with periodic spikes up to 1000 W. m^{-2}. These MLE fluxes are representative of the horizontal buoyancy gradient sampled by the glider's path, therefore, it is likely that these by values are underestimated and that Q_{MLE} is higher in reality. As the periods of restratification exhibited shallow MLDs (<100 m), estimates of Q_{MLE} were weak (<200 W. m^{-2}). As such, values of

Q_{MLE} after the springtime restratification were weak and the effects of MLE negligible. Although large periodic fluxes of Q_{MLE} occurring during deep MLDs suggest they may be important in enhancing the stratification, the onset of restratification occurred as the wind direction changed from a predominantly westerly wind during the initial month of the time series, to southerly wind persisting for a number of days (Figure 3.8b). Synonymously, the wind stress weakened to below 0.2 N. m^{-2} while Q_{EBF} reduced to < 100 W. m^{-2}. Mahadevan et al. (2012) provide a ratio of buoyancy fluxes due to down-front winds and MLEs by $R = \frac{\tau^y}{C_e \rho_0 b_x H^2}$, where τ_y is the down-front wind stress, H is the MLD and C_e = 0.06. Where R=1, the effects of restratification by MLEs and destratification by EBF equally oppose each other. For typical spring value of b_x = 10^{-7} s^{-2} with a MLD of 150 m, τ^y corresponds to 0.14 N. m^{-2}. The wind reversal and subsequent weakening of the wind stress toward the end of October satisfy these conditions which allow restratification of the mixed layer by MLEs. A successive passage of storms from early November (Figure 3.7b) enhanced the down-front winds (> 0.4 N. m^{-2}) to generate intense negative Q_{EBF} larger than -1000 W. m^{-2}, providing conditions whereby EBF dominated the restratification by MLEs and surface heat fluxes (Figure 3.8d). The mixed layer subsequently deepened from 20 m to 150 m over six days of down-front persistent winds (Figure 3.8a). This resulted in the eradication of N^2_{0-100m} in the observations which were not explained by shear-driven mixing alone (Figure 3.7c).

In our observations, the springtime restratification rapidly shoals the mixed layer from > 200 m to < 100 m within a few days. Before this restratification, the equivalent heat flux by submesoscale processes (combination of Q_{MLE} and Q_{EBF}) approached 1000 W. m^{-2} at times (Figure 3.8d), dominating the contribution to the combination of surface heat fluxes and equivalent submesoscale fluxes (Figure 3.8c). During down-front winds, EBF dominates the restratifying flux by MLEs. However, weakening winds during wind reversals away from the nominally down-front wind conditions allow MLEs to dominate. The high values of horizontal buoyancy gradients and deep MLDs before the spring restratification of the mixed layer implicate that MLEs may

provide an important mechanism to support the seasonal restratification of the mixed layer. We expect values of Q_{MLE} to be greater during winter, due to deeper mixed layers enhancing the APE in the mixed layer (Callies et al., 2015; Thompson et al., 2016). A full seasonal cycle (winter-summer) would present more information to understand the presence of submesoscale flows in the Southern Ocean. Our observations agree with those of Mahadevan et al. (2012), where MLEs are potentially crucial during springtime restratification. However, our results indicate that MLEs act in combination with a positive surface heat flux and a weakening of the local wind stress to restratify the upper ocean, while the North Atlantic study focuses primarily on the value of $Q_{surface}$ as the mediator of MLE restratification. Thompson et al. (2016) perform a full seasonal cycle of glider measurements in the North Atlantic, and show that the same submesoscale processes shown here can reverse the sign of heat fluxes up to 25% of the time during winter, providing a restratification flux which can oppose winter cooling. Although ever-present horizontal buoyancy gradients in the Southern Ocean suggest that submesoscale flows may be prevalent in winter, extreme cooling and strong down-front winds shown in this work may inhibit such flows to undergo mixed layer restratification.

The potentially important role of submesoscale flows in periodically increasing, or decreasing the total net heat flux applied to the Subantarctic mixed layer during the springtime restratification may have far-reaching implications in our understanding of how the open ocean Southern Ocean responds to increased heating and winds. Understanding these processes is fundamental as Swart et al. (2015) indicate that the observed spring restratification is consistent with an increase in primary production. Additionally, strong intraseasonal variability in primary productivity and carbon fluxes has been discussed in a number of recent studies for this region (Thomalla et al., 2011, 2015; Swart et al., 2015; Carranza and Gille, 2015; Monteiro et al., 2015; Nicholson et al., 2016). Thomalla et al. (2011) first showed that large areas of the Southern Ocean experience regional heterogeneity in the seasonal onset of phytoplankton blooms. The sensitivity of submesoscale processes to heating, wind stress, and direction shown

here suggested that they may be important in determining the timing of these blooms and associated CO_2 flux. Although submesoscale processes may only be dominant for just a few weeks during the end of spring, their impacts on upper ocean stratification may have critical implications given the vast extent of the Southern Ocean. Also, the frontal regions of the Southern Ocean are prone to stronger horizontal buoyancy gradients, and thus submesoscale flows may be augmented throughout other periods of the seasonal cycle for these areas. Additionally, Q_{EBF} can reverse the sign of the net surface heat flux into the mixed layer from a positive to a negative during strong down-front winds (Figure 3.8d), which may provide an additional mixing dynamic to one-dimensional shear-driven mixing. Considering the huge uptake of CO_2 by the Southern Ocean as a result of primary production, it is vital that we fully understand these processes over a full seasonal cycle, especially in the interest of parameterizations in climate models.

Future development of this work will look to implement three-dimensional modeling suitable for the SAZ to enhance our understanding of the evolutionary processes that develop between MLE, along-front winds and heating/cooling where the influence of these processes on net seasonal primary productivity and associated carbon cycling are likely to be significant. Furthermore, full annual observations (winter to summer; presented in Chapter 4) will help to explain the seasonality of submesoscale processes in the Southern Ocean and their associated impacts on the mixed layer variability.

3.4 Conclusions

In this study, we applied five months of high-resolution ocean glider data from the SAZ to investigate the processes that determine the transition from a weakly stratified upper ocean during the springtime to a strongly stratified shallow mixed layer environment in summer. Simulations from a one-dimensional mixing model indicate that one-dimensional fluxes of heat, freshwater, and momentum can explain the timing of seasonal restratification. However, one-dimensional fluxes alone cannot explain the observed magnitude and variability of the springtime restratification. The glider

data show the presence of strong submesoscale buoyancy fronts within the mixed layer during spring. Under weak down-front winds or up-front wind reversals, in the presence of submesoscale buoyancy fronts and deep mixed layers, the mixed layer is conducive to restratification by MLEs. This timing of enhanced MLE fluxes can explain the observed variations of stratification that one-dimensional processes cannot. These observations suggest that submesoscale processes play an important role in enhancing the seasonal restratification of the mixed layer, where a separate study using the biogeochemical properties from this dataset show this period to be key in the seasonal increase of primary production (Swart et al., 2015). Future work will focus on understanding the vertical motions between the mixed layer and the ocean interior as this provides crucial information about nutrient transport supporting summer phytoplankton blooms. Additionally, the implementation of three-dimensional numerical simulations applying characteristics of the SAZ will assist to quantify the evolutionary process of submesoscale dynamics and MLEs and their associated impact on biogeochemical cycles in this globally important region.

CHAPTER 4

Southern Ocean seasonal stratification delayed by wind-front interaction at submesoscales

This chapter is submitted for publication as M. du Plessis, S. Swart, I.J. Ansorge, A. Mahadevan and A.F. Thompson (2018) Southern Ocean seasonal stratification delayed by wind-front interaction at submesoscales. J. Phys. Oc.

4.1 Introduction

In the Southern Ocean, the seasonal cycle dominates the mixed layer depth (MLD) variability (Dong et al., 2008; Sallée et al., 2010b). At the ocean surface, buoyancy loss during winter months initiates vertical convection and results in an erosion of the stratification and associated deepening of the mixed layer. Buoyancy gain during spring and summer increases the vertical stratification which shoals the mixed layer to around 50 m all around the Antarctic Circumpolar Current (ACC) (Sallée et al., 2010b). Sub-seasonal variability of the MLD is defined here as vertical excursions occurring within a seasonal timescale (hours to months). Mixed layer deepening at these scales occurs by a form of wind-driven mechanical stirring at the ocean surface. In the Southern Ocean, strong atmospheric storms with winds in excess of 20 m. s^{-1} are associated with synoptic scale frequencies (Yuan et al., 2009). The passage of storms is found to erode the mixed layer stratification and deepen summer mixed layers by as much as 50 m (Swart et al., 2015; Nicholson et al., 2016). These synoptic perturbations of the mixed layer have direct implications for biological processes, where the vertical entrainment of nutrients into the mixed layer from below may sustain phytoplankton production across the summer (Swart et al., 2015; Tagliabue et al., 2014; Carranza and Gille, 2015; Nicholson et al., 2016). Furthermore, vertical entrainment of important gasses such as carbon dioxide has direct implications on the global carbon cycle (Sabine et al., 2004). Despite this clear importance of temporal variations of the mixed layer for biological and physical processes, numerical models fail to accurately simulate the depth and extent of stratification of the Southern Ocean mixed layer. Current simulations of global climate models provide mixed layers which are too shallow and stratified compared to the observations, attributed to excess freshwater at the ocean surface (Sallée et al., 2013a). The simulated over-stratification in the Southern Ocean leads to heat being trapped in the mixed layer resulting in much warmer (3-4 °C) conditions compared to observations.

A significant part of our understanding of mixed layer processes is owed to one-

dimensional forcing mechanisms (Niiler and Kraus, 1977; Price et al., 1978). However, the ocean is impacted by horizontal processes in response to fronts, eddies, and filaments, which can modify upper ocean stratification. These potentially important dynamics can occur at small spatial scales, namely submesoscales, $\mathcal{O}$(1-10 km) (*e.g.* Thomas, 2005; Mahadevan et al., 2010; D'Asaro et al., 2011; Mahadevan et al., 2012; Thompson et al., 2016). One particular submesoscale process is the formation of baroclinic instabilities within the mixed layer (MLI), which form as ageostrophic horizontal shear instabilities off the mesoscale (10 -100 km) frontal flow (Haine and Marshall, 1998; Boccaletti et al., 2007). MLI arise at the mixed layer Rossby radius of deformation, $L = NH/f$, where N is the buoyancy frequency in the mixed layer and H is the MLD. MLI have typical length scales of $L \sim$ 1-10 km and can spin down into submesoscale-sized eddies, referred to as mixed layer eddies (MLE). MLEs can directly impact the mixed layer stratification by rearranging horizontal buoyancy gradients associated with mixed layer fronts (horizontal change in buoyancy over some spatial distance) to vertical stratification through an ageostrophic secondary circulation (ASC) with upwelling on the lighter side of the front and downwelling on the denser side (Fox-Kemper et al., 2008).

Surface winds blowing in the direction of the frontal flow, that is down-front winds, drive a cross-frontal horizontal Ekman advection from the denser side of the front to the lighter side. The cross-frontal flow can force convective instabilities, enhancing mixing through small-scale turbulence, which can increase dissipation within the mixed layer by up to an order of magnitude compared to wind-driven shear mixing (Thomas, 2005; D'Asaro et al., 2011). Conversely, up-front winds (winds directed against the frontal flow) advect the lighter side of the front over the denser side, thus increasing the vertical stratification. This wind-driven Ekman advection at fronts is termed Ekman buoyancy flux (EBF).

Multi-month observational studies sampling at resolutions necessary to resolve submesoscale dynamics in the Southern Ocean are limited given its remoteness and harsh conditions. These lack of observations result in an over-reliance on high-resolution

numerical modeling (Nikurashin et al., 2012; Rosso et al., 2014; Bachman et al., 2017) and relatively short duration ship-based measurements (Rocha et al., 2016; Adams et al., 2017) to tease out the role of submesoscale processes impacting mixed layer stratification. Therefore, long-endurance observational platforms, such as profiling gliders, are becoming a common tool to address the data requirements to observe these fine-scale processes. Gliders have already began to provide quasi-continuous observations in the Southern Ocean at horizontal resolutions of less than 5 km and temporal resolutions of 2-5 hours (Schofield et al., 2010; Thompson et al., 2014; Swart et al., 2015; Schofield et al., 2015; Erickson et al., 2016; Miles et al., 2016; du Plessis et al., 2017; Viglione et al., 2018).

In this paper, we use data acquired from Seagliders over four separate years in the Subantarctic Zone region of the Southern Ocean (SAZ). We attempt to elucidate the roles of MLE and EBF impacting the sub-seasonal and inter-annual variability of the mixed layer stratification. We do this by applying already existing parameterizations which scale MLE and EBF as equivalent heat fluxes. These fluxes are incorporated into a one-dimensional mixed layer model to investigate the potential importance of submesoscale processes impacting the seasonal evolution of stratification. Section 2 describes the field deployments of gliders and supplementary data used. Results from the glider experiments and model simulations are presented in Section 3, while Section 4 comprises the discussion summarized in Section 5.

4.2 Methods

4.2.1 Field campaign and regional setting

Seagliders sample the top 1000 m of the ocean in a V-shaped pattern and have shown to provide an adequate resolution for investigating submesoscale dynamics within the mixed layer (*e.g.* Ruiz et al., 2012; Baird and Ridgway, 2012; Mahadevan et al., 2012; Swart et al., 2015; Todd et al., 2016; Thompson et al., 2016; Erickson et al., 2016; du Plessis et al., 2017; Viglione et al., 2018). The field campaign forms a part of the

Southern Ocean Seasonal Cycle Experiment (SOSCEx, Swart et al., 2012), with the aim to understand the seasonal cycle dynamics of mixed layer characteristics in the Southern Ocean. SOSCEX is organized as follows, a glider is deployed at roughly 43 °S and 8 °E in the SAZ prior to the onset of seasonal restratification of the mixed layer for the seasons of 2012, 2013, 2015 and 2016 (Figure 4.1). All gliders continually sampled the upper ocean within the SAZ for the duration of each experiment before being retrieved in late summer (February/March). The duration of each mission ranges from 3-6 months (Figure 4.2). The deployments are labeled incrementally from SOSCEx1 to SOSCEx4. A note is made that SOSCEx1 was stationed approximately one degree north of SOSCEx2-4.

The horizontal resolution between consecutive profiles is obtained by estimating the direct distance between GPS coordinates at the mid-depth of each profile (nominally 500 m). The 95th percentile of the horizontal separation distance is 3.4 km, with a mean of 1.4 $\pm$ 1.1 km (Figure 4.1b). Following the mixed layer Rossby radius of deformation L, typical values within the SAZ of mixed layer stratification ($N \sim 10^{-2}$ s^{-2}), MLD of 100 m and f (10^{-4} s^{-2}) gives L a value of 1 km, which indicates that the spatial sampling resolution of the gliders should resolve submesoscale the gradients of the SAZ. The definition of the MLD follows the density difference criteria of $\Delta\rho$ = 0.03 kg m^{-3} from a depth 10 m (de Boyer Montégut et al., 2004; Dong et al., 2008).

At the location and time of each glider deployment and retrieval, CTD calibration casts were performed and checked for sensor drift and corrected accordingly, as in Swart et al. (2015). Temperature and salinity data are gridded vertically by depth to 1 m intervals. Bad profiles are manually removed. A moving mean is performed for each profile point over a range of 5 m above and below each data point.

4.2.2 Potential vorticity calculations

A metric to determine the susceptibility of the flow to submesoscale instabilities is the Ertel potential vorticity (q), defined in Eq. 4.1 (Ertel, 1942; Hoskins, 1974):

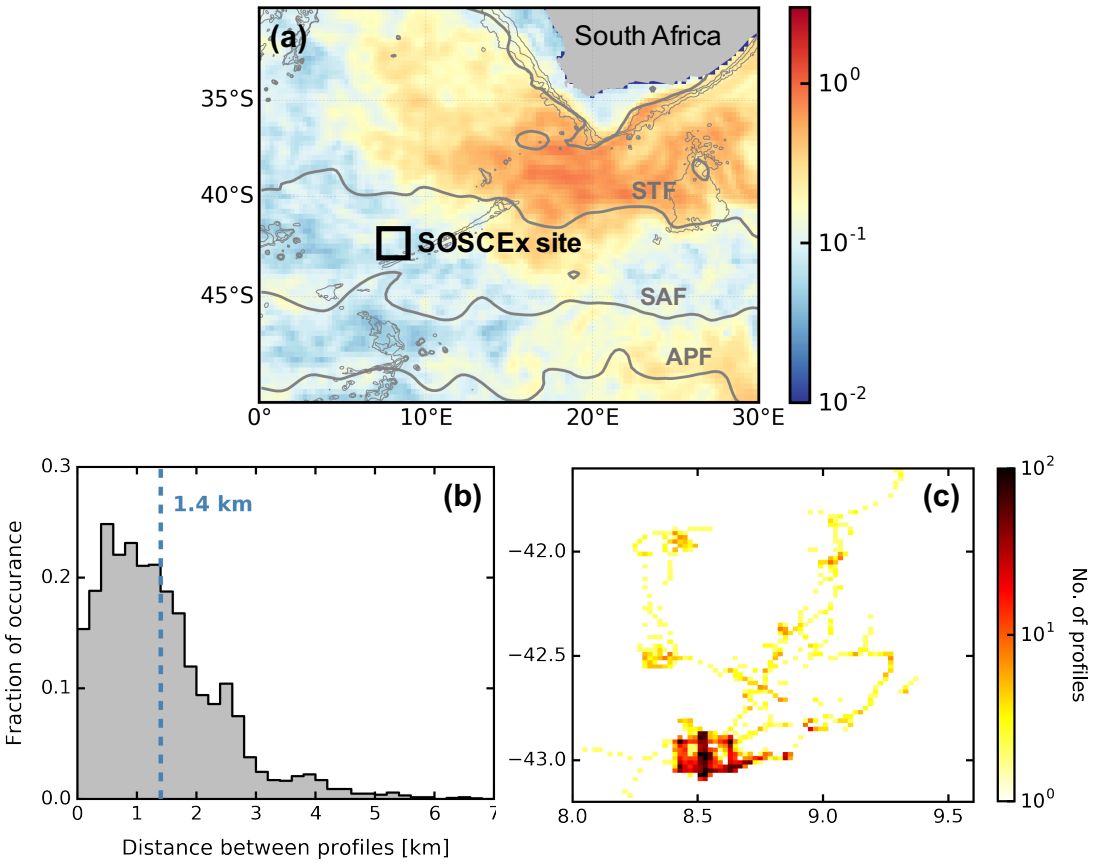

Figure 4.1: (a) Surface eddy kinetic energy ($m^2\ s^{-2}$) over the third Southern Ocean Seasonal Cycle Experiment (SOSCEx) deployment (Jul 2015 - Feb 2016) calculated from the AVISO 0.25° maps. Gray lines on (a) show the positions of the mean large-scale Southern Ocean fronts labeled from north to south as the Subtropical Front (STF), Subantarctic Front (SAF) and Antarctic Polar Front (APF). The fronts are determined from the AVISO absolute dynamic topography as defined in Swart et al. (2010) over the same period as the EKE. Black box shows the location of the four ocean glider deployments occurring between December 2012 and December 2016. The distribution of the distance between the mid-point of consecutive profiles for all deployments is shown in (b), while (c) displays a heat map of the glider surfacing locations for all four deployments.

$$q = \omega_a \cdot \nabla b = (f\hat{k} + \nabla \times U) \cdot \nabla b, \tag{4.1}$$

where ω_a is the vertical component of the absolute vorticity, $b = g(1 - \rho/\rho_0)$ is the

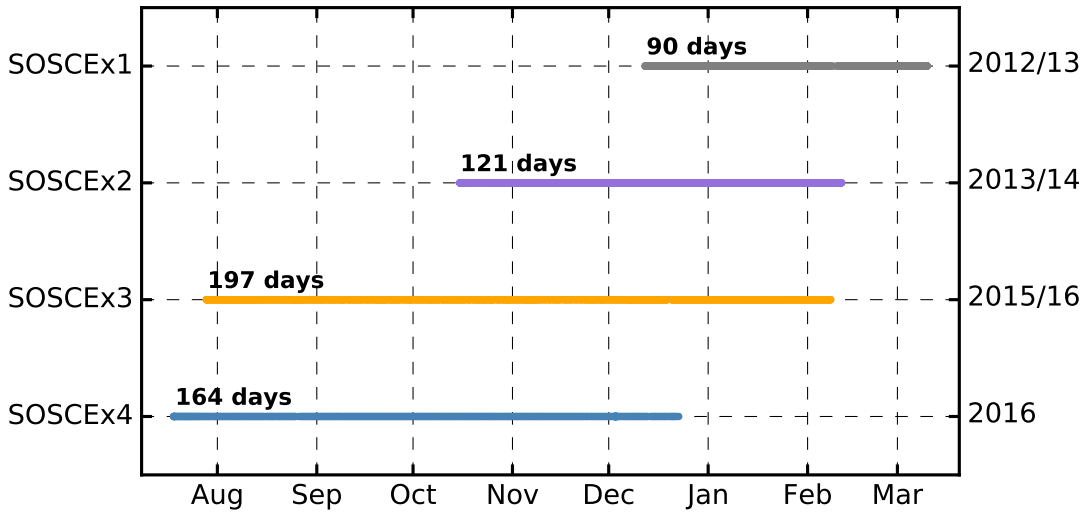

Figure 4.2: The temporal coverage of all Seaglider deployments for the Southern Ocean Seasonal Cycle Experiment. The thick lines show the seasonal glider coverage.

buoyancy and U is the three-dimensional velocity vector (u, v, w). Flow instabilities arise when fq 0, which can occur through variations of vertical vorticity, stratification and vertical shear of the velocity. In particular, unstable stratification (gravitational instability), horizontally sheared flows (centrifugal or inertial instability) or symmetrical instability. Unstable stratification may occur as a result of down-front winds, which are known to extract q from the ocean surface (Thomas, 2005).

In the Southern Ocean, flow instabilities arise when q is positive as f is negative in the Southern Hemisphere. Separating q into vertical and baroclinic components is useful as this helps identify what process may make the flow unstable (Eq. 4.2).

$$q = N^2(f + \zeta) + q_{bc} + q_{nt}, \tag{4.2}$$

The vertical component of q is associated with the vertical component of the absolute vorticity and the vertical stratification shown in Eq. 4.3.

$$q_{vert} = N^2(f + \zeta) \tag{4.3}$$

When horizontal variations in velocity and buoyancy are small, q may be positive (unstable) if the flow is unstably stratified, ($N^2 = b_z$ 0). As the horizontal buoyancy and vorticity gradients become larger, a baroclinic component of the flow, q_{bc}, must be considered,

$$q_{bc} = (w_y - v_z)b_x + (u_z - w_x)b_y, \tag{4.4}$$

where f is the Coriolis parameter, $\zeta = v_x - u_y$ is the vertical relative vorticity and q_{nt} contains the terms related to the non-traditional component of the Coriolis frequency. Estimating q using gliders has successfully been achieved in numerous studies to date (*e.g.* Shcherbina et al., 2013; Thompson et al., 2016; Todd et al., 2016; Erickson et al., 2016; Viglione et al., 2018). These studies have shown that although possible, calculating q using glider data requires the following assumptions: i) We ignore terms in the q calculation that involve the vertical velocity, w, ii) we neglect the q_{nt} term, which only makes a small correction to q, and iii) we assume the flow to be in thermal wind balance, such that the vertically sheared horizontal velocities can be directly related to the horizontal buoyancy gradients (v_z) = $\frac{b_x}{f}$. When these approximations are applied, q_{bc} appears in a more compact form (Eq. 4.5),

$$q_{bc} = -\frac{|\nabla b|^2}{f} \equiv -\frac{M^4}{f}, \tag{4.5}$$

where M^2 is taken as the glider derived horizontal buoyancy gradient b_x. Here x is taken as the distance along the glider path.

Following Thompson et al. (2016), q_{vert} and q_{bc} are combined to provide an observational expression for q using glider data,

$$q_{obs} = q_{bc} + q_{vert} = (f + \zeta)N^2 - \frac{M^4}{f}. \tag{4.6}$$

This expression makes the contribution of horizontal buoyancy gradients (M^2) to a positive q_{obs} clear, as M^4 is a positive quantity. A complicated term in q_{obs} is ζ, which is an approximation of the vertical relative vorticity calculated from the along-track

gradient in the cross-track velocity (v_x). The dive-averaged current is the vertically-integrated (nominally 0-1000 m) current experienced by the glider between each surfacing location. The dive-averaged current is used as the v to provide an estimate for v_x. Calculating v_x using the dive-averaged current raises an important consideration as gliders sample in two dimensions (x,z) and thus only a two-dimensional approach of the three-dimensional buoyancy and velocity fields are obtained. As such, b_x and v_x are unlikely to represent the full in-situ horizontal buoyancy gradient ∇b and vertical relative vorticity (ζ) fields. The potential impacts of these under-estimations are discussed in the Discussion.

4.2.3 Submesoscale buoyancy fluxes

EKMAN BUOYANCY FLUX

By the Coriolis deflection, winds directed along a front drive a cross-frontal flow of water over the Ekman layer depth (Thomas, 2005; Thomas and Lee, 2005), promoting either mixing (down-front winds) or restratification (up-front winds). The process of EBF can be quantified as an equivalent heat flux comparable directly to surface heat fluxes (Q_{EBF}). Negative values of Q_{EBF} represent a negative buoyancy flux, while positive values denote a positive buoyancy flux with units of W. m^{-2}. The equation for Q_{EBF} is shown in Chapter 3, Eq. 3.2. To estimate Q_{EBF}, knowledge of the along-front component of the wind stress, τ^y, is required. The dive-averaged current provides the frontal flow direction, while the magnitude and direction of τ is determined from the NCEP Reanalysis-2 10 m at 6-hourly time intervals. τ^y is determined by finding the along-front component of the wind stress. Section 4.2.4 provides further details on the remotely sensed parameters.

MIXED LAYER EDDIES

Mixed layer baroclinic instabilities drive a thermally direct vertical buoyancy flux within the mixed layer by upwelling the lighter side of a front over the denser side. Fox-Kemper et al. (2008) provide a parameterization of MLEs to represent the vertical

rearrangement of buoyancy. Mahadevan et al. (2012) represent this parameterization as an equivalent heat flux (Q_{MLE}), which is dependent on the horizontal buoyancy gradient and the MLD. The equation for Q_{MLE} is shown in Chapter 3, Eq. 3.1. Note that Q_{MLE} always acts as a restratification flux.

4.2.4 Additional datasets/Reanalysis products

At the location of the SOSCEx site, Schmidt et al. (2017) use *in-situ* winds from Wave Glider deployments to show that NCEP Reanalysis-2 winds (NCEP-2, `https://www.esrl.noaa.gov/psd/data/gridded/data.ncep.reanalysis2.html`) provide the highest correlation to *in-situ* observations compared with other gridded wind products. Thomson et al. (2018) use Wave Glider measurements near the Antarctic Peninsula to show a good agreement between the *in-situ* wind direction and the NCEP-2 wind direction. This is despite a spatial resolution of 2.5°. The temporal resolution of the NCEP-2 wind product is at 6 hours. We apply NCEP-2 10 m winds as well as surface heat fluxes (solar, net longwave, latent and sensible) and precipitation.

4.2.5 Model description

The Price-Weller-Pinkel (PWP, Price et al., 1986) bulk mixed layer model is used as a diagnostic tool to elucidate the role of one-dimensional mixing and restratification processes. PWP applies a momentum flux induced by winds, which along with cooling and evaporation contribute to the three types of mixing: i) convective instability, ii) entrainment from the pycnocline and iii) mixing through enhanced vertical current shear. The water column restratifies when the buoyancy flux at the surface is positive, *e.g.* through heating and precipitation. The surface net heat flux ($Q_{surface}$) constitutes shortwave and longwave radiation, as well as latent and sensible heat fluxes. The PWP model is simulated for each SOSCEx deployment (four in total). The first full profile (0-1000 m) provides the initial profile, while the nearest time and location are used to co-locate the momentum and heat fluxes for each simulation. The density difference criteria $\Delta\rho$ = 0.03 kg. m^{-3} defines the MLD for each time step (de Boyer Montégut

et al., 2004).

PWP simulations using the above criteria are referred to as the one-dimensional simulations (PWP_{1D}). We follow the analysis of Viglione et al. (2018) by incorporating Q_{EBF} and Q_{MLE} as direct buoyancy fluxes into the PWP model. We repeat the four simulations described above with the addition of the equivalent heat fluxes. We refer to these simulations as PWP_{SM}. Direct comparisons of the seasonal evolution of stratification between PWP_{1D} and PWP_{SM} is used to diagnose the role of submesoscale processes impacting the seasonal evolution of mixed layer stratification.

4.3 Results

4.3.1 Mixed layer seasonality

Multi-month (ranging mid-winter to late summer) glider deployments over four separate years show an evident seasonal evolution of mixed layer temperature and salinity (Figure 4.3). The mixed layer temperature increases rapidly from winter (8 °C) to summer (11 °C - 12 °C). The largest seasonal temperature range of 4.7 °C (6.7 °C - 11.4 °C) occurs over 147 days between August 2015 to January 2016. This warming equates to a daily average surface heat flux of 146 W. m^{-2} over a mixed layer of 100 m. Seasonal freshening of the mixed layer occurs from December (most prominent in SOSCEx2 and SOSCEx3), where the salinity gradually decreases from around 34.3 psu to 34.1 psu by mid-January. This is likely to be a signature of an equatorward freshwater flux driven by seasonal ice melt (Haumann et al., 2016). There appears to be large (1 °C, 0.2 psu) density-compensating mixed layer temperature and salinity variations occurring over the order of a day/a few km's. These are likely to be nearby water mass features which either flow through the sampling site or are directly crossed by the glider path.

Despite seasonal warming and freshening both reducing the mixed layer density, the change in density is dominated by the warming, as an increase in temperature of 4 °C reduces the density by about four times more than a freshening of 0.2 psu. To

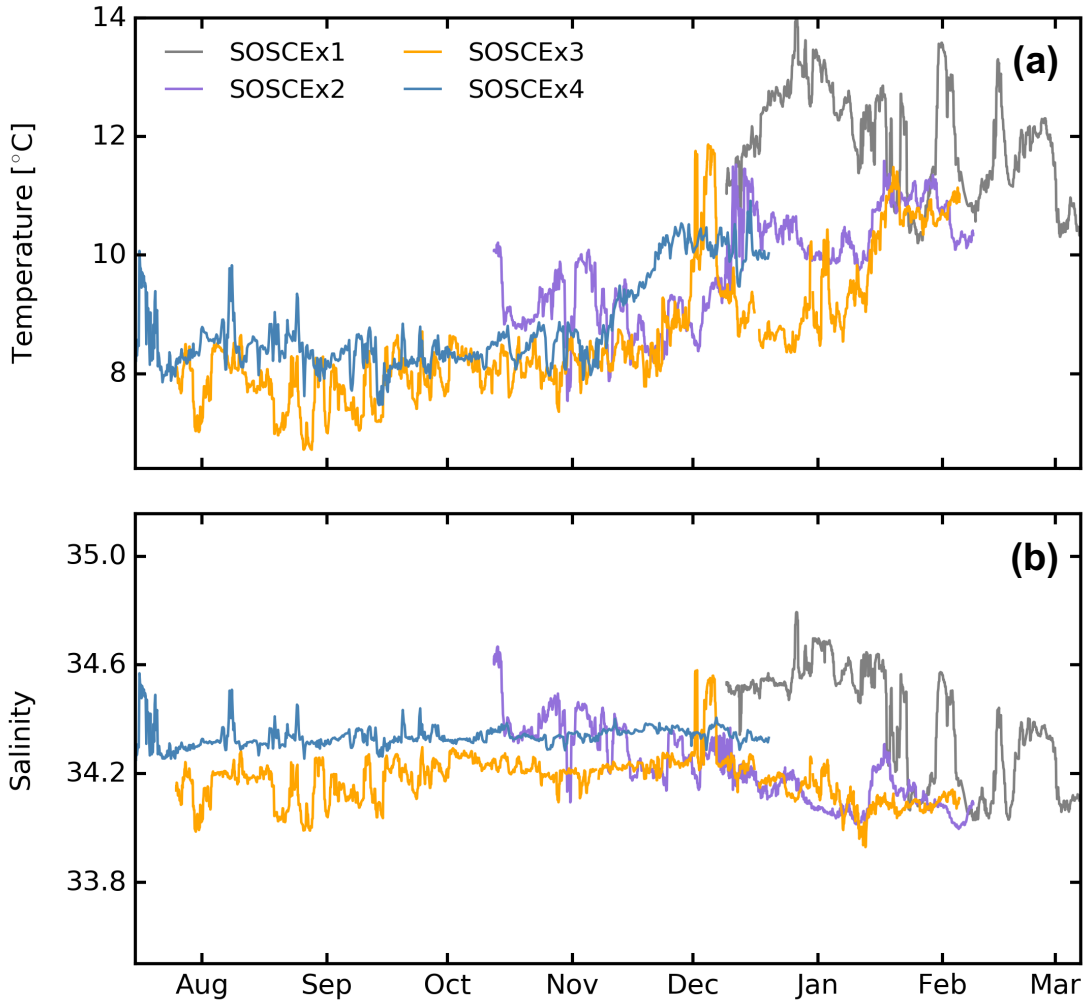

Figure 4.3: Mixed layer temperature (a) and salinity (b) structure observed from the gliders for the four SOSCEx studies. Thermal expansion and haline contraction coefficients α and β scale the ranges of axes proportionally, such that equal displacements in temperature and salinity have an equal effect on density.

quantify the relative effect of horizontal variations in the mixed layer temperature and salinity on density, the density ratio is applied,

$$R = \frac{\alpha \Delta T}{\beta \Delta S}, \tag{4.7}$$

where α and β are the thermal expansion and haline contraction coefficients,

and the horizontal differences of temperature and salinity, ΔT and ΔS, are taken across the spatial interval between consecutive glider dives. For values of $|R| > 1$, horizontal gradients of mixed layer temperature contribute to a larger change in density than salinity. Values of $|R|$ 1 represent the opposite. The median value of monthly compositions of $|R|$ obtains values above 1 for all SOSCEx studies (Figure 4.4). This indicates the tendency for horizontal gradients in temperature to impact density fronts over salinity gradients. The median value of $|R|$ follows a seasonal trend, with the lowest values which are generally closest to 1 in winter (defined here at July/August/Septemeber) when the surface ocean undergoes atmospheric cooling. Values of $|R|$ begin to increase from late winter to reach a seasonal maximum of $|R| =$ 3.6 during November/December before decreasing in late summer.

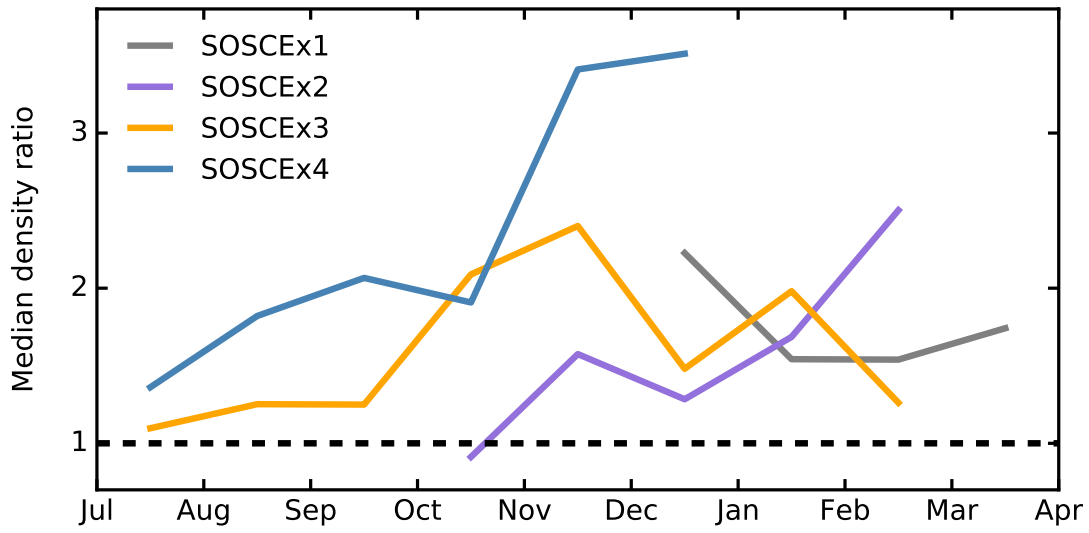

Figure 4.4: Median values of $|R|$ distribution as a function of total monthly values for each of the SOSCEx studies. $R = \alpha\Delta T \; / \; \beta\Delta S$ is computed where ΔT and ΔS represent the change of mixed layer temperature and salinity from daily mean profiles. All datasets are consistent with a seasonal cycle with a maximum $|R|$ in November or December.

A composite of the mixed layer horizontal buoyancy gradients from all four SOSCEx studies show that during the winter months, 45 % of the mixed layer horizontal buoyancy gradients occur above 10^{-8} s^{-2}, but do not exceed 10^{-7} s^{-2} (Figure 4.5). Meanwhile, during spring (October, November, and December) and summer (January,

February, March) when temperature fronts dominate mixed layer density fronts, mixed layer horizontal buoyancy gradients exceeding 10^{-8} s^{-2} occur 67% and 78% of the time, respectively. The strongest fronts (> 10^{-7} s^{-2}) occur during 3% and 8% of the profiles.

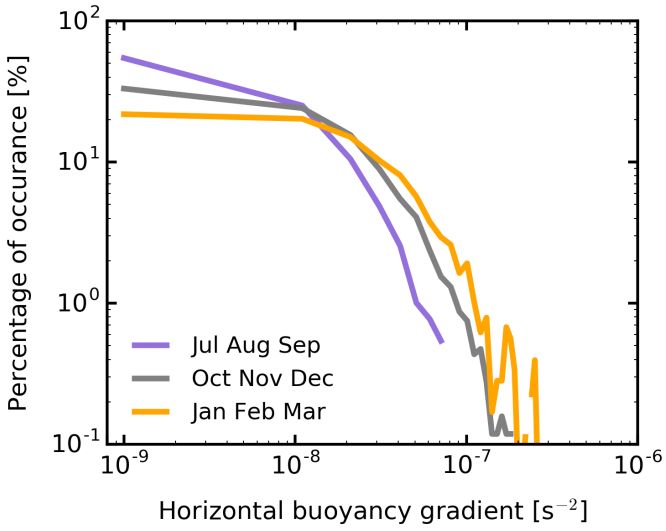

Figure 4.5: Probability distributions of the total seasonal mixed layer horizontal buoyancy gradients b_x calculated from all the SOSCEx glider profiles. Seasons are as follows (JAS: winter, OND: spring, JFM: summer). A seasonal signal exists where weakest horizontal buoyancy gradients occur in winter and strongest in summer.

4.3.2 Seasonality of summer restratification

The temporal evolution of the upper ocean buoyancy frequency and MLD for all SOSCEx studies is shown in Figure 4.6. The mixed layer obtains a maximum depth of 200 m during August and September before shoaling to consistently above 100 m from December. Sub-seasonal scale variations in the MLD are associated with rapid mixed layer restratification (∼50 m per day) via the formation of new stratification within the top 20 m of the ocean ($N^2 \sim 0.3$ x 10^{-5} s^{-2}, *e.g.* SOSCEx3: 25 August, 5 September, 5 November and SOSCEx4: 8 August, 15 August, 4 October). These events are observed 2-3 times per month and can remain for periods from one day up to a week before being eroded.

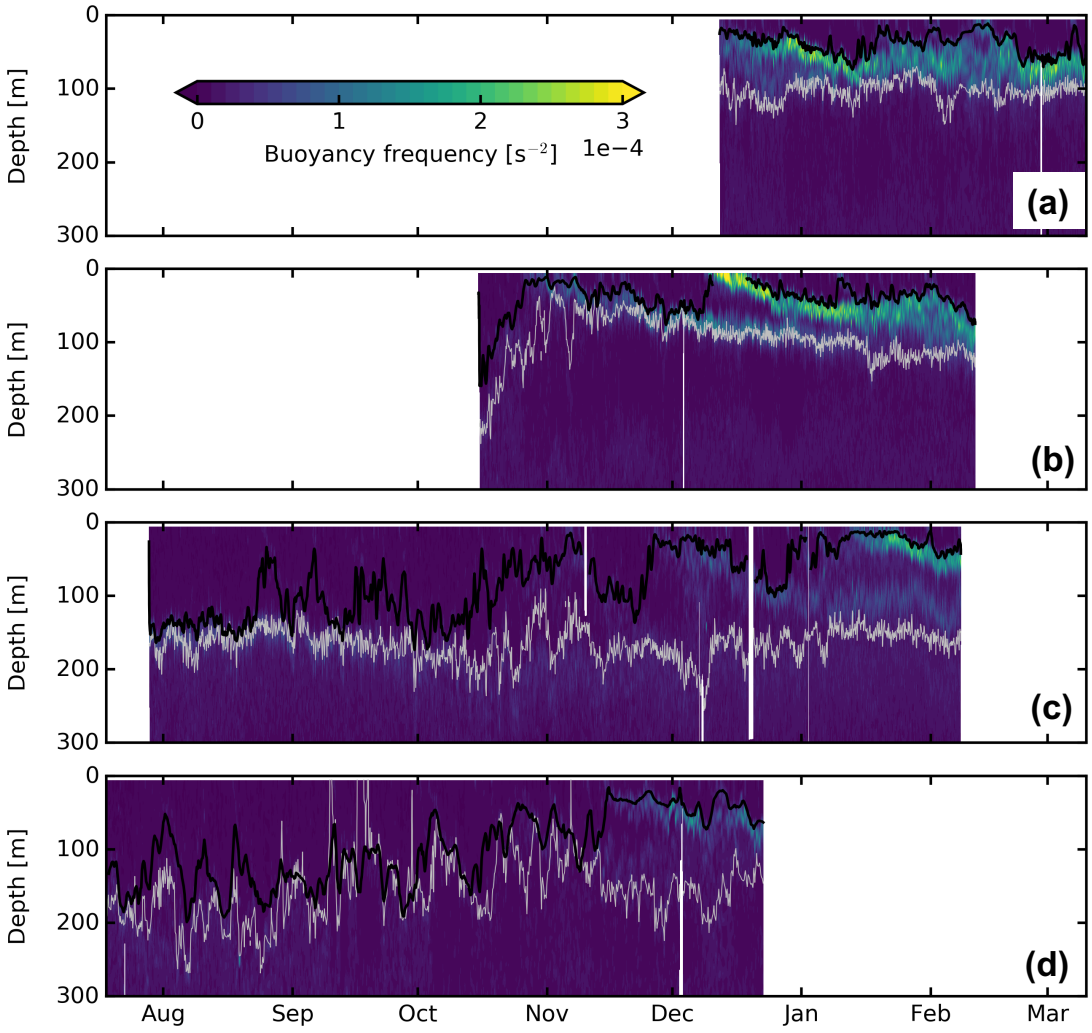

Figure 4.6: Upper ocean section of the seasonal evolution of the vertical stratification in units s^{-2} from the four SOSCEx glider experiments. Blue shading represents weak stratification, while yellow shading shows strong stratification. The black line indicates the mixed layer depth, while gray contour depict the 26.75 kg. m^{-3} isopycnal.

Seasonal restratification is defined by a shoaling of the mixed layer to consistently above 100 m (Figure 4.6). The physical process by which the restratification occurs is through the generation of a new pycnocline at the surface, referred to as the seasonal pycnocline. When initially formed, the seasonal pycnocline is about 100 m above the winter pycnocline, creating multiple layers of stratification in summer. This process is

best observed during SOSCEx3, when the formation of the seasonal pycnocline in late November is superseded at the surface by a second seasonal pycnocline in January to generate three separate layers of stratification within the upper 300 m. Each SOSCEx study displays a similar evolution of the seasonal pycnocline, whereby a seasonal pycnocline is formed at the surface before gradually deepening to around 100 m over the period of a month. In this study, the winter/spring (summer) period is defined as prior to (after) the onset of seasonal restratification.

To objectively determine a seasonal restratification date, N^2 is averaged from the surface to the depth of the 26.65 kg. m^{-3} isopycnal ($\sigma = 26.65$), which resides within the winter pycnocline (Figure 4.7). The seasonal restratification date is determined to be the first day of the period when the mean N^2 above $\sigma = 26.65$, denoted here $\overline{N^2_{\sigma=26.65}}$, is continuously above 10^{-5} s^{-2} for the duration of summer. $\overline{N^2_{\sigma=26.65}} = 10^{-5}$ s^{-2} represents the maximum stratification within the mixed layer during winter, and thus the development of newly formed stratification by buoyancy input above the winter MLD will result in increasing $\overline{N^2_{\sigma=26.65}}$ (Figure 4.7). By this definition, the seasonal restratification dates can only be determined for SOSCEx2 to SOSCEx4 as restratification of the mixed layer occurred prior to the glider deployment for SOSCEx1. The dates of seasonal restratification, shown as vertical bars in Figure 4.7a, for SOSCEx2 to SOSCEx4 are 13 October, 22 November, and 9 November, respectively. This results in 28-day difference of the restratification dates between SOSCEx2 and SOSCEx3.

The onset date of net positive surface heat flux, $Q_{surface}$, corresponds to 13 October for SOSCEx2 and SOSCEx4, and 18 October for SOSCEx3 (Figure 4.7b). By this index, the mixed layer restratifies immediately during SOSCEx 2. Conversely, mixed layer restratification is delayed by 36 and 28 days after the onset of surface warming for SOSCEx3 and SOSCEx4 respectively. Although SOSCEx3 and SOSCEx4 reveal an immediate increase of $\overline{N^2_{\sigma 26.65}} > 10^{-5}$ s^{-2} in response to solar warming ($Q_{surface} > 0$), the stratification subsequently erodes to 10^{-5} s^{-2} on 7 November (SOSCEx3) and 2 November (SOSCEx4) which arrests the seasonal restratification.

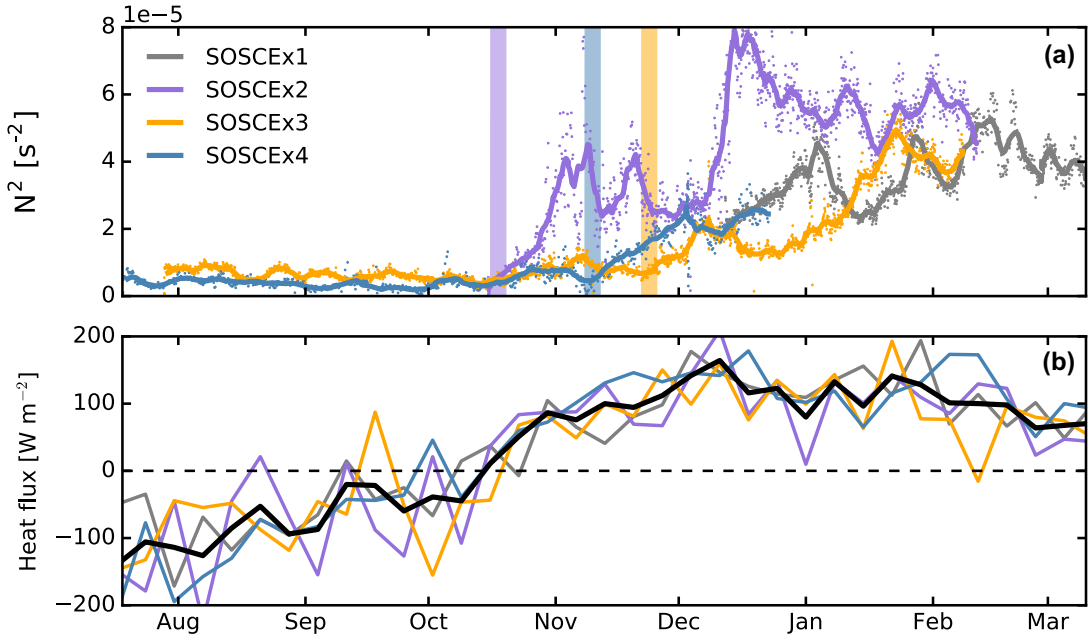

Figure 4.7: (a) The evolution of the mean stratification above the winter mixed layer depth isopycnal (26.75 kg. m^{-3}). (b) Weekly means of the surface heat flux from NCEP-2 for all four SOSCEx studies.

4.3.3 Potential Vorticity structure

We now consider sections of glider-derived potential vorticity (q_{obs}, Eq. 4.6) to investigate the seasonality of flow stability in the upper ocean (Figure 4.8). The seasonal pycnocline is associated with stable potential vorticity ($q_{obs} \sim$ -0.5 $\times$ 10^{-8} s^{-3}). An inter-annual comparison of q_{obs} at the winter MLD indicates that deeper mixed layers (224 m in SOSCEx4, 182 m in SOSCEx3) occur when $q_{obs} \sim$ -0.1 to -0.3 $\times$ 10^{-8} s^{-3}. Within the mixed layer, structure of q_{obs} is largely weak ($q_{obs} \sim$ -10^{-9} s^{-3}) where q_{obs} regularly becomes unstable (positive) when the mixed layer deepens. Sub-seasonal restratification events during winter denoted by rapid mixed layer shoaling are subject to positive q_{obs} within the top 50 m of the water column. These are destroyed within a few days as convective instabilities arise and the mixed layer deepens again.

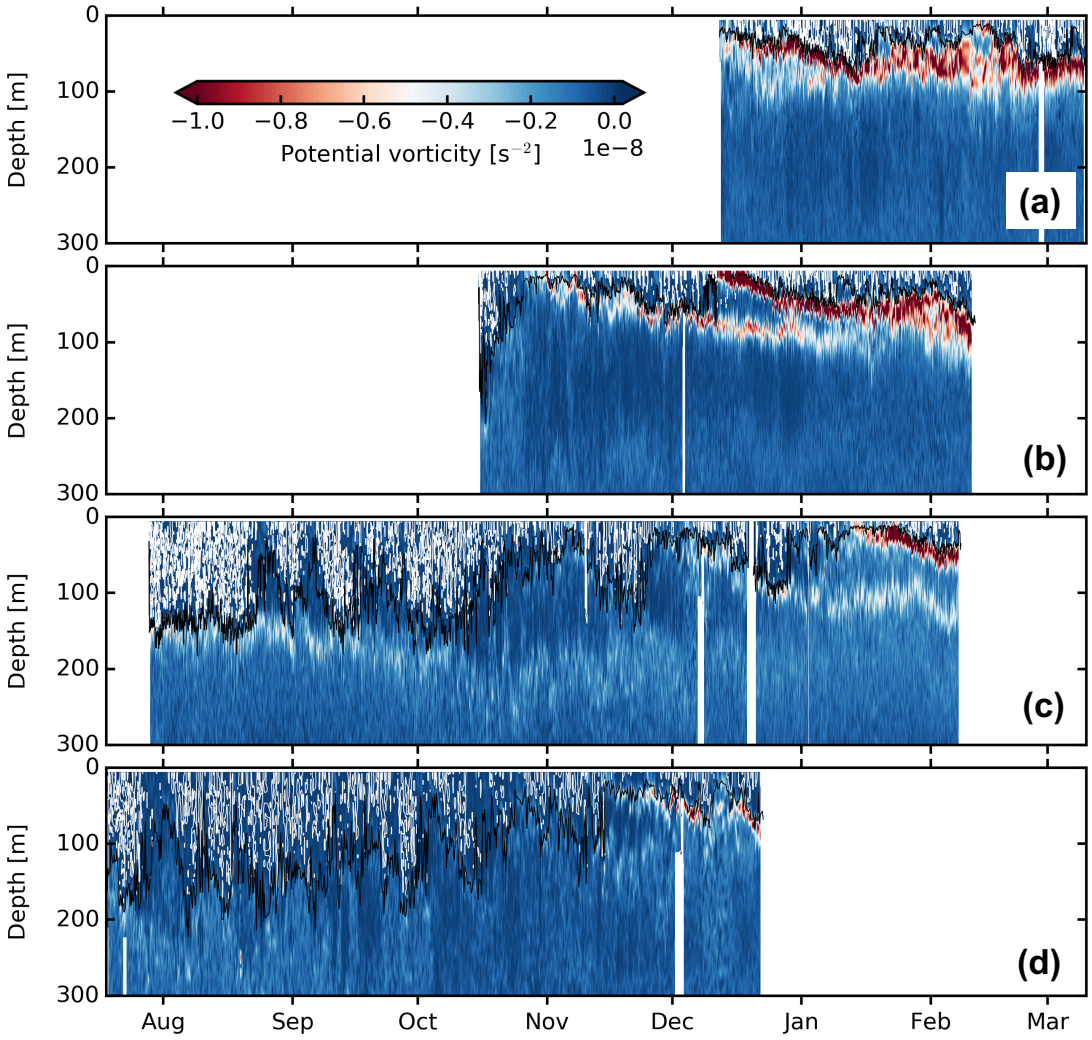

Figure 4.8: Seasonal evolution of the potential vorticity (s^{-3}) derived the four SOSCEx glider experiments. The black line indicates the mixed layer depth. White contours represent instances where the potential vorticity is zero, identifying regions conducive to instabilities.

4.3.4 Submesoscale Instabilities: Wind-Front Interactions and Mixed Layer Baroclinic Instabilities

The estimation of EBF (Eq. 3.2) requires knowledge of the wind-front alignment. For this analysis, the direction of the mixed layer front is taken as the direction of the depth-averaged current acquired from the glider dive cycle (Figure 4.9). In all

four years studied, the frontal flow is predominantly directed between 45° and 90°, observed between 33% and 42% of the time over the experiment. Frontal flow between 0° and 180° (eastward) is observed between 81% (SOSCEx1) and 94% (SOSCEx3), meaning that flow reversals toward the west are most often found during SOSCEx1 (19%) and least often in SOSCEx3 (6%).

The wind direction during the period of SOSCEx is strongly dominant toward the east, occurring 89% of the time during SOSCEx3 and SOSCEx4 and 95% of time during SOSCEx1 (Figure 4.10). In particular, the wind is predominantly toward the east and south-east (between 90° and 135°), accounting for 31% of the wind direction during SOSCEx4 and 42% during SOSCEx1. SOSCEx3 and SOSCEx4 experienced the most westward wind reversals (11%). The coherent alignment of westerly winds and frontal direction toward the east promotes the occurrence of down-front winds. In the following section, we apply existing parameterizations for EBF and MLE to infer the impact of winds and baroclinic instabilities on upper ocean stratification.

Calculating Q_{EBF} requires both the mixed layer horizontal buoyancy gradient and the along-front wind stress (Eq. 3.2). The horizontal buoyancy gradient is achieved by obtaining the spatial distance between the mid-point of each glider profile, while the along-front wind stress is co-located to the time of each profile. The co-located wind stress reveals modulations characteristic of the synoptic scale variability, where wind stress peaks regularly exceed 0.4 N. m^{-2} before relaxing to near zero before the following storm. The peak of each storm is denoted in Figure 4.11, where the mean time difference between peaks is obtained for each experiment. A lowest mean difference between storm peaks of 2.6 days occurred during SOSCEx3 and the highest of 3.2 days during SOSCEx4. The along-front component of the wind stress is shown in Figure 4.11. The dominance of westerly winds at the study site and predominantly westerly orientated front direction results in the along-front wind stress containing a large component of the synoptic storm signal.

Equivalent heat flux estimates of Q_{MLE} and Q_{EBF} are compared directly to the co-located surface heat fluxes ($Q_{surface}$, Figure 4.12). The datasets which contain the

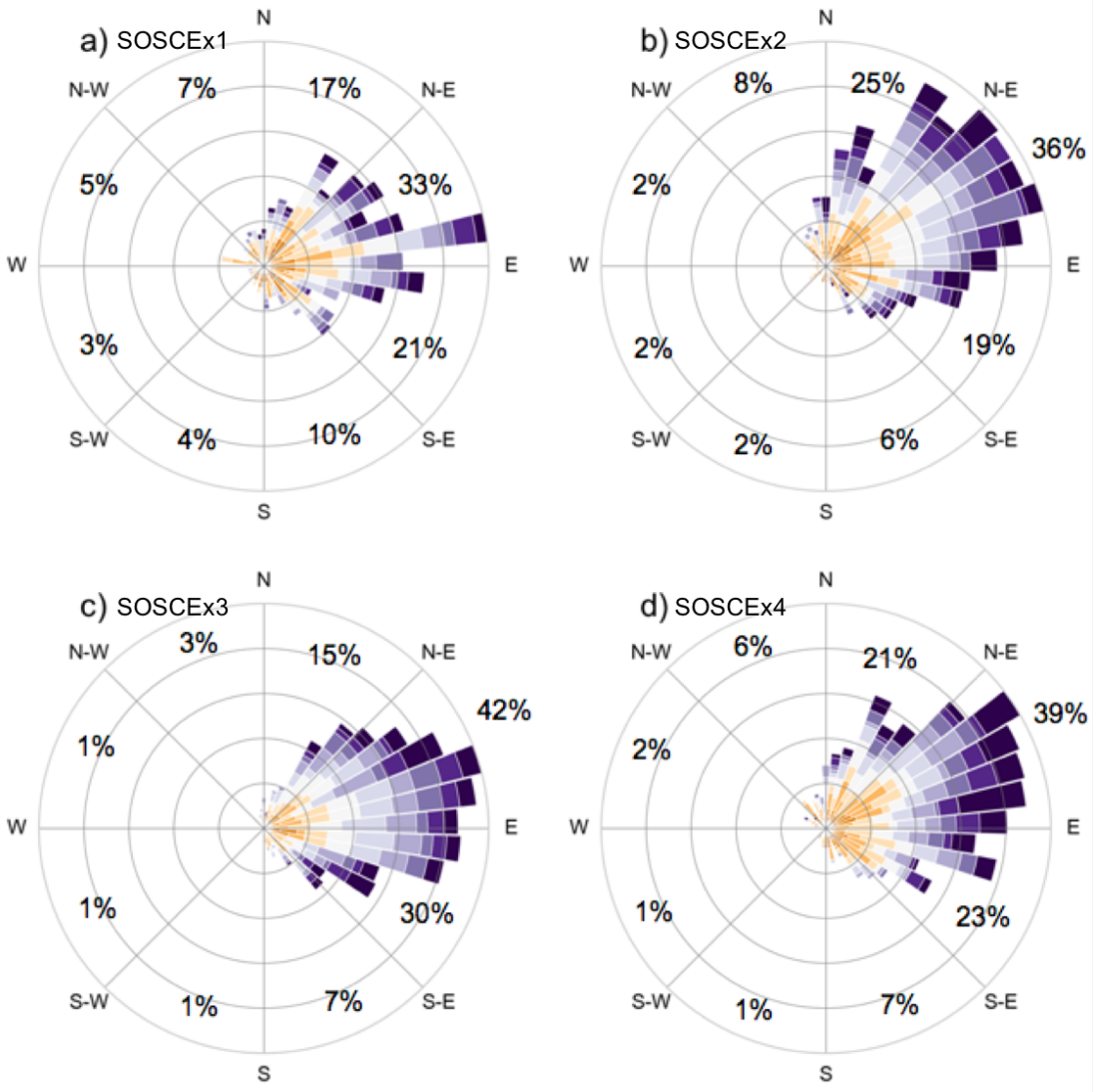

Figure 4.9: Rose plot representing the depth average current acquired at each glider surfacing location. Depth-averaged current vectors infer the direction of fronts used to determine the along front wind component. Colors are an indication of the speed of the front, orange to purple represents low to high current speeds. a - d represents the four Southern Ocean Seasonal Cycle experiments in chronological order.

winter time series (SOSCEx3 and SOSCEx4) reveal the seasonal cycle of $Q_{surface}$, where late winter cooling gradually changes sign, alternating between cooling (∼-200 W. m^{-2}) and warming (∼200 W. m^{-2}) throughout August and September. The temporal variability of Q_{EBF} and Q_{MLE} appear as intermittent spikes, whereby the magnitude

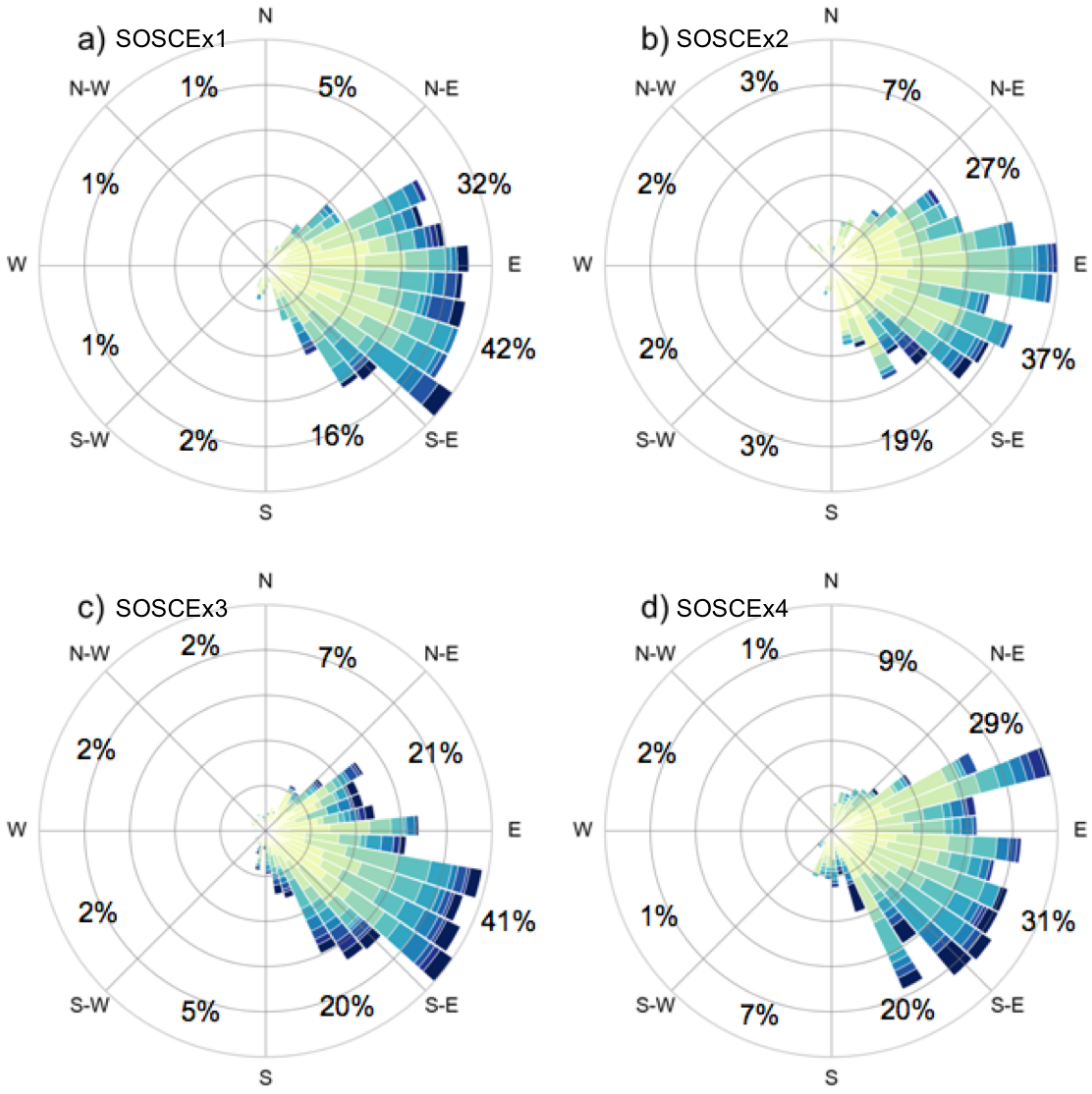

Figure 4.10: Rose plot representing the wind direction acquired at each glider surfacing location. Colors are an indication of the magnitude of wind stress, yellow to blues represents low to high wind stress. a - d represents the four Southern Ocean Seasonal Cycle experiments in chronological order.

of Q_{EBF} regularly exceeds -500 W. m^{-2} throughout spring and summer. Q_{MLE} is comparatively weaker than Q_{EBF} and does not surpass 500 W. m^{-2}. Furthermore, Q_{EBF} undergoes sustained periods (> 1 week) of negative buoyancy flux (-500 W. m^{-2}) which exceeds the amplitude of $Q_{surface}$ and can thereby change the sign of the

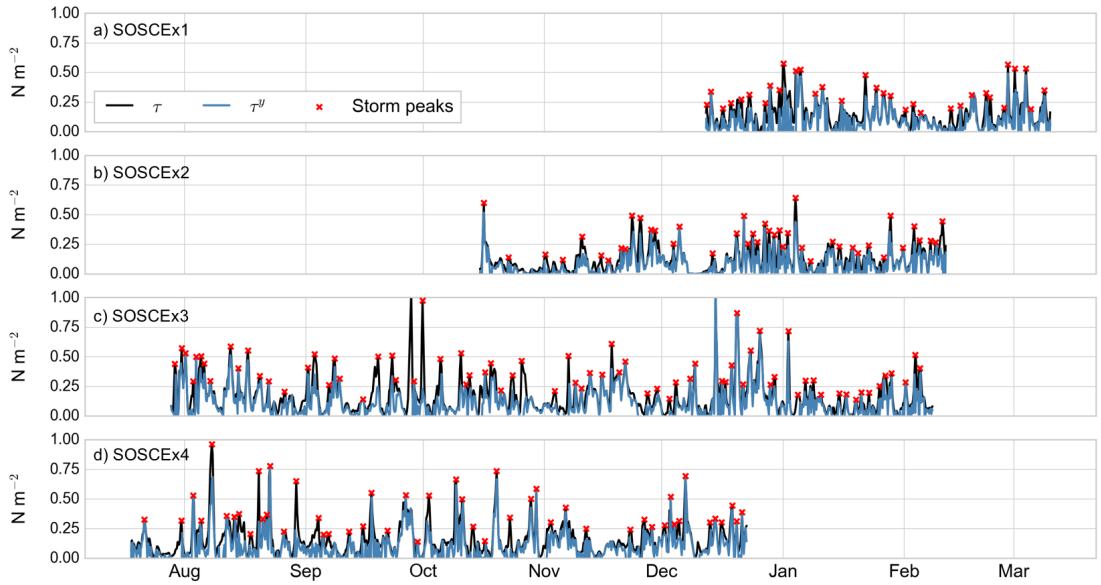

Figure 4.11: Black line shows the co-located NCEP-2 reanalysis wind stress for each glider surfacing location. The blue line is the along-front component of the wind stress while the red crosses show the peaks of the synoptic scale storms. a - d represents the four Southern Ocean Seasonal Cycle experiments in chronological order.

net buoyancy flux. Integrating the three fluxes ($Q_{surface}$ + Q_{EBF} + Q_{MLE}) across each experiment reveals that the contribution of MLE and EBF is to reduce the warming provided by $Q_{surface}$ alone by 53%, 41% and 58% for the first three SOSCEx respectively. For SOSCEx4, cooling by Q_{EBF} results in a net cooling of the mixed layer across the study period.

4.3.5 Model Comparison

The PWP model run for both PWP_{1D} and PWP_{SM} scenarios show an increase in stratification as the season progresses from winter to late summer. Stratification at the end of each PWP_{1D} experiment exceeds 0.25 x 10^{-4} s^{-2}, around double the in-situ stratification estimated by the glider observations. The observed and PWP_{1D} stratification diverge from early October, around the time when $Q_{surface}$ becomes positive. This represents a significant over-stratification of the mixed layer by atmospheric forcing over a seasonal period. The inclusion of Q_{EBF} and Q_{MLE} (PWP_{SM}) reduces the stratification

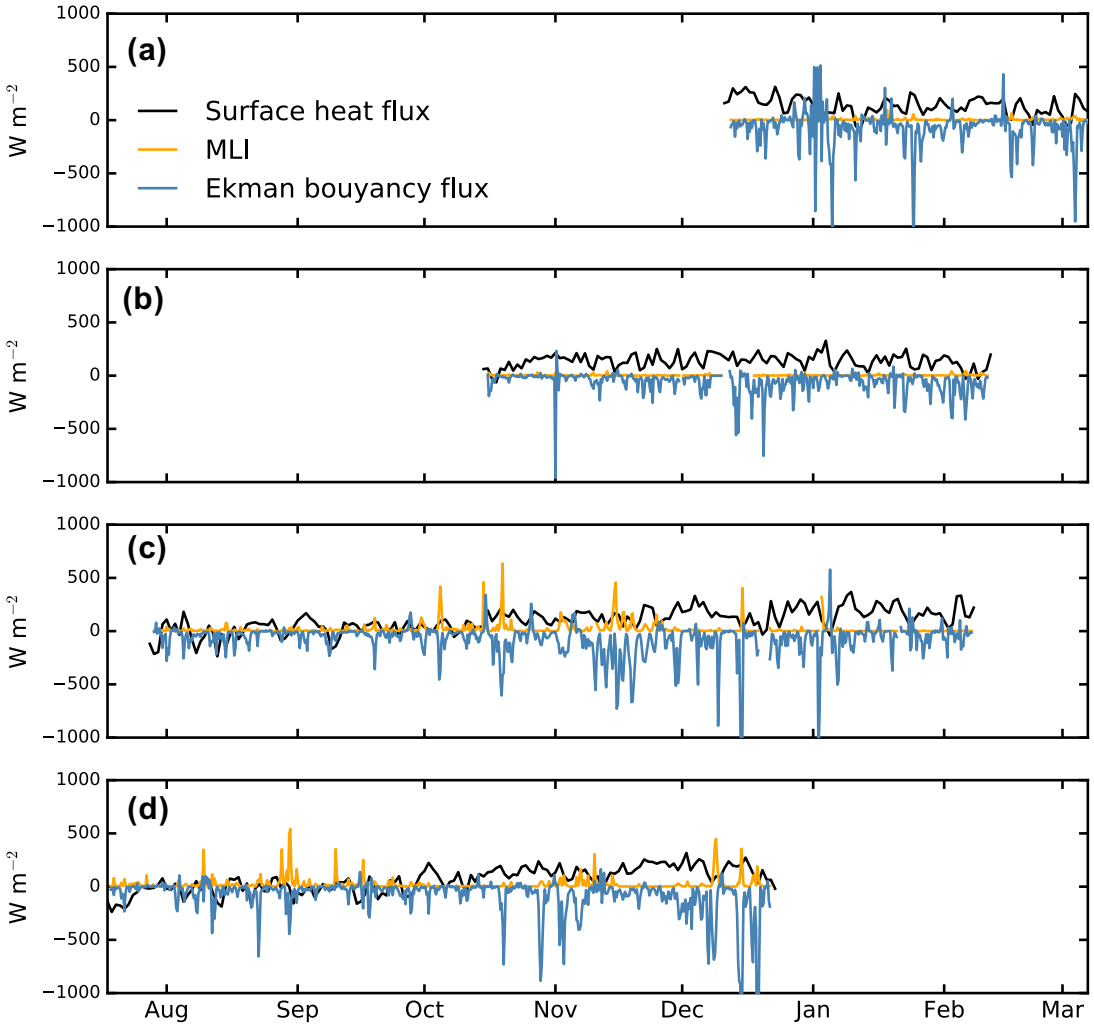

Figure 4.12: Values of submesoscale equivalent heat fluxes by Ekman buoyancy flux (Q_{EBF}, blue line) and mixed layer eddies (Q_{MLE}, red line) for each glider dive. Surface heat flux acquired from NCEP-2 reanalysis (daily) co-located to each glider profile shown by the black line. All units are W. m^{-2}. a - d represents the four Southern Ocean Seasonal Cycle Experiments in chronological order.

by the end of each season such that N^2 is within 10^{-5} s^{-2} during three of the four years studied. The suppression of stratification in PWP$_{\text{SM}}$ is largely attributed to the improved sub-seasonal variability of stratification, particularly during last two years where enhanced negative buoyancy fluxes by Q_{EBF} in PWP$_{\text{SM}}$ generate periodic reductions in stratification coinciding with the observations. This is particularly pertinent

during October and November. The remaining differences in stratification between the PWP_{SM} and the observations may be the result of advective water mass features, which are not included in the PWP simulations (*e.g.* propagating features over the glider).

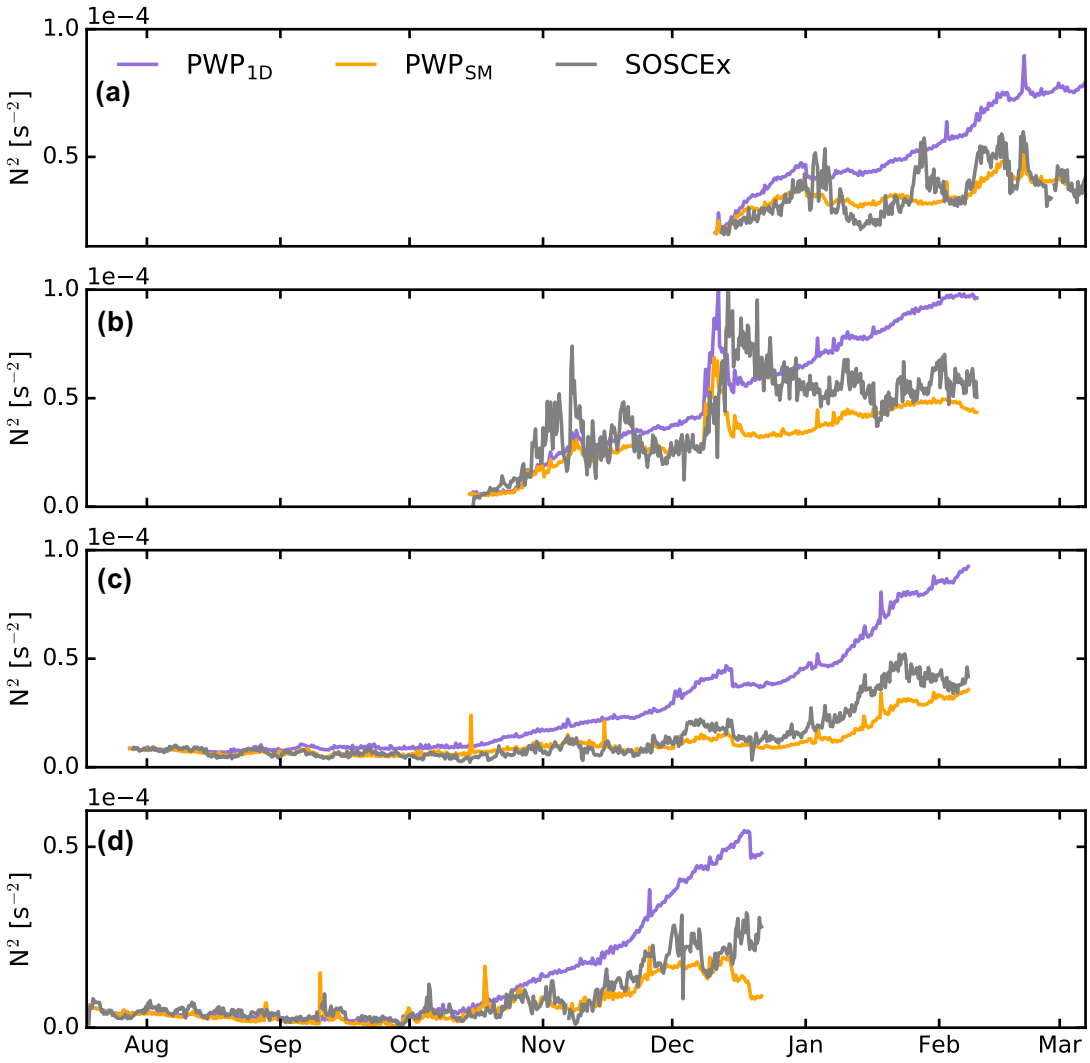

Figure 4.13: The evolution of the mean stratification above the winter mixed layer depth isopycnal (26.75 kg. m^{-3}) for PWP model run using only one-dimensional forcing (blue line), the same run which included submesoscale parameterizations for Q_{MLE} and Q_{EBF} (red line) and the observations gridded to 6-hourly to be comparable to the model (black line). a - d represents the four Southern Ocean Seasonal Cycle experiments in chronological order.

4.4 Discussion

4.4.1 Seasonal cycle of the Subantarctic mixed layer

This study investigates inter-annual variations of the sub-seasonal evolution of stratification using four seasonal cycles of upper ocean glider data from the Subantarctic Zone of the Southern Ocean. Evidence of inter-annual variability in the timing of seasonal mixed layer restratification exists. Two glider deployments occur during the austral winter (August and September) when atmospheric cooling promotes convective instabilities and deep mixed layers (Figure 6b). During this time, periodic events of mixed layer restratification occur across the order of a day, synonymous with the timescale of restratification by baroclinic instabilities (Boccaletti et al., 2007).

The magnitude the mixed layer horizontal buoyancy gradients are generally an order of magnitude weaker than regions of the Southern Ocean preconditioned for strong mesoscale eddy fields (Viglione et al., 2018) and topographical influence (Rosso et al., 2014), but are comparable with the open ocean conditions of the North Atlantic (Thompson et al., 2016). The winter to summer observations of horizontal buoyancy gradients indicates a seasonal cycle, where weaker gradients occur during the winter months. This contrasts the observations from Callies et al. (2015) and Thompson et al. (2016), where horizontal buoyancy gradients are stronger during winter. We associate the strengthening horizontal buoyancy gradients during summer with the seasonal warming and subsequent increase in the contribution of horizontal temperature gradients to density fronts.

Calculations of PV using gliders reveals a seasonality in the role of PV in upper ocean flow. A weak, but stable PV layer forms the winter pycnocline, which is capped by strong stable PV in summer. Weak PV at the base of winter mixed layer limits the maximum seasonal depth of the mixed layer, as a reduction in the strength of this stable PV layer results in deeper mixed layers during one of year studied. These deeper mixed layers will likely impact the vertical transfer of properties at the base of the mixed layer. Furthermore, the weak vertical component of PV associated with

the winter pycnocline may provide an environment whereby an enhanced baroclinic component of PV associated with the presence of mesoscale eddies or filaments can generate conditions suitable for symmetric instabilities (*e.g.* Thomas et al., 2013). This ultimately reveals the importance of stratification within the winter pycnocline, which dominates the vertical component of PV. Preconditioning of the stratification associated with the pycnocline during late summer and autumn may, therefore, be an important dynamic to understand for future work. Full seasonal cycle measurements are required to understanding the precursors for the stratification of the winter pycnocline. The emergence of a strong seasonal pycnocline in the summer produces a stable PV layer, which may likely inhibit the vertical motion across the base of the mixed layer.

The seasonal mixed layer restratification is easily observed by the emergence of stratification from the surface. The observations indicate that the requirement of seasonal restratification is a positive surface heat flux, consistent with the observations of Southern Ocean mixed layer seasonal variability by Dong et al. (2008) and Sallée et al. (2010b). We define the date of seasonal restratification as a continued increase of the mean stratification above the isopycnal which resides at the winter pycnocline. Although the onset of positive surface heat flux does result in increasing stratification, we show that the onset date is highly variable (up to 28 days) between the different years studied. We find that the inter-annual offset of seasonal restratification is due to a transient reduction of the mixed layer stratification throughout the spring. Considering this temporal arrest in seasonal restratification, there is likely to be direct implications for the vertical exchange of properties between the mixed layer and below and therefore the estimation of mixed layer heat budgets (Dong et al., 2007). Furthermore, Swart et al. (2015) show that seasonal mixed layer restratification results in a bloom of biological activity when phytoplankton growth is limited by light exposure, such as is the case in the SAZ. Thomalla et al. (2011) indicate the presence of spatial heterogeneity of phytoplankton bloom initiation dates in the Southern Ocean. We consider that inter-annual variability of mixed layer restratification observed here may partially be responsible for these discrepancies.

4.4.2 Submesoscale impacts on seasonal restratification

Parameterizations of MLE and EBF require information of the mixed layer horizontal buoyancy gradient, the MLD and the along-front wind stress. The horizontal buoyancy gradient and MLD are calculated directly from glider measurements. The along-front wind stress is obtained using the frontal direction inferred by the depth-averaged current and the wind direction. The consistent eastward alignment of winds and upper ocean flow in the SAZ is indicative of a down-front dominant regime. The propagation of cyclonic storms in the Southern Ocean (Yuan et al., 2009) is associated with periods of 4-10 days in the SAZ (Swart et al., 2015). Our observations of peaks in the wind stress corroborate with these estimates. Estimates of a negative buoyancy flux by EBF suggest that the storms drive enhanced down-front Ekman flow, which manifests as enhanced gravitational mixing exceeding the buoyancy input by a positive surface heat flux. In contrast, calculations of MLE for our experiments do not provide a significant contribution to the upper ocean buoyancy flux compared to surface heat flux and EBF. We recognize this may be the result of i) the glider not sampling the fronts perpendicularly and thus underestimating the magnitude of the horizontal buoyancy gradient, ii) baroclinic instabilities spin off the mesoscale horizontal buoyancy gradient, which is unable to be determined as the gliders remain is a localized region and iii) relatively shallow winter mixed layers (150 m - 200 m) and weak horizontal buoyancy gradients (order 10^{-7} s^{-2}) compared to other regions where submesoscales are shown to be active (200 m - 300 m and order 10^{-6} s^{-2} in the Drake Passage, Viglione et al., 2018).

By parameterizing EBF and MLE as buoyancy fluxes into the PWP one-dimensional mixed layer model, the seasonal evolution of stratification within the mixed layer greatly improves compared to when the model is run with surface heat and freshwater fluxes alone. This improvement occurs in two ways. The first is the role of EBF reducing the magnitude of mixed layer stratification to values comparable to the glider observations. The second improvement is the impact of EBF providing sub-seasonal mixing events, providing event scale decreases of the mixed layer stratification which

largely mirror the observations. Periods of unexplained mixed layer stratification variability may be the result of horizontal advection unaccounted for by the model or the glider crossing a frontal feature. Crucially, the timing of mixed layer restratification is improved when using the submesoscale parameterizations.

4.4.3 Implications

The role of down-front wind mixing has been studied in other regions of the global ocean, where D'Asaro et al. (2011) show an enhancement in the rate of energy dissipation of the upper ocean by an order of magnitude. Although these estimates are made in a region of strong mesoscale frontal activity, we show that submesoscale horizontal buoyancy gradients are ubiquitous in the open ocean Southern Ocean. The weaker fronts in observed in the SAZ compared to regions preconditioned for submesoscale activity such as the Drake Passage (Bachman et al., 2017; Viglione et al., 2018) and Kerguelen Plateau (Rosso et al., 2014) suggest that baroclinic instabilities may only act in localized regions of enhanced frontal activity such as mesoscale eddies, fronts, and filaments. However, the continual presence of the horizontal buoyancy gradients in the open ocean Southern Ocean appear to interact with a constantly down-front, intense Southern Ocean wind field which leads to persistent enhanced EBF-induced mixing. This is unlike regions where the flow may be diverted due to topographical influenced and therefore periodically misaligned with the wind field such as the Shackleton Fracture Zone (Viglione et al., 2018). The result is that the persistent EBF in the SAZ may translate to an additional input of turbulence at the surface and a synoptic modulation of the SAZ mixed layer (Nicholson et al., 2016). Furthermore, the delay of seasonal restratification may directly result in inter-annual variability of phytoplankton bloom initiation dates and general bloom heterogeneity observed in the SAZ by Swart et al. (2015) and elsewhere in the Southern Ocean by Thomalla et al. (2011) and Carranza and Gille (2015).

This work forms a part of a growing body of literature which continues to show the presence, and importance of submesoscale processes in the Southern Ocean (*e.g.*

Rosso et al., 2014; Swart et al., 2015; Rocha et al., 2016; Adams et al., 2017; Bachman et al., 2017; Erickson et al., 2016; du Plessis et al., 2017; Viglione et al., 2018). Our observations have shown that for climate models to correctly simulate the seasonal restratification, the wind direction and fronts in the Southern Ocean need to be adequately represented. A further step in improving this field would be to distinguish the discrepancies in the distributions of key submesoscale parameters sampled when using various glider sampling patterns. Furthermore, obtaining an understanding of the relative importance of EBF across the SAZ, or even the entire Southern Ocean would be useful going forward.

4.5 Conclusions

Over four separate years, ocean gliders were deployed in the Subantarctic Zone of the Southern Ocean to investigate the sub-seasonal and inter-seasonal variability of mixed layer stratification. Observational studies, which elucidate the role of submesoscale motions in the Southern Ocean are rare, while those that cover multiple consecutive seasons have not previously existed. The datasets presented here range between winter and late summer, capturing the transition between deep winter mixed layers to strongly stratified, and shallow summer mixed layers. From these valuable datasets the major conclusions are:

1. Horizontal fronts within the mixed layer exhibit strong seasonality and are driven primarily by changes in temperature, which exhibits the strongest influence in early summer. Mixed layer buoyancy gradient are weakest in winter and strongest in summer.

2. Winter to summer glider time series shows that the restratification of the mixed layer can occur up to two months after the onset of seasonal surface heat flux warming. This provides an important observation considering the restratification regulates the exchange of properties between the mixed layer and ocean interior as well as air-sea fluxes and the vertical control of tracer properties important for

biological production.

3. The principle mechanism that delays the onset of restratification is a transient enhancement of submesoscale Ekman buoyancy flux. The conditions which promote EBF are dominant in the Southern Ocean - strong synoptic storms drive down-front winds, which interact with an ocean substrate of prevalent horizontal buoyancy gradients induced by fronts, meandering jets, and eddies.

4. The net effect of EBF on mixed layer stratification is to reduce the seasonal evolution of restratification by about half the amplitude of that generated by the surface heat flux alone using simulations of a one-dimensional bulk mixing model.

This study has shown that the relationship between intense Southern Ocean storms and submesoscale motions may enhance the periodic input of energetic vertical motions and directly impact the production of upper ocean biomass. Therefore, we propose that the effect of submesoscale processes need to be considered when constraining global climate models. The intermittency of these mixing events suggests that this may be difficult to incorporate. Enhanced mixing by EBF may explain part of the inadequacies to represent the Southern ocean MLD in GCMs accurately.

CHAPTER 5

Seasonality of submesoscale flows in the Subantarctic Ocean

This chapter is under preparation for publication as M. du Plessis and S. Swart (2018) Seasonality of submesoscale flows in the Subantarctic.

5.1 Introduction

The mixed layer is a key component of the climate system through which heat, momentum, and gases are exchanged between the ocean and atmosphere. Predictions of climate on seasonal and longer time scales require an accurate depiction of the dynamics which control the mixed layer (Fox-Kemper et al., 2011; Belcher et al., 2012; Sallée et al., 2013b). It is now considered that one-dimensional processes are limited in their ability to explain changes in the mixed layer depth (MLD). Three-dimensional submesoscale flows with scales $\mathcal{O}$(0.1-10 km, hours to days) have now been identified to impact the mixed layer stratification directly. (Haine and Marshall, 1998; Thomas, 2005; Boccaletti et al., 2007; D'Asaro et al., 2011). Studies of the seasonal cycle of submesoscale flows have revealed the key mechanisms that energize submesoscale flows. These have been achieved in both high-resolution modeling efforts (Capet et al., 2008a; Mensa et al., 2013; Sasaki et al., 2014) and observational studies (Callies et al., 2015; Swart et al., 2015; Buckingham et al., 2016; Thompson et al., 2016). These include the circulation due to frontogenesis/frontolysis, mixed layer baroclinic instabilities (MLIs) and frictional forcing driving cross-frontal advection.

MLIs feed off the geostrophic flow, where instabilities result in the rearrangement of horizontal buoyancy gradients to the vertical via an ageostrophic secondary circulation (ASC) associated with large vertical velocities and a release of available potential energy (APE) to kinetic energy (KE). Sasaki et al. (2014) show that MLIs vary seasonally in the North Pacific Ocean due to deep mixed layers holding large amounts of APE, and thereby energizing the submesoscales in winter. They also suggest an inverse energy cascade of KE from the submesoscales toward larger scales. Callies et al. (2015) support the inverse cascade of energy of KE through observational evidence in the western subtropical North Atlantic showing the submesoscale flow is to leading order in geostrophic balance. Mensa et al. (2013) indicate the controlling factor in the occurrence of submesoscales in the Gulf Stream appears to be the mixed layer depth, which controls the reservoir of APE available. Atmospheric forcing is shown to be the

main driver of the enhanced APE indirectly through mixed layer deepening.

Frontogenesis develops from the straining of mesoscale eddies and filaments to increase the density variance, resulting in the strengthening of horizontal buoyancy gradients (Hoskins and Bretherton, 1972). Callies et al. (2015) report frontogenesis to be weak in the subtropical North Atlantic summer. Brannigan et al., 2015 show a weakening of frontogenesis in winter, suggesting that the enhancement of MLIs likely overturn strong horizontal buoyancy gradients when the mixed layer is of sufficient depth.

Frictional forcing driving cross-frontal advection within the mixed layer which can generate overturning convective instabilities for down-front winds termed Ekman buoyancy flux (EBF). Brannigan et al. (2015) show EBF to display a similar seasonality to frontogenesis, with peak values occur in summer.

Most of the studies mentioned above draw their understanding of submesoscale flows and their impacts on mixed layer stratification from ocean configurations or observations of regions characterized by strong surface forcing or regions preconditioned for enhanced frontal activity. Furthermore, studies focusing on the seasonality of submesoscales in the Southern Ocean are either coastal (Capet et al., 2008a) and topographically influenced (Bachman et al., 2017). This work focuses on the seasonality of submesoscales in the open ocean Southern Ocean.

Submesoscale instabilities provide an efficient forward cascade of energy from the large-scale geostrophic flow all the way down to dissipation (Capet et al., 2008b; D'Asaro et al., 2011). Dynamically, the submesoscale regime can be defined for areas of large relative vorticity (ζ), where $Ro = \zeta / f$ is $\mathcal{O}(1)$. The contribution of the relative vorticity in setting Ro determines whether the flow is characterized by ageostrophic flow ($|\zeta| > |f|$), although, submesoscale flows have been found in instances where $Ro < 1$. This definition of submesoscale flow is useful, as it separates from the mesoscale regime where $Ro \ll 1$. Following the criteria, submesoscale flows are characterized by strong horizontal velocity shears. Southern Ocean conditions are often suited to this characteristic due to the abundance of mesoscale eddies, fronts, and filaments.

A useful index to determine the seasonality of submesoscale flows is a negative (positive) skewness of the distribution of the ζ term in the Southern (Northern) Hemisphere. This results in a positive skewness in the distribution of Ro, which has been documented from observations (Rudnick, 2001; Shcherbina et al., 2013; Buckingham et al., 2016) and high-resolution models (Roullet and Klein, 2010; Qiu et al., 2014). Positive skewness in Ro exists due to small perturbations in the flow growing exponentially when the potential vorticity (q) takes the opposite sign of f. Since instabilities in the flow drive fq toward a positive state, the instabilities prevent ζ from growing to large positive (negative) values in the Southern (Northern) Hemisphere. The result is a positively skewed distribution in Ro.

Modeling studies of submesoscale flow in the Southern Ocean have thus far been limited to coastal (Capet et al., 2008a), topographically influenced (Rosso et al., 2014) and strongly energetic regions (Bachman et al., 2017), with good reason, as these regions are expected to have higher submesoscale activity than the open ocean. However, recent results from the North Atlantic have shown that submesoscale processes are particularly active in regions away from topographical influence (Brannigan et al., 2015; Thompson et al., 2016; Buckingham et al., 2016). This chapter aims to extend the understanding of submesoscale seasonality in the open ocean Southern Ocean. This modeling effort focuses on the region south of Africa and particularly the Subantarctic Zone (SAZ). An analysis of the submesoscale field is presented in terms of statistical properties leading to its generation and seasonality. In particular, this chapter looks to characterize the seasonality of the Ro numbers regarding their contribution to submesoscale dynamics. Following this, the mechanisms which contribute to the seasonal evolution of the vertical buoyancy flux, the Ekman buoyancy flux, and frontogenesis is studied. In doing this, the following issues will be addressed:

1. Identifying seasonality of horizontal buoyancy gradients,

2. Demonstrate the seasonality of skewness in the Ro number to determine the intensity of submesoscales,

3. Determine the balance between frontogenetic and baroclinic instabilities,

4. Investigate the indirect role atmospheric forcing has in providing conditions for submesoscale processes to develop.

5.2 Methodology

5.2.1 Numerical model simulation

This chapter makes use of a realistic NEMO simulation (NEMO-SOSCEX36 3.4 configuration) detailed in Table 2.2 in Chapter 2. The spatial resolution is latitudinally dependent, where Δxy is the horizontal grid spacing, which ranges from 1.83 - 2.45 km from the southern to the northern boundaries of the SOSCEX36-NEMO domain. 46 vertical levels are used, while 14 vertical levels make up the top 200 m. The model is atmospherically forced using ERA-Interim reanalysis data on a 3 minute time step, where daily snapshots are saved to output. A complete annual period (1 January 2007 - 31 December 2007) is used for the analysis in this chapter. A regional SAZ sub-domain is defined with boundaries of 40.5 °S - 44.5 °S and 10 °E - 10 °W (Figure 5.1).

5.2.2 Vorticity calculations

The relative vorticity term ζ is estimated as $\zeta = v_x - u_y$, where the subscripts denote the differentials. v and u are the horizontal components of velocity and x and y are the spatial resolution of the model. For the expression $Ro = \zeta / f$, $f = 2\,\Omega\, sin(\lambda)$ was computed using the latitude λ as 43.34° S so as to represent $f = 1 \times 10^{-4}$ s^{-1}. To quantify the seasonality of submesoscale flows within the mixed layer, the skewness quantity of Ro is calculated.

5.2.3 Vertical buoyancy flux

Mixed layer baroclinic instabilities are responsible for the conversion of APE to KE. The release of APE can be quantified in terms of a vertical buoyancy flux $w'b'$, where

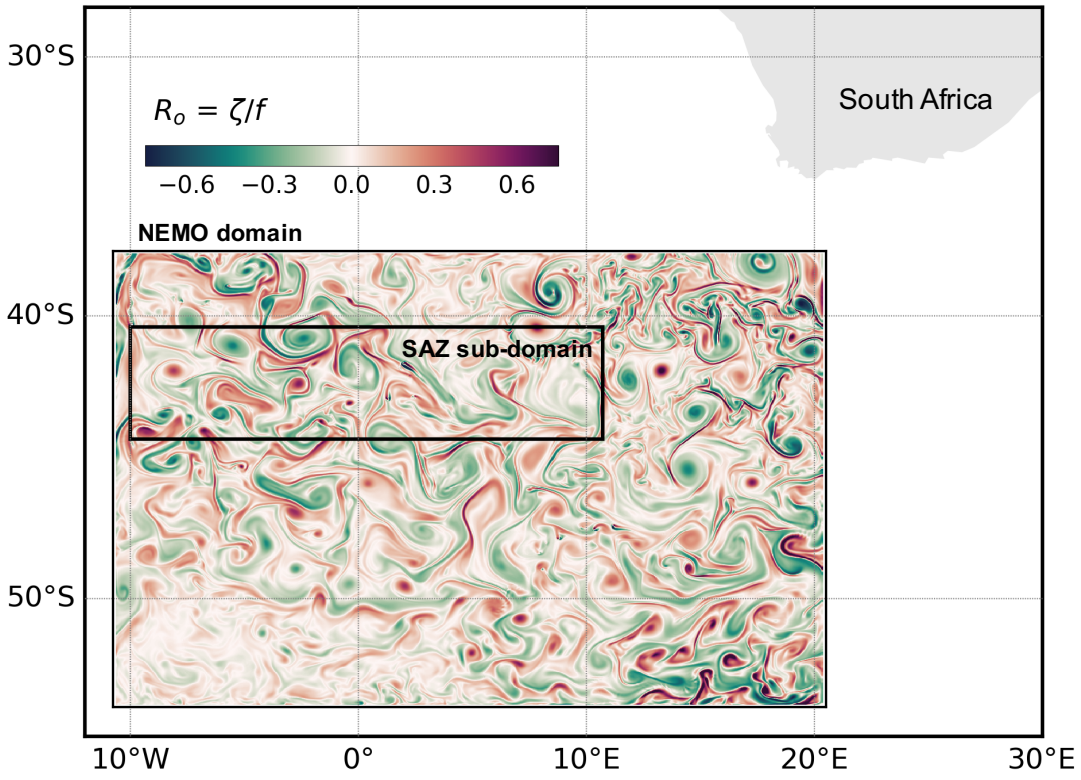

Figure 5.1: Model mixed layer relative vorticity in the Southern Ocean south of Africa for 25 October 2007. The domain 10 °W - 10 °E, 40.5 ° - 44.5 °S represents the SAZ sub-domain that is analyzed in this chapter.

w is the vertical velocity and b is the buoyancy and primes indicate a departure from the mean.

The larger the APE for release, the greater the potential for restratification of the mixed layer. The APE magnitude can be deduced from the Fox-Kemper et al. (2008) parameterization, which scales as:

$$\text{APE} = H^2 |\nabla_h b| \tag{5.1}$$

where H is the mixed layer depth defined as where the density changes by 0.03 kg m^{-3} from a 10 m reference depth (de Boyer Montégut et al., 2004).

To quantify the net release of APE, $w'b'$ is integrated over the MLD and averaged

across the SAZ domain thus obtaining the rate of conversion of APE to KE (Boccaletti et al., 2007; Fox-Kemper et al., 2008; Capet et al., 2008a). We follow Mensa et al. (2013) in defining a potential to KE conversion as:

$$PK = \frac{1}{H} \int_0^H \overline{w'b'}\, dz, \tag{5.2}$$

where w is the vertical velocity, b is the buoyancy, prime denotes deviation from the mean and the overline ($\bar{\cdot}$) represent the averaging across the SAZ domain.

5.2.4 Frontogenesis

Frontogenesis is studied to determine the role of mesoscale stirring generating enhanced submesoscale flows in the mixed layer. Frontogenesis is defined here to be the action by the flow field to increase or decrease the variance of the horizontal buoyancy gradients. The frontogenesis function can describe the role that frontogensis has on the horizontal buoyancy gradients (Hoskins and Bretherton, 1972):

$$F_s = \mathbf{Q}_s \cdot \nabla_h b \tag{5.3}$$

where:

$$\mathbf{Q}_s = -(u_x b_x + v_x b_y + w_x b_z, u_y b_x + v_y b_y + w_y b_z), \tag{5.4}$$

and $|\nabla_h b|$ is the horizontal buoyancy gradient, where ∇ is the gradient operator, h is horizontal components, and b is the buoyancy within the mixed layer.

5.2.5 Ekman buoyancy flux

Frictional forcing at the ocean to atmosphere boundary is an important process at ocean fronts. Cross-frontal flow has shown to be important in driving direct variations in the ocean stratification (Thomas, 2005; Mahadevan et al., 2010; D'Asaro et al., 2011). This process has been the focus of Chapter 4 and is referred to as Ekman buoyancy

flux (EBF), diagnosed as follows:

$$\text{EBF} = (\frac{\tau}{\rho_0 f} \times \mathbf{k}) \cdot \nabla_h b, \tag{5.5}$$

where τ is the wind stress, ρ_0 is a reference density and $\mathbf{k}$ is the unit vertical vector.

5.3 Results

To test the validity of the model derived horizontal buoyancy gradients, the seasonal distribution of horizontal buoyancy gradients from the SAZ sub-domain are compared to the seasonal distribution of horizontal buoyancy gradients from the glider studies of Chapter 4. There are no qualitative discrepancies between the distribution of horizontal buoyancy gradients calculated from within the model mixed layer and the observations.

A snapshot of the model surface relative vorticity field on 1 January 2007 (Figure 5.1) shows large cyclonic and anticyclonic vortices spanning a few degrees in spatial extent throughout the domain. These eddies reveal the presence of mesoscale structures interspersed with a large number of submesoscale features. Elongated filaments and vortices reveal these submesoscale features with *Ro* numbers approaching order 1. The SAZ sub-domain adequately represents occurrences of enhanced *Ro* numbers, demonstrating that this region is susceptible to submesoscale activity.

5.3.1 Surface fluxes

The seasonal cycle of surface heat fluxes that are used to force the model are averaged across the SAZ sub-domain (details in Table 2.2 in Chapter 2) and illustrated as a time series in Figure 5.3a. A clear seasonal cycle of $Q_{surface}$ exists with warming in the summer and cooling during the winter (Figure 5.3a). Surface warming occurs from October - April with magnitudes of the mean across the domain reaching up to 200 W. m^{-2} in January. The cooling winter period spans April - October where surface heat fluxes exceed -200 W. m^{-2} on numerous occasions throughout winter. Figure

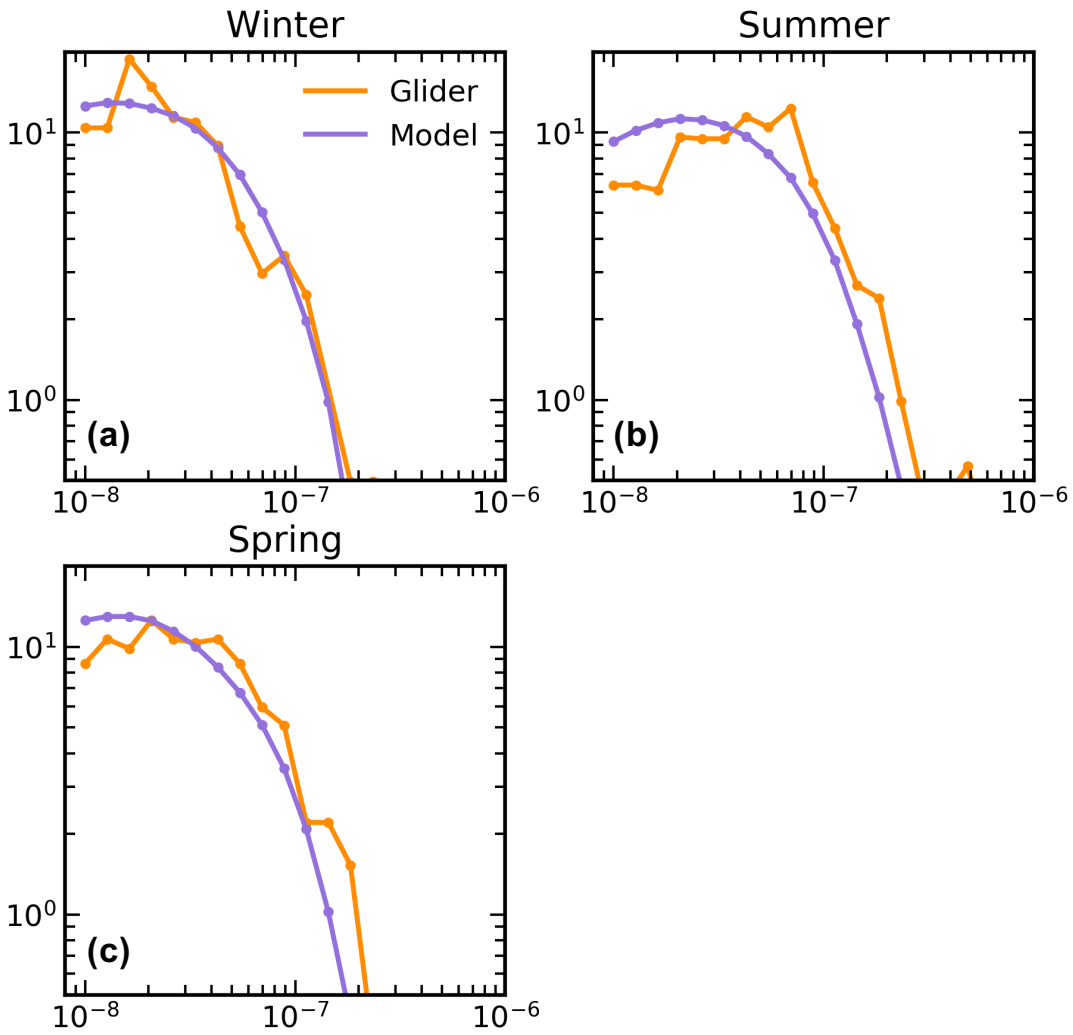

Figure 5.2: Comparisons of the seasonal distribution of mixed layer horizontal buoyancy gradients from 4272 *in-situ* glider measurements (orange) and the NEMO-SOSCEX36 SAZ sub-domain. Seasons are separated in to (a) winter (JJA), (b) spring (SON) and (c) summer (DJB) to correspond to the time series of the glider measurements.

5.3b shows the values of wind stress, illustrating the synoptic variability where an amplitude of about 0.3 N. m^{-2} between low and high wind speed events occur. These results are consistent with the frequency and magnitudes of mid-latitude storms over the Southern Ocean (Yuan et al., 2009) and are in the range of observed values from

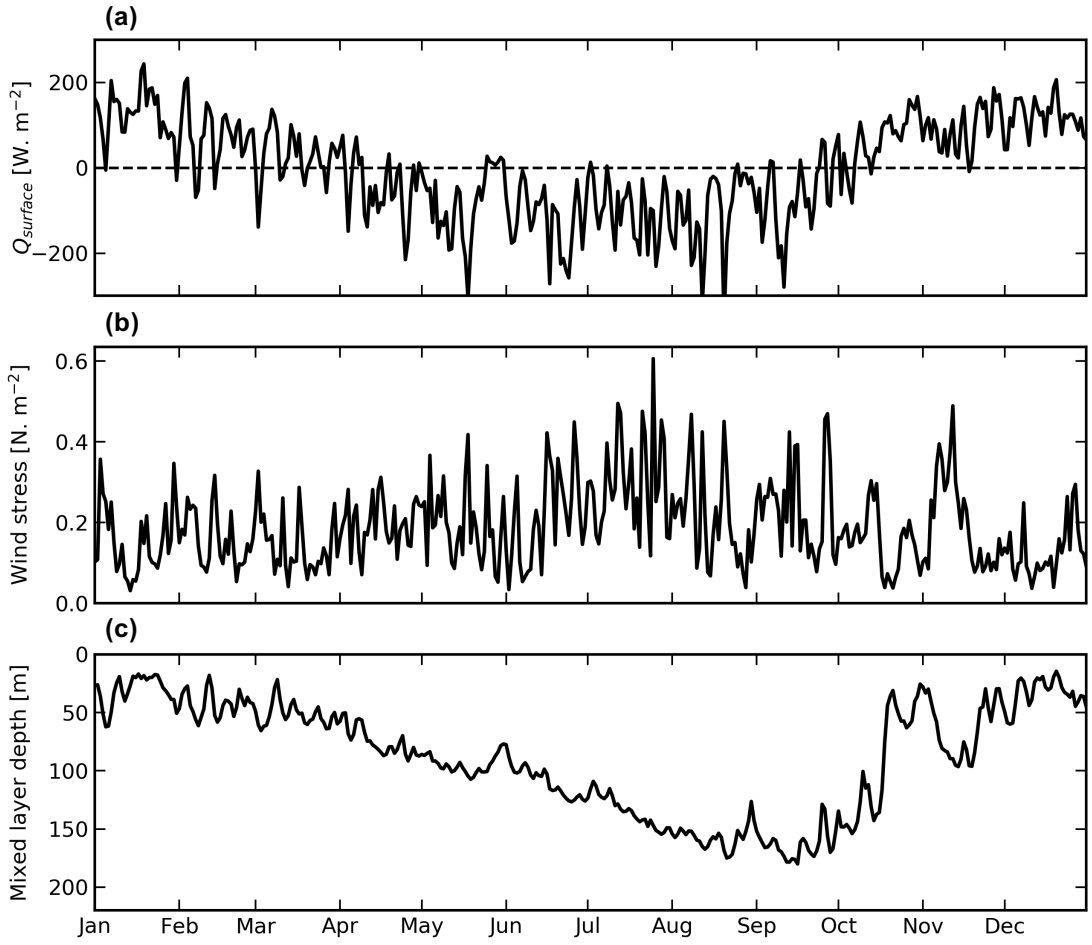

Figure 5.3: (a) Seasonal cycle time series of the mean (a) surface heat flux ($Q_{surface}$, W. m^{-2}), (b) wind stress (τ, N. m^{-2}) and (c) mixed layer depth for the SAZ sub-domain. (a) and (b) are from the ERA-Interim reanalysis product at 24-hourly and 3-hourly temporal resolutions, respectively. Surface and momentum fluxes are used as the atmospheric forcing parameters.

Swart et al. (2015); du Plessis et al. (2017). The mean mixed layer depth (MLD) is at a minimum in December and January with values around 20 m. The mixed layer gradually deepens from February to a maximum MLD of 160 m in September. The seasonal restratification period of the mixed layer reveals a rapid shallowing (> 100 m in a few days) in October and subsequent deepening of > 50 m over a few days during the beginning of November. This variability of the mixed layer is characteristic of the spring observations in the SAZ of Chapters 3 and 4 as well as Swart et al. (2015) and

Little et al. (2018).

5.3.2 Horizontal buoyancy gradients

The model mixed layer horizontal buoyancy gradient is taken at 16 m to be consistently within the mixed layer and averaged across the SAZ sub-domain to provide a full seasonal cycle of M^2 (Figure 5.4). Largest M^2 values exist during the summer season (December - April), where M^2 values approach a seasonal maximum of 5.8 $\times$ 10^{-8} s^{-2} in January. The lowest values of M^2 occur during the end of winter in October, with values around 4 $\times$ 10^{-8} s^{-2}. The 15% percentile of all M^2 values over the SAZ sub-domain is persistently < 1 $\times$ 10^{-8} s^{-2} with a weak seasonal cycle range of 0.5 $\times$ 10^{-8} s^{-2}. Conversely, the 85% percentile of all M^2 values in the SAZ sub-domain reveal enhanced frontal activity during summer. This range of 4 $\times$ 10^{-8} s^{-2} in the 85% percentile of horizontal buoyancy gradients is evidence of a clear seasonal cycle in the generation of mixed layer fronts. Furthermore, this result shows that at the peak of submesoscale activity in summer, the range between the smallest and largest values of M^2 in the SAZ can reach an order of 10^{-7} s^{-2} difference.

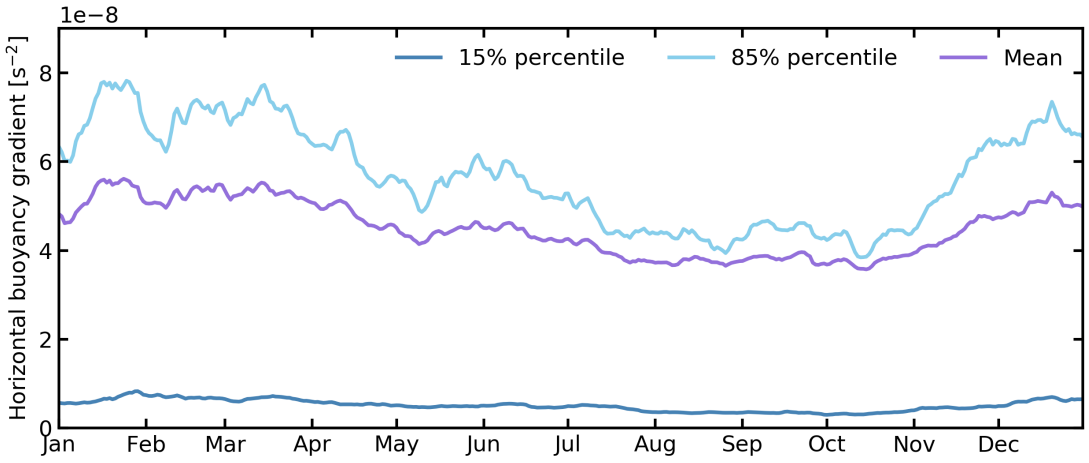

Figure 5.4: Seasonal cycle of the mean (purple), 15% percentile (dark blue) and 85% percentile (light blue) mixed layer horizontal buoyancy gradient ($\overline{M^2}$) for the NEMO-SOSCEX36 simulation across the SAZ sub-domain.

The seasonal cycle of M^2 is coherent with seasonal modulation of the surface heat flux. Horizontal buoyancy gradients begin to strengthen at the start of the heating period in October and nearly double in magnitude by January, reaching a maximum during the same time as the surface heat flux. A deepening of the mixed layer and a shift from warming to cooling in March has an associated decrease in the strength of M^2 until October again.

5.3.3 Skewness in the Rossby number

One of the hallmarks of submesoscale flows is skewness in the distribution of relative vorticity. Figure 5.5 illustrates the normalized distribution of *Ro* numbers calculated within the mixed layer for each of the four seasons.

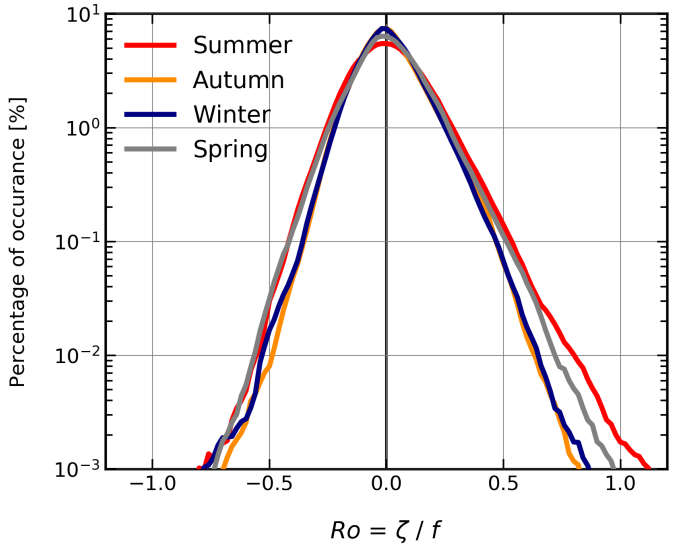

Figure 5.5: Seasonally separated (winter: JJA, spring: SON, summer: DJF, autumn: MAM) distribution of mixed layer *Ro* from the NEMO-SOSCEX36 simulation across the SAZ sub-domain.

The *Ro* numbers appear to be approximately normally distributed in all seasons, where the peak in the distribution occurs at marginally negative *Ro* values. Seasonal discrepancies exist in the frequency of weak positive *Ro*. Lower frequencies of weak *Ro* numbers appear during the spring and summer months, while autumn and winter

indicate a higher frequency of weak *Ro*, where the tail to the right of the histogram ($Ro > 0$) appears to represent higher frequencies of *Ro* values above 0.4 rather than below -0.4. The value of skewness for each seasonal histogram provides a quantitative measure of the seasonal cycle of submesoscale flows. The skewness is similar between all seasons, but largest for autumn and winter at a value of 2.1, while spring (1.9) and summer (1.6) both show the positive skewness associated with submesoscale flows. This result displays a marginal enhancement of submesoscale flows in the winter and autumn.

5.3.4 Vertical advective fluxes

Submesoscale activity in terms of the potential for restratifying instabilities such as baroclinic instabilities (Boccaletti et al., 2007; Fox-Kemper et al., 2008) occurs in regions of enhanced horizontal buoyancy gradients and deep mixed layers. These can be scaled by the APE in the mixed layer. The seasonal cycle of the mean APE within the SAZ sub-domain is displayed in Figure 5.6.

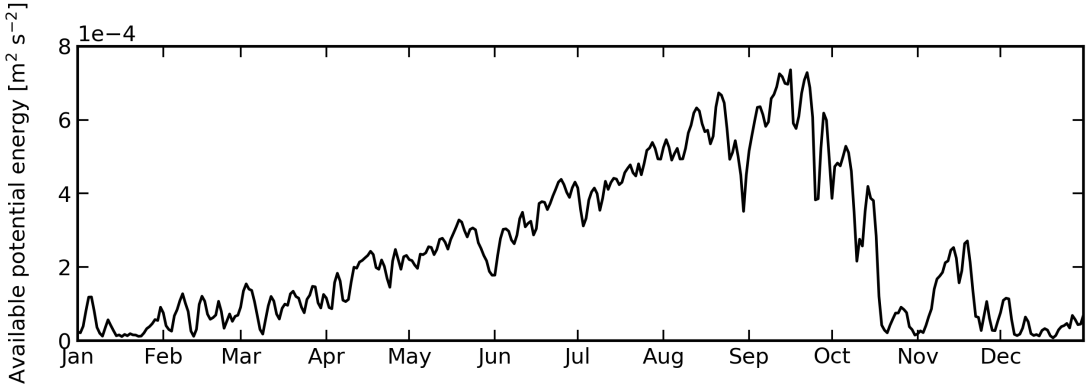

Figure 5.6: Seasonal cycle of the SAZ sub-domain average available potential energy in the mixed layer from the NEMO-SOSCEX36 simulation.

APE is much lower in the summer months ($\sim$1 m^2 s^{-2}) when the mixed layer is shallow (< 50 m). This is despite the horizontal buoyancy gradients being at a maximum within the seasonal cycle. APE then begins to steadily increase in April as the onset of seasonal cooling begins to deepen the mixed layer. APE continues to

rise until a seasonal peak occurs in September, when the mixed layer is deepest, even though the horizontal buoyancy gradients are seasonally weakest at this time. This indicates that the period most favorable for the development of mixed layer instabilities, which scale with the potential energy available for release, occurs during late winter and before surface heat fluxes have begun to warm the mixed layer.

The domain mean mixed layer vertical velocity, $\overline{w}$, is weakest in April (Figure 5.7a) when the MLD $\sim$ 50 m. An increase from May to a maximum in July of $\overline{w}$ $\sim$ 4 m. d^{-1} occurs at the same time as the MLD actively deepens to around 160 m. Instantaneously fluxes of w (Figure 5.7b, larger than 5 m. d^{-1}) occur more frequently in winter, indicating a seasonal cycle of vertical velocities.

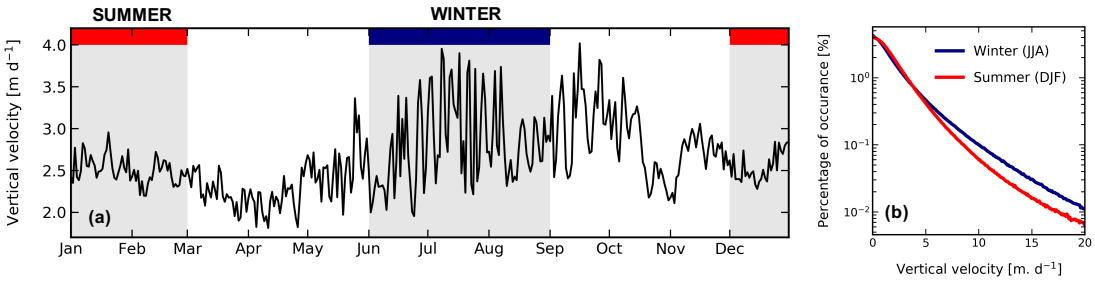

Figure 5.7: (a) Seasonal cycle of the SAZ sub-domain average vertical velocity at 42 m from the NEMO-SOSCEX36 simulation. (b) Histogram of the summer (DJF) and winter (JJA) values of vertical velocity at 42 m across the SAZ sub-domain.

Computations of $w'b'$ for the SAZ sub-domain shown in Figure 5.8 shows that there is an enhancement of vertical buoyancy fluxes in winter compared to summer. In both seasons, large values of $w'b'$ occur along frontal filaments and are often associated with upwelling and downwelling on either side of a front. Figure 5.9 shows the profile of vertical buoyancy flux that has been averaged across the SAZ sub-domain into a seasonal period (winter: JJA, summer: DJF). The average flux is consistently positive within the upper 300 m, but approaches zero near the surface. Maximum $w'b'$ occurs at approximately 45 m for summer and 75 m for winter, with winter fluxes seen to be significantly larger than summer. In winter, the maximum $w'b' \sim 0.9 \times 10^{-9}$ m^2 s^{-3}

occurs at around the middle of the mixed layer, supporting the presence of MLIs.

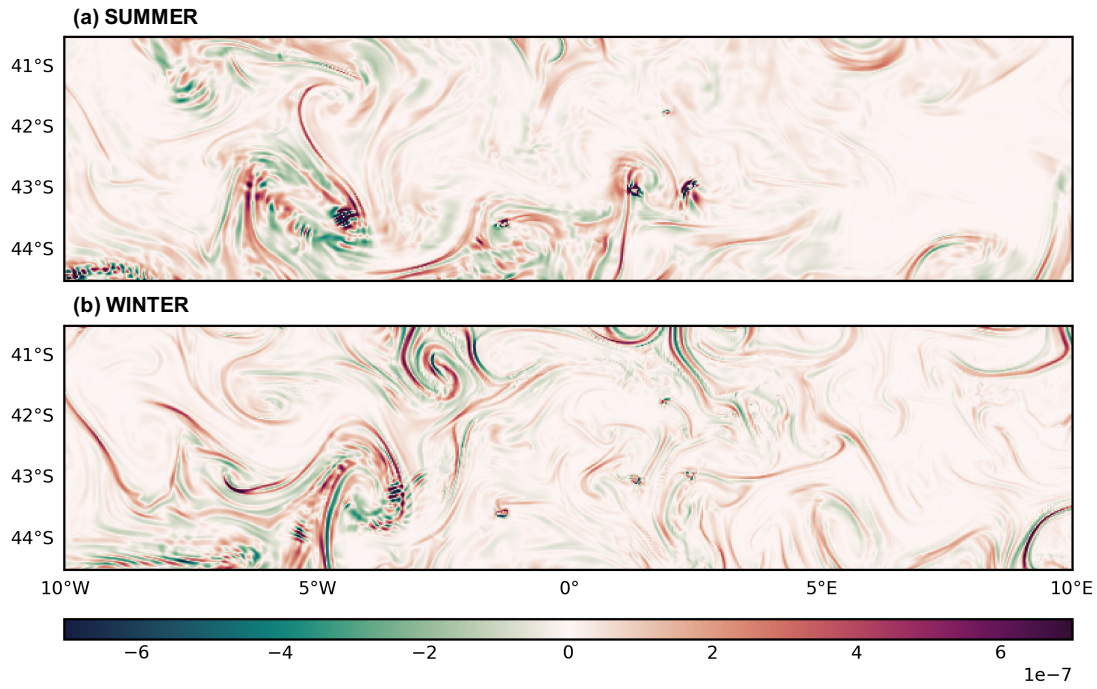

Figure 5.8: $w'b'$ maps ($m^2\ s^{-3}$) of the SAZ sub-domain at 42 m for (a) summer (8 February 2007) and (b) winter (8 July 2007) season from the NEMO-SOSCEX36 simulation

To quantify the conversion of potential energy to kinetic, the seasonal cycle of PK is studied (Figure 5.10). Values of PK indicate that the winter season displays the largest potential energy conversion. This is in line with the vertical velocity and APE seasonality. PK is weakest when frontogenesis is largest, suggesting that the net effect of the mixed layer vertical circulations is driven by MLI generation.

5.3.5 Frontogenesis

The seasonal cycle of frontogenesis is estimated by averaging mixed layer F_s across the SAZ sub-domain, $\overline{F_s}$ (Figure 5.11). Seasonality of frontogenesis largely follows that of the mixed layer horizontal buoyancy gradients. $\overline{F_s}$ is largest during the summer season (December - March), rising from $0.6 \times 10^{-20}\ s^{-5}$ when the surface heat flux becomes positive in October, to a maximum in January of $2.5 \times 10^{-20}\ s^{-5}$. $\overline{F_s}$ gradually declines

from March to reach a minimum in July, which follows the mixed layer deepening from 50 m - 150 m, the seasonal increase in vertical velocities and a weakening of the horizontal buoyancy gradient across the same time period. $\overline{F_s}$ remains low until mid-November, one month after seasonal restratification of the mixed layer (October). This seasonal weakening of $\overline{F_s}$ (March - July) could possibly be a result of the enhanced ASC supporting elevated vertical velocities to slump the horizontal buoyancy gradients when mixed layers are deep.

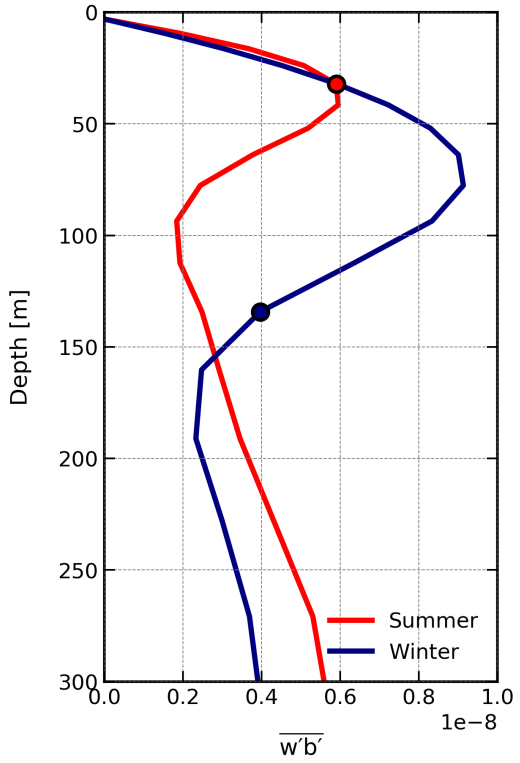

Figure 5.9: Vertical dependence of $w'b'$ (m^{-2} s^{-3}) averaged over the SAZ sub-domain for summer (red line, DJB) and winter (blue line, JJA). The dots represent the mean mixed layer depth averaged over the SAZ sub-domain for summer (32 m, red dot) and winter (134 m, blue dot).

5.3.6 Ekman buoyancy flux

Seasonality of the Ekman buoyancy flux averaged across the SAZ sub-domain, $\overline{\overline{\text{EBF}}}$ is shown in Figure 5.12. There does not appear to be any clear seasonal cycle, rather $\overline{\overline{\text{EBF}}}$ fluctuates between about 0 - 1.3 $\times$ 10^{-7} m^2 s^{-3} with a mean of order 10^{-7} m^2 s^{-3}. $\overline{\overline{\text{EBF}}}$ may be larger still given the likely stronger buoyancy gradients of a finer spatial resolution model or the real ocean. The variability of $\overline{\overline{\text{EBF}}}$ follows the synoptic variability of the winds, which vary by more than 1 m^2 s^{-3} over a single synoptic period, supporting the importance of wind variability in driving buoyancy fluxes and stratification in the SAZ. The weak seasonality of $\overline{\overline{\text{EBF}}}$ is likely a result of the opposing seasonal cycles of the wind stress and horizontal buoyancy gradients. This may hint to the vulnerability of the EBF seasonal cycle to the long-term variability of the winds.

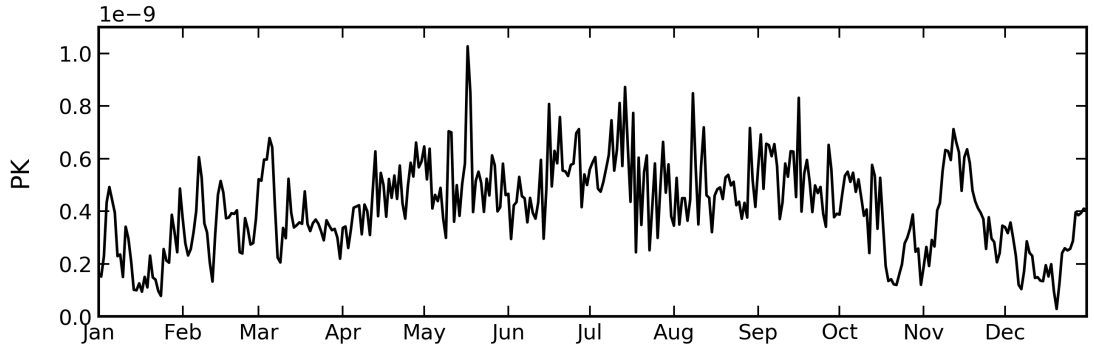

Figure 5.10: Seaonal cycle of the conversion rate of available potential energy into eddy kinetic energy, PK (m^2 s^{-3}), as calculated in Eq. 5.2. PK is integrated horizontally over SAZ sub-domain and vertically from the surface to the mixed layer depth.

5.4 Discussion

In this chapter, results from a realistic NEMO simulation of the Subantarctic Zone (SAZ) in the Southern Ocean are presented, with the aim of investigating the submesoscale processes in the mixed layer across a full seasonal cycle. The results show a clear submesoscale structure in the mixed layer flow, where mesoscale structures are separated by elongated filaments and vorticies associated with relative vorticity $\mathcal{O}(f)$,

indicating a depature from geostrophy in these highly energetic regions.

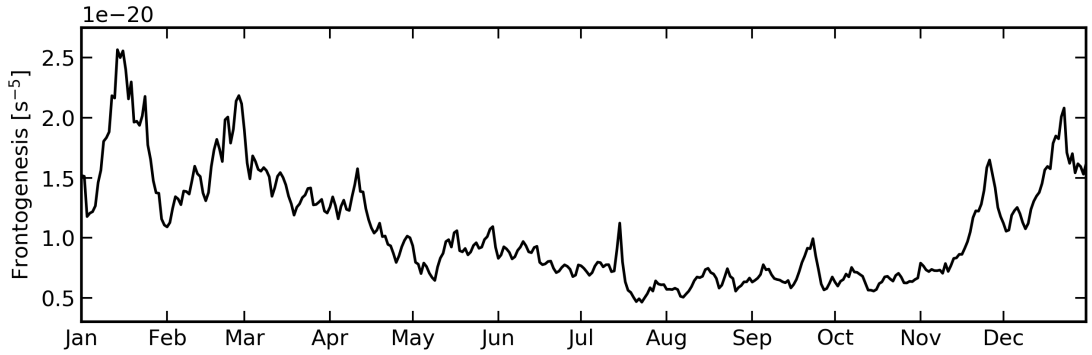

Figure 5.11: The seasonal cycle of the mixed layer frontogenesis function averaged over SAZ sub-domain, defined in Eq. 5.4.

The seasonality of the relative vorticity provides a clue to the submesoscale dynamics at play. There exists a constant positive skewness in the distribution of Rossby numbers for all seasons. This is analogous with submesoscale flow when limitations exist in the growth of instabilities for unstable potential vorticity (Rudnick, 2001). Seasonality in the skewness follows a marginal increase in the winter, lending to submesoscale flows having a stronger growth in winter, which agrees with the observations made in the North Atlantic (Buckingham et al., 2016). However, our results differ from those of Buckingham et al. (2016) in that we observe a presistence of submesoscale flows throughout the year, indicated by the year-round positive skewness, while this is not the case in the North Atlantic. This result is perhaps explained by the presence of seasonally stronger horizontal buoyancy gradients during summer, which are likely due to the enhanced frontogenesis within the mixed layer, provided by an active mesoscale eddy field.

During winter, strong atmospheric cooling is followed by a deepening of the mixed layer by about 100 m relative to summer. During this period, a secondary baroclinic instability in the mixed layer that converts potential to kinetic energy in the submesoscale range grows. This indicates that the balance between frontal instabilities by frontogenesis and baroclinic instabilities is goverened by the MLD. These baroclinic

instabilities may greatly impact the variability of the MLD indicated by enhanced standard deviation in winter. This builds a confidence in the presence of baroclinic instabilities as these results agree with the seasonal cycle of the release of APE, which creates an inverse cascade of kinetic energy (Mensa et al., 2013; Sasaki et al., 2014; Callies et al., 2015). Capet et al. (2008a) relate PK to the magntidue of the mixed layer buoyancy gradient in the mixed layer and the MLD. Given the opposing seasonal cycles of horizontal buoyancy gradients, which are stronger in summer, and the MLD, it appears that the deepening mixed layer is the governing factor in what drives the release of potential to kinetic energy in the SAZ. This enhancement during the winter relates directly to mixed layer restratification, which is maximum at about 60 m in the winter mixed layer. This falls in the middle of the mixed layer, which follows the structure of thermally driven overturning instabilities generated by mixed layer instabilities proposed by Fox-Kemper et al. (2008).

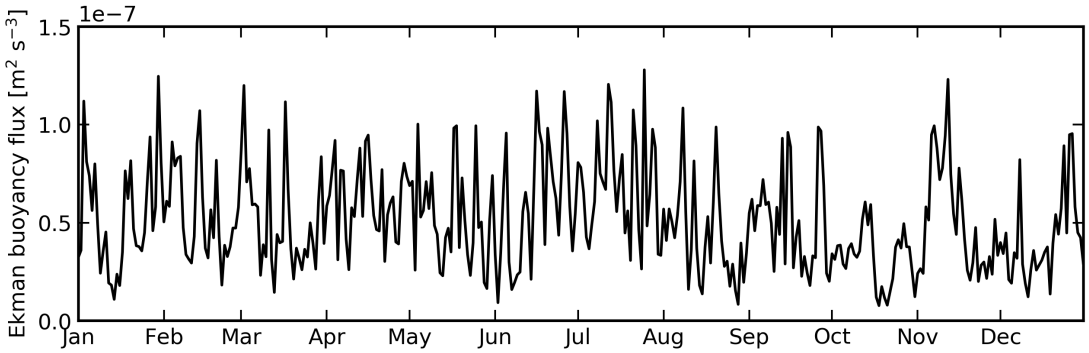

Figure 5.12: The root-mean-square magnitude of the Ekman buoyancy flux averaged over the SAZ sub-domain, defined in Eq. 5.5.

Previous studies have suggested that the mesoscale surface frontogenesis generates most of the submesoscale kinetic energy in the upper ocean (Lapeyre et al., 2006). While we do observe that frontogenesis is likely to be responsible for the enhanced horizontal buoyancy gradients and positive skewness in the Rossby numbers during summer, the weak APE and vertical buoyancy flux during this time suggests that frontogenesis is not a major role player in driving strong vertical submesoscale motions

in the SAZ. The dominance of the mixed layer baroclinic instability mechanism during deep mixed layers and the enhancement of submesoscale flow in winter corroborates with the expectation of Callies et al. (2015), who propose baroclinic instabilities to be present in the Southern Ocean. However, we show that our results are more nuanced in that we observe the dominance of baroclinic instabilities where MLDs are on average 150 - 200 m in winter, while the expectation for baroclinic instabilities to be present in the Southern Ocean are for deep mixed layers, which reach values far larger (> 400 m, Dong et al. (2008)) than those seen in this study.

These results have further supported the notion that submesoscale processes are prevelent in the open ocean and not only in regions of strong boundary currents and topographically influenced turbulent areas. The submesoscale fluxes are driven by the action of atmospheric forcing and momentum fluxes driving deep mixed layers. Although the surface fronts are present year-round, the vertical buoyancy fluxes scale with the MLD so the action of submesoscale flows driving vertical recirculations are seasonaly depenedent on the variability of the MLD. Indeed, the enhanced variability of the MLD during winter suggests that the vertical buoyancy fluxes may provide a restratification flux in regions of large fronts.

Although in this chapter, the seasonality of submesoscales has become clear and the atmospheric controls are discussed, a number of improvements can be foreseen in future work. A more refined numerical experiments at higher horizontal and vertical resolutions could enhance the role of horizontal buoyancy gradients in the seasonality of baroclinic instabilities, frontogenesis and EBF.

The enhanced vertical buoyancy fluxes associated with submesoscale flows may be important for the vertical distribution of physical and biogeochemical tracers such as key nutrients for phytoplankton growth. Given the substantial role of the Southern Ocean in the global CO_2 uptake (Sabine et al., 2004) and the large spatial heterogeneity of phytoplankton variability (Thomalla et al., 2011), it is plausable to consider that the presence of mixed layer baroclinic instabilities, especially in winter and when the mixed layer is still deep, may be partially responsible for fluxes of nutrients between the

nutrient depleted mixed layer and the nutrient rich thermocline (Tagliabue et al., 2014; Nicholson et al., 2016). We require to study the direct impacts which submesoscale fluxes contribute to the total vertical exchange of these key nutrients.

CHAPTER 6

Optimized sampling techniques to observe submesoscale gradients using gliders

This chapter is under preparation for publication as M. du Plessis, S. Swart and A. Mahadevan (2018) Optimized sampling techniques to observe submesoscale gradients using gliders.

6.1 Introduction

Submesoscale motions arise from strong horizontal buoyancy gradients which persist in the mixed layer with a typical horizontal scale of $\mathcal{O}$(0.1-10 km). These gradients can store large amounts of available potential energy (APE) which may produce instabilities in the flow and provide an efficient energy transfer to smaller scales. In particular, baroclinic mixed layer instabilities (MLI) have important impacts on upper ocean mixing and stratification. Associated with MLI is enhanced vertical fluxes which play an essential role in the vertical transport of ocean tracers and physical-biological coupling (Lévy et al., 2012). However, these processes are actively being further understood as insight into submesoscale dynamics has largely been achieved through high-resolution numerical simulations (Haine and Marshall, 1998; Boccaletti et al., 2007; Fox-Kemper et al., 2008; Capet et al., 2008a,b; Thomas and Ferrari, 2008; Mahadevan et al., 2010). Observations occurring at the required temporal and spatial resolution to resolve submesoscale processes is challenging given the small spatial and rapid temporal scales, $\mathcal{O}$(hours to days), at which they occur. However, significant improvement in observing submesoscale processes has been made using autonomous ocean gliders. Gliders sample the ocean by diving in a V-shaped pattern from the surface to 1000 m and back. The typical horizontal spatial distance between glider surfacing is about 5 km, thus providing a profile of the upper ocean around every 2.5 km. A particular strength of gliders is active sampling, where the pilot can direct the horizontal motion of the glider toward fronts and eddies identifiable by satellite remote sensing. This has been successfully performed to study the dynamics of persistent fronts and mesoscale eddies in many studies to date (*e.g.* Martin et al., 2009; Todd et al., 2009; Pelland et al., 2013; Thompson et al., 2014; Erickson et al., 2016; Krug et al., 2017). However, gliders are increasingly being used to sample the open ocean, away from time-mean fronts and high mesoscale eddy activity (Swart et al., 2015; Buckingham et al., 2016; Thompson et al., 2016; du Plessis et al., 2017). These studies have aimed to characterize submesoscales dynamics in regions which cover a large

proportion of the global ocean, such as the Southern Ocean and Northern Atlantic. A key component of submesoscale dynamics is the horizontal buoyancy gradient, which holds direct influence on key parameters such as potential vorticity (Shcherbina et al., 2013; Thompson et al., 2016; Todd et al., 2016), MLI (Thompson et al., 2016) and Ekman buoyancy flux (EBF) (Thomas and Lee, 2005, Chapter 4).

In observational glider studies, calculating the horizontal buoyancy gradient requires two assumptions: *i*) the timescale for the evolution of submesoscale processes (such as MLI of $\mathcal{O}$(hours to days)) occurs over a comparable time taken to perform a dive ($\sim$6 hours) and thus we assume the horizontal buoyancy gradient observed by the gliders is representative of a snapshot of *in-situ* fronts and does not change in magnitude or direction whilst the glider is diving, and *ii*) the glider calculates the horizontal buoyancy gradient as the gradient of buoyancy b = -$g(\rho$-$\rho_0)/\rho_0$ from the along track distance x, thus termed b_x, while the *in-situ* mixed layer horizontal buoyancy gradient is calculated as two-dimensional, $M^2 = (b_x, b_y)$, where here b_x is the zonal gradient and b_y is the meridional gradient of buoyancy. Throughout this study, M^2 is calculated in this way, while b_x will refer to the along track glider calculated horizontal buoyancy gradient. Therefore, the assumption here is that b_x is representative of M^2. One of the objectives of this study is to investigate these two assumptions and therefore the capability of gliders to characterize the total distribution of M^2 for the Subantarctic Zone (SAZ) of the Southern Ocean. This will provide useful for future glider deployments to understand the representative variability the horizontal buoyancy gradients estimated using gliders.

6.1.1 Region of study

Submesoscale dynamics within the Southern Ocean have primarily been studied in regions such as the Drake Passage (Rocha et al., 2016; Erickson et al., 2016; Bachman et al., 2017; Viglione et al., 2018) and the Kerguelen Plateau (Rosso et al., 2014, 2015). These regions are characterized by a strong mesoscale eddy field, persistent fronts and direct topographical influence driving enhanced vertical velocities. However, the

SAZ south of Africa is a particularly striking transitional zone between the warm and salty subtropics and the cool and fresh Antarctic region (Faure et al., 2011). Agulhas rings and eddies crossing from north of the Subtropical Front (STF, Swart and Speich, 2010; Arhan et al., 2011; Dencausse et al., 2011; Domingues et al., 2014), interact with equatorward flow from across the southern boundary (Subantarctic Front, SAF) of the SAZ driven by the Ekman response to westerly wind field (Rintoul and England, 2002). Sallée et al. (2006) show that the large gradients in temperature and salinity within the mixed layer lead to a lateral eddy diffusion of these interleaving water masses. The response of these large gradients and mixing to creating conditions suitable for submesoscale activity is to be explored in this work.

6.1.2 Numerical simulation

We obtain a full seasonal cycle (1 January 2007 - 31 December 2007) from NEMO-SOSCEX36 (See Section 2.4 in Chapter 2 for details). The model is a 1/36° simulation with 46 vertical levels and is forced with reanalysis surface and momentum fluxes from the European Centre for Medium-Range Weather Forecasts (Berrisford et al., 2011). NEMO-SOSCEX36 simulates the Atlantic Southern Ocean (10 °E to 20 °W and 38 °S to 53 °S, Figure 6.1). This study uses a sub-domain of the model to represent the SAZ region (10 °E to 10 °W and 40.5 °S to 44.5 °S). This box is chosen to represent the northern and southern boundaries of the SAZ, namely the STF and the SAF as determined in Swart and Speich (2010). The eastern zonal boundary of 10 °E is to avoid the influence of direct poleward Agulhas Current water in the analysis, as here the STF moves southward due to the preferential pathway of subtropical waters between 12 °E and 23 °E (Dencausse et al., 2011). Buoyancy and momentum fluxes are interpolated from a temporal resolution of 24 hours and 3 hours, respectively, to 3 minute time steps. Model output is saved once a day as the daily mean. Boundary conditions are supplied by a Southern Ocean 1/12° NEMO configuration.

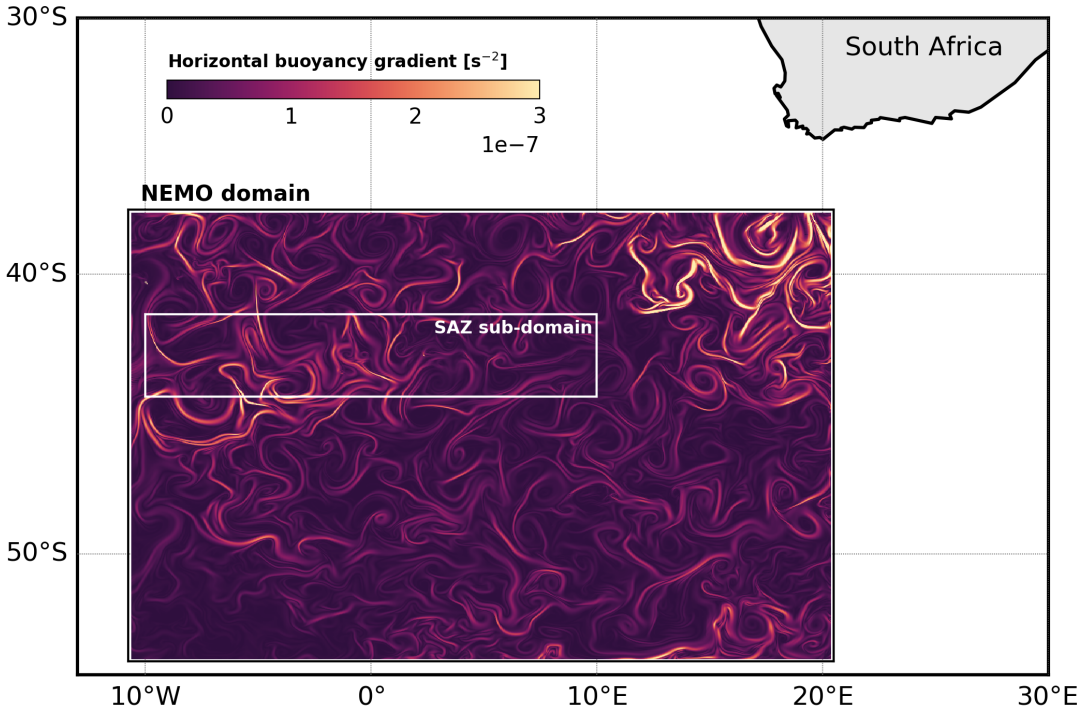

Figure 6.1: Mixed layer horizontal buoyancy gradient [s^{-2}] magnitude from a numerical NEMO simulation on 1 Januray 2007. The SAZ sub-domain used for the analysis in this work shown by the white box.

6.1.3 Specific aims and questions

The direction of this study will be as follows:

1. Firstly, we compare the distribution of model M^2 to more than 4000 glider-derived mixed layer values of b_x to provide an estimation of the ability of the model to represent the overall shape of the distribution of real ocean mixed layer fronts.

2. We simulate virtual gliders in the model using four commonly used sampling modes (meridional and zonal transects, box-shaped pattern and mooring mode) over a full annual period. We then compare the distribution of b_x determined by the virtual gliders to the total M^2 distribution within the SAZ.

3. Next, we test whether incrementally increasing the duration of glider sampling from one month to a full annual period improves the distribution of b_x relative to the total distribution of M^2 over the SAZ.

4. The following step is to determine the potential bias in the distribution of b_x when the distance a glider moves over a day varies.

5. Finally, the effectiveness of incrementally increasing the number of gliders sampling simultaneously from one to a swarm of six (*e.g.* Thomsen et al., 2016) in combined with the length of a glider mission to understand how best to characterize the horizontal buoyancy gradients of the SAZ.

6.2 Observation and model comparison

Due to computational limitations, temperature and salinity fields of the model are saved as daily averages. As the growth rate of MLI occurs over time scales on the order of a day, the model may smooth across horizontal buoyancy gradients which vary within sub-daily timescales. Daily output of horizontal buoyancy gradients from the model are compared directly to glider data obtained from the Southern Ocean Seasonal Cycle Experiment, where 4272 glider profiles were obtained within the SAZ at 43 °S and 8 °E over a period four years (SOSCEx, Swart et al., 2012, 2015; du Plessis et al., 2017). The data was collected between July and March.

In standard use, a glider profiles from the surface to 1000 m and back. This 1000 m dive cycle takes up to 6 hours to complete, covering approximately 6 km horizontally. To perform the model to glider comparison of horizontal buoyancy gradients, the temperature and salinity fields of the glider are interpolated onto daily grids prior to the calculation of b_x. There is a good agreement in the shape of the distribution of modeled M^2 and the *in-situ* glider calculated b_x from both individual glider profiles and the daily gridded glider data (Figure 6.2). The distribution of horizontal buoyancy gradients between the daily interpolated glider data and the model is tighter than the model and the individual glider profiles. This indicates that there is a higher probability

of observing larger horizontal buoyancy gradients by sampling at finer temporal and spatial resolutions. However, all three datasets compared have the same shape in the distribution of horizontal buoyancy gradients and thus provides confidence in the model to robustly represent the distribution of the horizontal buoyancy gradients for this analysis.

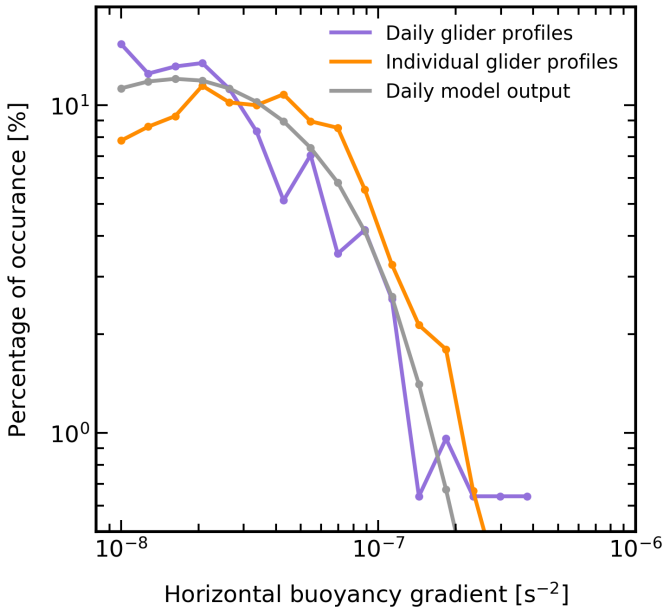

Figure 6.2: Distribution of mixed layer horizontal buoyancy gradients [s^{-2}] from 4272 in-situ glider measurements using individual profiles (orange) and profiles gridded to a daily resolution (purple), as well as the distribution of horizontal buoyancy gradients across the entire Subantarctic Zone sub-domain from the numerical NEMO simulation (Figure 6.1) (gray). Details of the glider deployments are in Table 2.1. The seasonal range encompassing the glider measurements for all the distributions is 16 July to 7 March.

6.3 Methods

6.3.1 Testing of four glider sampling modes

Common glider sampling modes include repeat patterns such as the box-shaped pattern (Chapter 4) and butterfly pattern in Thompson et al. (2016), the survey mode

or long distance transect (Swart et al., 2015; du Plessis et al., 2017) and virtual mooring mode, which is performed when the glider stays at one single target location as long as ambient current velocities do not exceed the glider speed. The following four virtual glider sampling modes are simulated in the model: meridional transects, zonal transects, repeat box-shaped pattern and virtual mooring mode, with each mode covering a full annual period (Figure 6.3).

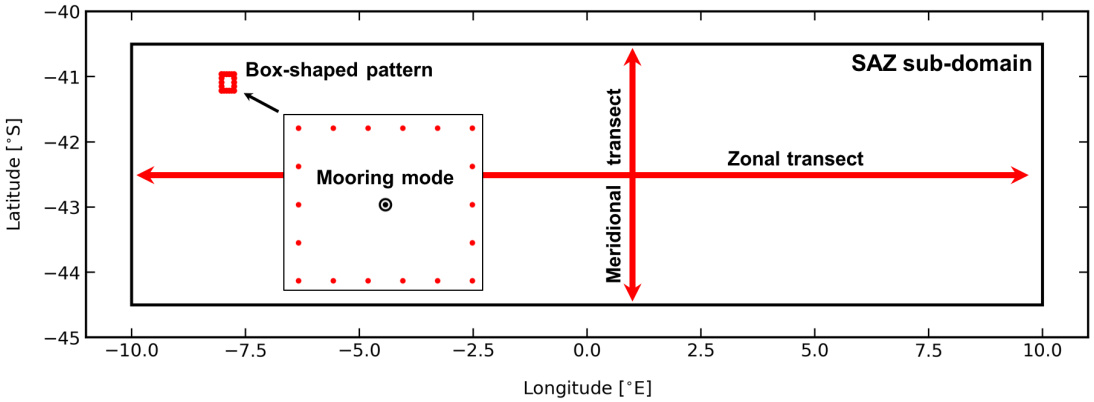

Figure 6.3: Schematical diagram indicating the four virtual glider sampling modes used in this analysis. These include repeat meridional and zonal transects (vertical and horizontal red lines), box-shaped pattern (red box) and mooring mode (black and white dot). Box-shaped pattern and mooring mode are enlarged for clarity.

The virtual gliders calculate horizontal buoyancy gradients in the following way. At time t_0, a measurement of mixed layer buoyancy is made (b_0). After one model time step (one day), or time t_1, the virtual glider obtains the mixed layer buoyancy (b_1) at a horizontal distance of 11.4 km along the respective sampling mode transect (x_{glider}). The horizontal buoyancy gradient is therefore calculated over a horizontal distance representative of the mean distance covered daily by the SOSCEx gliders ($b_x = (b_1 - b_0)/x_{glider}$). This allows for a time evolution of the buoyancy field as occurs in *in-situ* glider studies (Figure 6.4). This is done for all sampling modes except the virtual mooring mode, where the virtual glider remains in a fixed location over a day, thereby incorporating only temporal gradients in the calculation. Each virtual

sampling mode contains over 140 000 iterations, with each iteration having a unique starting location within the SAZ.

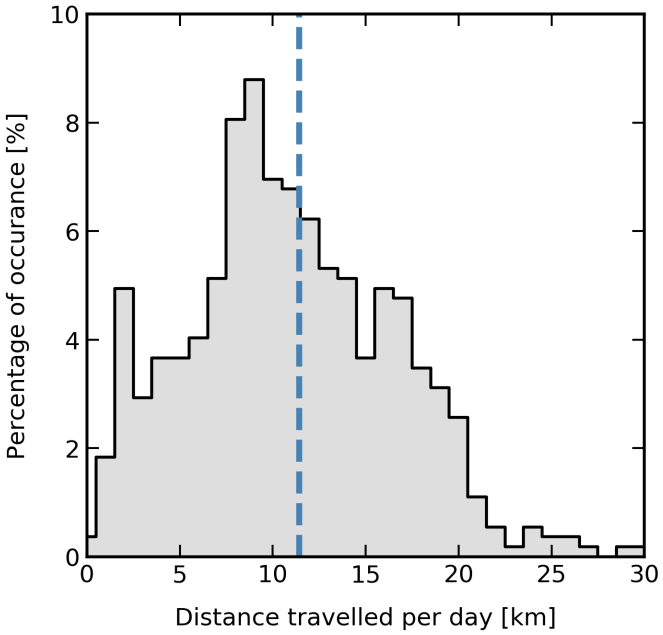

Figure 6.4: Distribution of the total distance travelled per day by the gliders in the Southern Ocean Seasonal Cycle Experiment (Swart et al., 2012). Blue dashed line indicates the value of the mean distance of the distribution of 11.4 km.

6.3.2 Variability obtained by increasing number of gliders

To determine the benefit of increasing the number of gliders sampling the ocean to achieve a more robust distribution of horizontal buoyancy gradients, we perform six annual-length (1 January - 31 December) virtual glider simulations by incrementally increasing the number of glider sampling simultaneously. To provide an index of the benefit of having multiple gliders sampling simultaneously, the distribution of horizontal buoyancy gradients calculated from the virtual glider is correlated to the distribution of all horizontal buoyancy gradients within the SAZ sub-domain. This analysis is performed at monthly intervals to better understand the balance of having multiple gliders sampling simultaneously with the added complexity of the variable

duration of sampling.

6.4 Results

6.4.1 Testing various glider sampling modes

The mean distribution of horizontal buoyancy gradients for each sampling mode is compared to the M^2 distribution for the entire SAZ sub-domain (Figure 6.5). Overall, there is a good agreement in the shape of the b_x distribution of all sampling modes and shape of the distribution of M^2 in the SAZ. All sampling modes show a marginal over-representation of $b_x < 10^{-7}$ s^{-2}, ranging from 95% for the box-shaped pattern to 98% for mooring mode compared to 93% for all SAZ M^2 values. Subsequently, this leads to an under-representation of $b_x > 10^{-7}$ s^{-2} relative to M^2. The standard deviation of the distribution of b_x across all unique transects for each sampling mode (Figure 6.5) encouragingly indicates that the M^2 distribution falls within a standard deviation around the mean for the b_x distribution of all sampling modes. The spread in the percentage of occurrence for weak b_x (10^{-8} s^{-2}) shows that gliders are likely to overestimate the presence of weaker fronts ($M^2 \sim 10^{-8}$ s^{-2}) by between 3% to 7% of the total occurrences. Conversely, for b_x values of 10^{-7} s^{-2} (*i.e.* sharper fronts), gliders are likely to underestimate the presence of M^2 by 0.3% of the total occurrences.

SEASONAL CYCLE ANALYSIS

The distribution of horizontal buoyancy gradients that are sampled by the virtual gliders provides important information for the capabilities of gliders to observe the overall submesoscale gradients for the SAZ. Now, we aim to better understand the ability of gliders to represent the seasonal cycle of the magnitude of horizontal buoyancy gradients for the SAZ. To do this, the magnitude of the horizontal buoyancy gradient from each of the unique transects of the sampling modes (> 140 000 seasonal cycles of $|b_x|$ per sampling mode) are correlated to the seasonal cycle of all mixed layer M^2 values across the SAZ sub-domain (*e.g.* Figure 6.6). The percentage of the

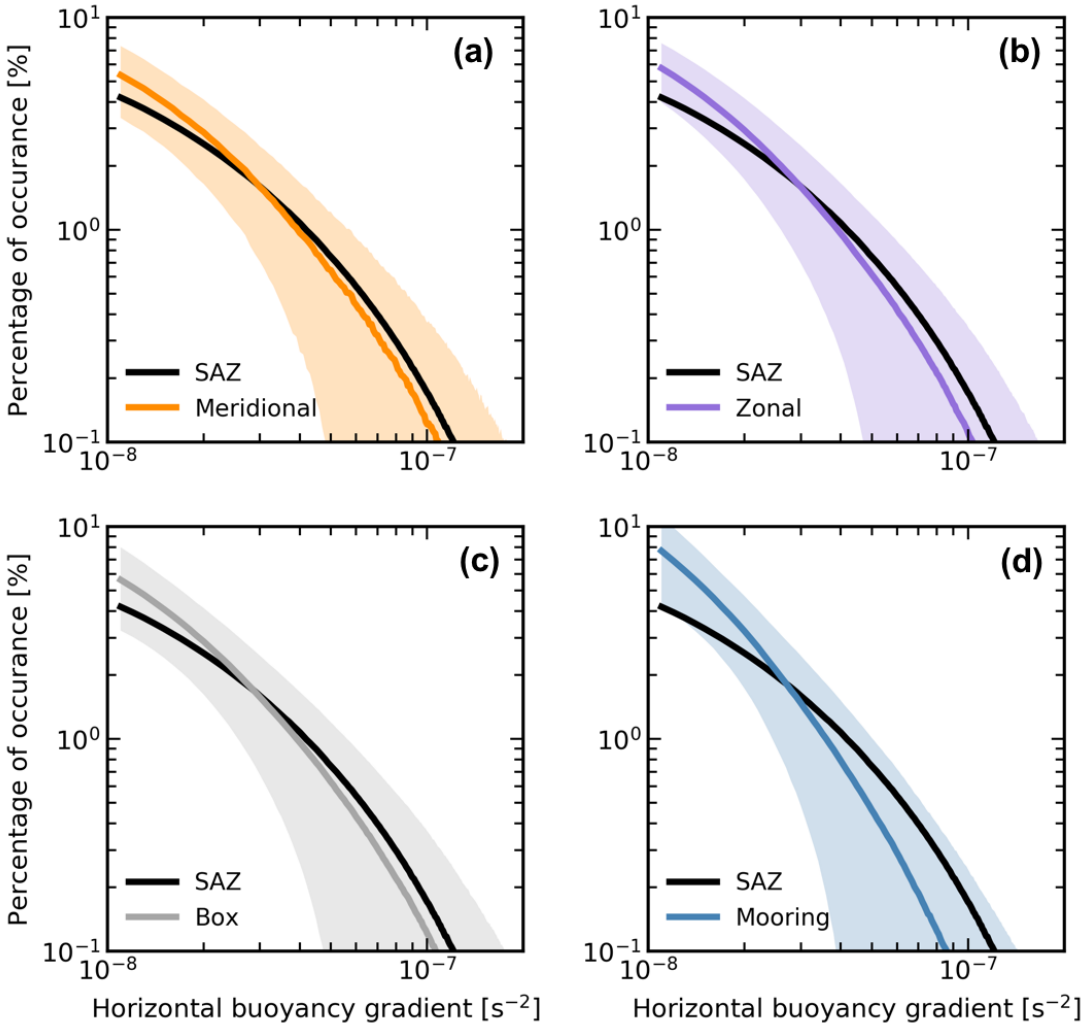

Figure 6.5: (a) The mean and standard deviation (shaded colors) histogram distributions of horizontal buoyancy gradients from all possible (> 140 000) combinations of seasonal length transects of the glider sampling modes. The black line represents the distribution of horizontal buoyancy gradients for the SAZ sub-domain shown in Figure 6.3 for the annual period of 2007. (a-d) represent the different sampling modes, namely merdional, zonal, box-shaped and mooring.

seasonal cycle captured by each sampling mode is obtained by the mean correlation of all unique transects for that sampling mode. At maximum, the seasonal cycle explains 4% $\pm$ 1% across the various sampling modes, suggesting that the dominant signal in the estimates of $|b_x|$ is the frontal variability associated with horizontal buoyancy gradients.

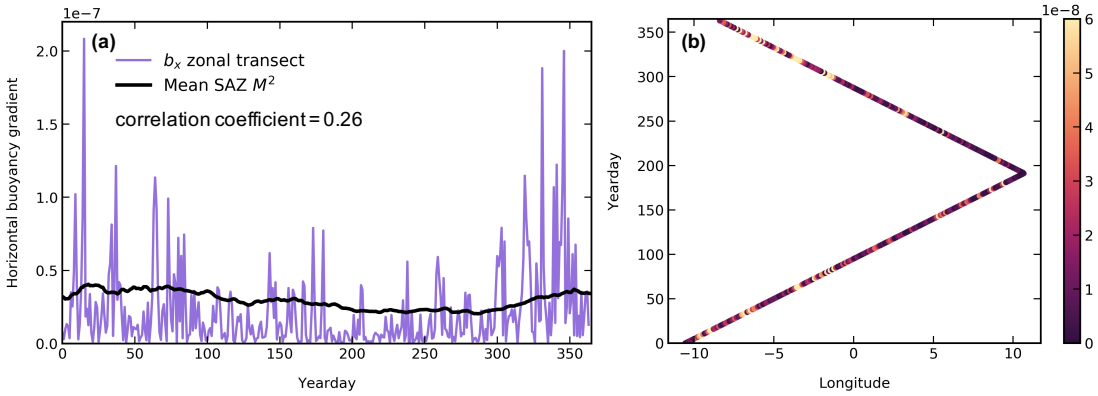

Figure 6.6: (a) The seasonal cycle of horizontal buoyancy gradients obtained from a single unique transect from the zonal sampling mode ($|b_x|$, purple line) compared to the seasonal cycle of the mean mixed layer horizontal buoyancy gradients for the SAZ sub-domain (M^2, black line). Correlation coefficient between the two seasonal cycles shown as r=0.26. (b) Hovmöller of the unique transect shown in (a), with the associated values of $|b_x|$ in color with units of s^{-2}.

6.4.2 Amount of variance captured as a function of sampling duration

For each unique transect of the sampling modes, the variance of $|b_x|$ is obtained as a function of the number of days that the virtual glider sampled. A ratio is determined between these values and the variance of all M^2 values within the SAZ sub-domain. The mean ratio for all unique transects of each sampling mode is converted to a percentage to determine the variance captured per sampling mode. All glider sampling modes rapidly increase the variance captured from the beginning of sampling to a maximum after about 15 days. The gliders sampling in a box-shaped pattern and meridional mode capture the most amount of M^2 variance (> 50%). The zonal mode obtains a maximum amount of variance explained (~45%) after two weeks before leveling off

between 30%-40% for sampling durations longer than two weeks, while the mooring mode is only able to capture ∼30% of the total variance.

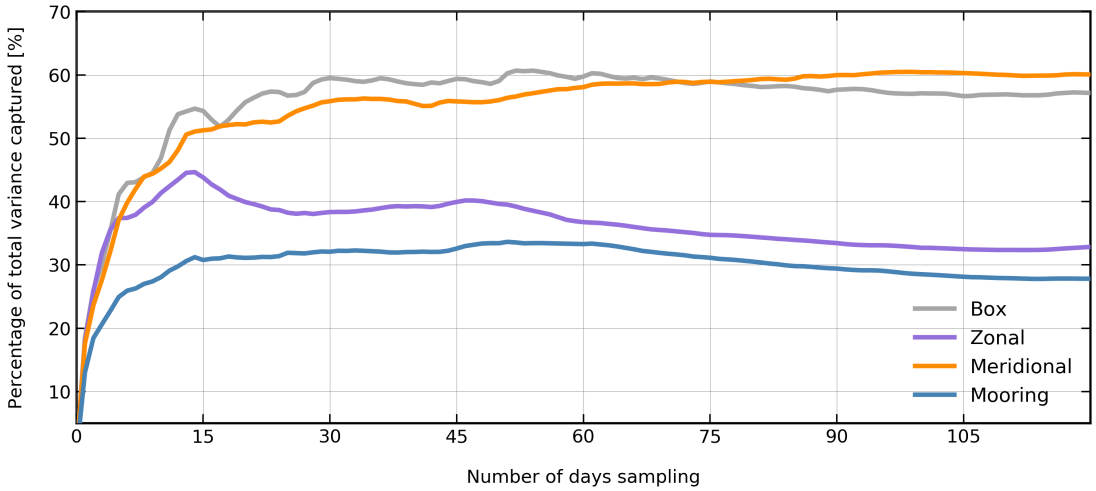

Figure 6.7: Mean percentage of the total variance explained by individual transects as a function of the duration a glider samples.

6.4.3 Investigating the distribution of horizontal buoyancy gradients observed by the spatial resolution of sampling

The horizontal distance a glider covers in a day of sampling typically ranges between 1 - 25 km (Figure 6.4). We investigate the bias in the distribution of b_x observed as a function of the horizontal distance covered by a glider across a day. This is done by obtaining b_x from a virtual glider simulation in the meridional sampling mode and iteratively changing the horizontal distance covered per day. This is performed for all unique transects (> 140 000), where the mean distribution is shown for each horizontal resolution (Figure 6.8). As scales less than 10 km, there is an increase in the occurrence of stronger fronts (> 10^{-7} s^{-2}) observed as well as a higher probability of capturing weak (10^{-7} s^{-2}) fronts.

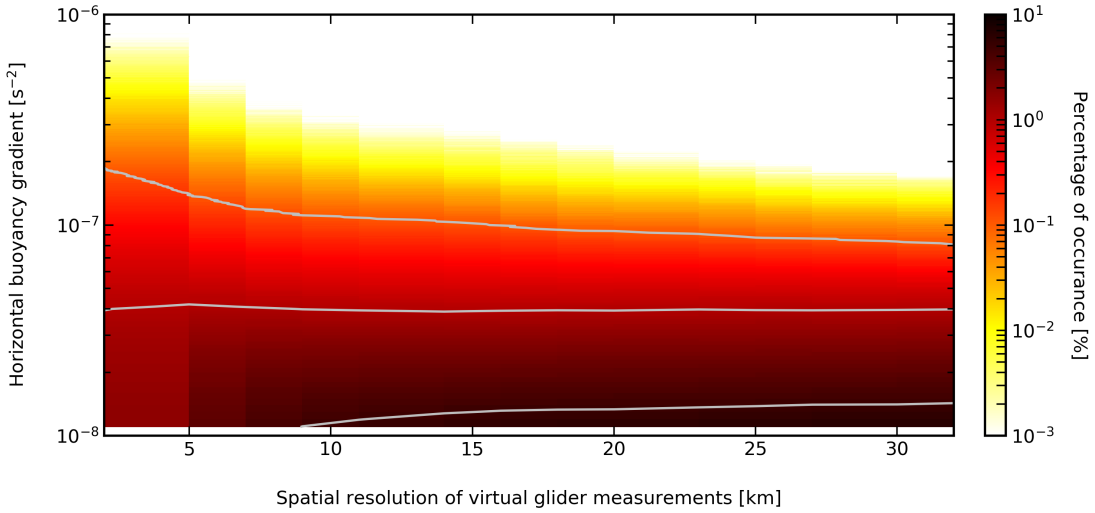

Figure 6.8: The distribution of horizontal buoyancy gradients observed as a function of the spatial resolution which a virtual glider covers per day. Colors indicate the percentage of occcurances for the horizontal buoyancy gradients. Gray contours represent the 0.1%, 1% and 5% percentage of occurrence.

6.4.4 M^2 variability explained by sampling duration and number of gliders used

Simulating over 140 000 unique seasonal length glider transects in the SAZ domain allows for the testing of whether increasing the number of gliders sampling at the same time will result in a distribution more representative of the total distribution of M^2 in the SAZ. b_x distributions are obtained for all unique transects using the meridional sampling mode as a function of the number of gliders sampling simultaneously as well as the duration the gliders are sampling for. These b_x distributions are correlated to the distribution of all M^2 for the SAZ domain for the equivalent duration of sampling (Figure 6.9). As expected, the weakest correlation occurs when one glider has sampled for one month (r^2 = 0.14). This improves to r^2=0.69 after 12 months of sampling. The increase in r^2 for each month that a glider samples is between 0.02-0.08, meaning that for every extra month the glider samples, there is an increase of between 2-8% of the total variability observed. Increasing the number of gliders sampling simultaneously provides a similar (6-9%) increase per glider added. Furthermore, a swarm of six gliders sampling for one month provides 51% of the total variability of the system.

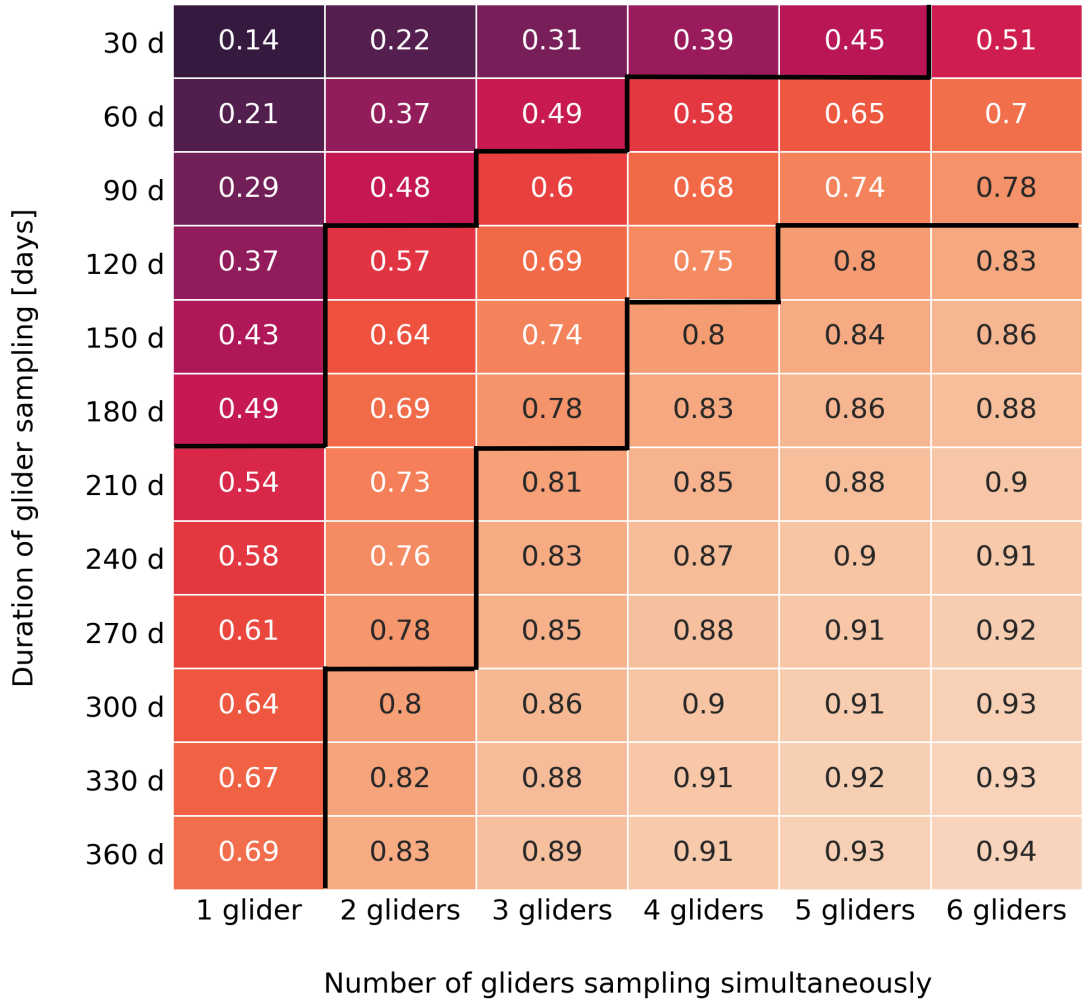

Figure 6.9: Figure representing the correlation coefficient (r^2, lighter colors represent stronger positive correlations) between the horizontal buoyancy gradient distributions for a given amount of gliders (x-axis) samping for a given duration (y-axis) and the total Subantarctic Zone (SAZ) sub-domain. Higher r^2 values indicate a larger representation of the variability of the horizontal buoyancy gradient. Black lines denote a seperation of r^2 values of 0.5 and 0.8

6.5 Discussion

Ocean submesoscale dynamics develop within scales of the Rossby radius of deformation (0.1-10 km) and evolve on the order of a day. The horizontal resolution of the numerical model run used in this work to determine the distribution of submesoscale

horizontal buoyancy gradients allows for resolving of the submesoscale gradients, while the temporal resolution of one daily output allows for the capturing of the evolution of submesoscale dynamics. The scale and distribution of horizontal buoyancy gradients of the model are consistent with *in-situ* observations. This suggests that the model is able to represent the leading-order submesoscale variability of the *in-situ* ocean mixed layer. This builds confidence in the usefulness of the model analysis which determines how to use gliders to most effectively observe the variability of horizontal buoyancy gradient in the SAZ.

Experimental campaigns to date have employed various glider sampling techniques in their field campaigns. Most glider experiments are designed to sample a particular feature such as a persistent front or a mesoscale eddy. However, recent work has highlighted the importance of open ocean dynamics contributing meaningfully to the submesoscale variability in the world's ocean (e.g. Rudnick and Cole, 2011; Swart et al., 2015; Thompson et al., 2016; Buckingham et al., 2016; du Plessis et al., 2017). The results shown in this chapter indicate that choosing a direction of sampling in the open ocean regions does not greatly influence the mean distribution of submesoscale horizontal buoyancy gradients observed over an annual cycle. The horizontal buoyancy fronts are likely stirred around and are isotropic in nature. This provides confidence in the ability of gliders to represent the regional distribution of horizontal buoyancy gradients which proliferate in the ocean. Of course, gliders are only capable of sampling a localized region of the ocean and are therefore unlikely to estimate the total variance of the region. Our results indicate that for gliders sampling in open ocean regions such as the SAZ, the variability of horizontal buoyancy gradients is best represented when sampling using a box-shaped pattern or performing meridional transects within the domain. The benefit of a box-shaped pattern is the combination of zonal and meridional sampling directions, as frontal filaments may align along elongated lines and thus a glider sampling parallel to the filament will under-represent the variability of horizontal buoyancy gradients. The meridional sampling strategy is an alternative preferred method of sampling in the SAZ as both the southern and northern boundaries

are influenced by ambient water masses (subtropical and Antarctic). Thus, enhanced horizontal gradients generated by either source of inflow is likely to be sampled by the glider. The weakest representation of horizontal buoyancy gradient variability in the SAZ is when sampling using the mooring mode. This is probably due to the glider not moving horizontally and thus not crossing the local horizontal buoyancy gradient. Rather, by sampling in the mooring mode, any horizontal buoyancy gradient acquired is a function of the advection of buoyancy into the sampling site.

An interesting component of the results is the drop-off in the number of strong fronts observed when the glider changes the distance it samples in a day. Of course, gliders sample more frequency ($\sim$6 hours) and at smaller scales ($\sim$2 km) than the daily distance proposed here, but this provides a first insight into the variability of fronts which may be under-represented due to the horizontal resolution of sampling. Therefore, we propose that the optimal technique for glider sampling is to perform dives over a small horizontal spatial distance, preferably around 1 km, which may reveal much sharper fronts than determined here.

Submesoscale dynamics are difficult to observe due to their fast evolving time scales and small horizontal length scales. Ocean gliders have made a large step in characterizing these submesoscale dynamics due to their ability to sample at a high horizontal resolution and for extended periods of time. However, glider is only able to capture a small localized region and thus do not represent the full scale of variability associated with a region such as the Southern Ocean. The results in this study have made a step forward towards understanding exactly how much of the variability gliders are observing. A single glider sampling the SAZ for a month is poor at representing the overall variability of the region (14% of the horizontal buoyancy gradients). Should future glider projects be limited by time, we would encourage a field campaign to employ up to six gliders (where feasible, of course) which can sample the region simultaneously. The variability of the region represented by the six gliders increases to 51% for just one month of sampling. Glider campaigns which lasting six months, such as Chapter 4, will provide around half of the total variability

of the SAZ, while by adding two more gliders increases that representation to 78%. The results further suggest that given the glider studies in this thesis, it is likely that only half of the total submesoscale variability of the SAZ is represented. This has large implications for understanding the importance of submesoscale dynamics impacting mixed layer variability in the Southern Ocean, where it is plausible that enhanced variability of the mixed layer depth and stratification could be driven by submesoscale processes such as MLI and EBF. Interestingly, these results infer that gliders are able to represent the full range of M^2 variability (95%) when six gliders sample for an entire year. This may have important considerations for the future of ocean observations, such as was proposed by Stommel, 1989 where a swarm of glider continually sample the ocean to provide real-time understanding of ocean dynamics.

CHAPTER 7

Concluding remarks and future perspectives

7.1 Thesis findings

7.1.1 Key findings

Submesoscale flows of $\mathcal{O}$(0.1-10 km) have increasingly been shown to play a key role in the evolution of the mixed layer (Thomas et al., 2008; McWilliams, 2016). The autonomous ocean glider deployments as a part of the Southern Ocean Seasonal Cycle Experiment provide key variables of temperature, salinity, pressure and depth-averaged currents at high resolutions ($\sim$5 km, 4 hours) over long endurance missions (3-6 months) to explore the dynamics of submesoscale flows in the open ocean Subantarctic Ocean. These measurements of the upper ocean are combined with atmospheric reanalysis data of co-located momentum and buoyancy fluxes to better understand the ocean-atmosphere interactions occurring at submesoscales and its impact on mixed layer variability. This thesis makes use of five separate seasonal-length glider deployments to observe and study the evolution of the mixed layer dynamics and characterize the role of submesoscale mechanisms between winter and late summer, and in particular during the springtime restratification phase of the mixed layer.

In the first part of this thesis, glider observations are analyzed to study the impact of one-dimensional atmospheric forcing on the seasonal restratification of the mixed layer. The role of one-dimensional forcing is determined by employing the use of the PWP mixed layer ocean model to show that in this dataset, the evolution of the magnitude of *in-situ* mixed layer stratification is elevated relative to the model simulation during the spring restratification phase. The misrepresentation of stratification by the one-dimensional model is proposed to be a result of the unresolved submesoscale dynamics and advective processes by the model. Calculations of submesoscale vertical buoyancy flux and up-front winds suggest that a combination of MLIs and restratification by up-front winds both contribute to the enhancement of stratification in the upper ocean. Swart et al. (2015) use the same dataset to indicate the immediate increase of chlorophyll within the mixed layer in response to the elevated springtime stratification. This work, therefore, suggests that submesoscale features are likely to indirectly impact

the biophysical interactions by altering the stratification and thus the alleviation of light for biomass growth. Furthermore, the enhanced stratification of the mixed layer by submesoscale processes may generate a response in the mixed layer thermodynamics as the shallowing of the mixed layer, and strengthening of the stratification is likely to reduce vertical heat transfer and thereby impact mixed layer heat budget estimates (Dong et al., 2007).

The second part of this thesis is aimed at understanding the potential of these submesoscale processes to generate inter-annual differences in the timing of seasonal restratification of the mixed layer. This is done by the use of glider deployments from the same location across four different years, with each year sampling between 3-6 months over the seasonal restratification period. Parameterizations of MLI and EBF into the one-dimensional mixed layer model of Chapter 3 reveals that down-front winds provide enhanced mixing, arresting the seasonal restratification despite atmospheric warming. This is shown to have particularly striking impacts on the timing of seasonal mixed layer restratification, which can differ by 28 days between the different years studied. Winter to summer observations of the upper ocean shows that within the mixed layer, convective instabilities dominate the potential vorticity estimates, thus indicating the importance of the vertical component of potential vorticity to its full budget. Furthermore, weak potential vorticity found at the base of the winter mixed layer is associated with deeper mixed layers, suggesting the potential for deeper mixing and elevated APE during strong down-front wind-mixing events. The generation of deep mixed layers by EBF may result in the potential for MLIs and subsequent submesoscale restratification by increasing the APE.

In the third part of this thesis, I employ the use of a three-dimensional NEMO model simulation at high resolution ($1/36^{\circ}$, 46 vertical levels) to investigate the seasonal cycle of submesoscale dynamics in the SAZ. I show that submesoscale flows are more intense during winter than summer due to the seasonal deepening of the mixed layer in response to atmospheric cooling. The result is to increase APE during winter, thereby promoting MLI generation. Elevated vertical buoyancy flux in the mixed layer during

the winter suggests that MLI generation is leading to enhanced ASC and potential restratification during winter. This may explain periodic restratification events during the winter from the glider observations in Chapter 4. Contrastingly, frontogenesis is elevated during the summer, when horizontal buoyancy gradients are strongest and mixed layers are shallow, indicating that the key mechanisms for submesoscale flow impacting stratification in the SAZ are MLIs and EBF.

In the final part of this thesis, I perform simulations of virtual gliders in the NEMO model to understand the impact different glider sampling strategies have on the distribution of horizontal buoyancy gradients observed in glider studies. I show that gliders are suitable platforms for observing the submesoscale structure of the mixed layer due to the isotropic nature of the mixed layer fronts, albeit marginally under-representing the presence of stronger fronts. Gliders are only able to observe about 60% of the variance of the region for a given meridional or box-shaped transect of the ocean. The weak representation of variance of the horizontal buoyancy gradient by the zonal and mooring mode of sampling reveals that it is essential to consider the dynamics of the region in which gliders are sampling before performing field campaigns. It is likely that there is a strong horizontal buoyancy gradient variance near the northern and southern boundaries of the SAZ due to the influence South Atlantic gyre interaction and the associated gradients at the STF. Finally, correlations of the distribution of horizontal buoyancy gradients observed by using a varying amount of gliders (one to six) sampling for varying amounts of time (a month to a year) provides recommendations for future fieldwork campaigns of the representative measure of the submesoscale gradients gliders will observe.

7.1.2 Providing context to global climate models

The findings of this thesis may have direct implications for how we simulate the ocean. A global climate model would require to consider the fundamental underlying physics. Present climate models are currently unable to simulate the strength and depth of the mixed layer stratification in the Southern Ocean (Sallée et al., 2013a).

The results presented here indicate the need to represent the processes of MLI and EBF robustly. In particular, the down-front mixing component has shown to provide enhanced energetics for the Southern Ocean. This has previously been observed in strong frontal regions such as the Kuroshio Current (D'Asaro et al., 2011), where turbulent mixing may be enhanced by order of magnitude. This can have severe impacts for vertical transfer of heat, gases, and tracers in the Southern Ocean if it is not correctly represented. Furthermore, this work differs from the work in the Kurushio as here we propose the importance of the persistent uni-directional wind forcing, which occurs over large regions of the Southern Ocean. The impact of this mixing on deepening the mixed layer, enhancing the APE and thereby promoting MLI generation leading to enhanced vertical buoyancy fluxes should be considered for future model endeavors.

7.2 Gliders as tools for sampling upper ocean dynamics

Autonomous underwater gliders are increasingly becoming an essential instrument for identifying and characterizing the presence of submesoscale flows in the ocean. Their capabilities extend beyond traditional sampling techniques, as they can survey the ocean for extended periods of time at high spatial and temporal resolution. A significant benefit of gliders is the ability to deploy them in remote or difficult to access regions of the world's ocean. This has important implications for the understanding of processes in areas that previously we inaccessible. This includes the recent development in the under-ice sampling capabilities by the University of Washington. Extended observations of the physical ocean under the sea ice is to become a topic of great interest in the coming years. This has already begun to be explored in the Beaufort Sea and soon to be expected in the Southern Ocean.

A remarkable feature of gliders, as ocean observing tools, is their ability to be steered. It would be interesting to consider future observational field campaigns whereby a swarm of gliders are deployed to perform a wide range of sampling strategies. This would involve characterizing the dynamic upper ocean in a way that

includes a pseudo monitoring site (mooring mode), a regional characterization mode (transects) as well as a 'free' glider to roam the region in search of features such as frontal meanders and eddies identifiable from the satellite in real time. Furthermore, field campaigns incorporating other ocean observing technologies, such as surface vehicles (*e.g.* Wave Gliders) are pertinent in combining the upper ocean dynamics to *in-situ* atmospheric forcing mechanisms such as wind speed and direction and radiation. The ongoing SOSCEx and ORCHESTRA field campaigns provide an example (pers. comm. S. Swart).

7.3 Future perspectives

In this thesis, ocean gliders are used to sample the upper ocean frontal dynamics. The observations indicate that gliders can resolve both the magnitude and timing of the seasonal enhancement of strong fronts (Chapter 4). It is shown in Chapter 5 that the glider missions in this thesis likely underestimate the distribution (*i.e.* what the scale of the observed fronts are) by about 50%. Additionally, I show that the horizontal buoyancy gradients determined by the glider represent around 60% of the regional spatial variability of the fronts. However, a remarkable aspect of the gliders as a tool for identifying the fronts is that it only requires about two weeks of continual sampling to capture this amount of variance in the b_x. This may potentially be useful for research teams/projects without the resources to deploy assets for many months of sampling. The relatively short period required to sample a large component of the variability of submesoscale gradients means that focused glider studies can occur on typical research voyages of weeks to months, such as supply cruises to Antarctic bases, to achieve a robust understanding of the upper ocean physical system for a region. The caveat being if the deployments are intended primarily to capture the range of variance of horizontal buoyancy gradients and its resulting dynamics. Naturally, these few weeks of sampling would not obtain the seasonal cycle of upper ocean bio-physical interactions that depend on processes exterior to the mixed layer.

To characterize the full regional distribution of buoyancy gradients, an extensive

field campaign is required. Employing the use of three gliders for a six month period provides 80% of the distribution of horizontal buoyancy gradients. This type of sampling is beginning to be within the scope of current research projects (*e.g.* ROAM-MIZ, a multi-national collaboration lead by the University of Gothenburg to observe the Southern Ocean Marginal Ice Zone).

Another key finding of this thesis is the identification of periods within an annual cycle where mixed layer variability is enhanced and where submesoscale mechanisms are driving this variability. The most notable period is during the spring restratification, where mixed layers can vary over 100 m per day. The implication of this mixed layer variability is potentially critical to bio-physical interactions and the transfer of heat and gases between the mixed layer and below. A tandem glider survey involving numerous gliders separated by lengths greater than the mixed layer Rossby radius of deformation can allow for understanding the role of local processes (wind forcing, heat, fronts) on mixed layer variability during the critical spring phase. Such a survey involving two gliders currently exists (see Swart et al., 2015).

It would be interesting to think about what has been learned from the sampling modes in Chapter 5 to apply to existing glider datasets. Field campaigns with multiple gliders surveying the ocean in numerous modes have been undertaken (*e.g.* SOSCEx, ORCHESTRA). The comparisons of *in-situ* distributions of submesoscale buoyancy gradients from the various sampling modes would provide unique insight into the differences at which these modes are able to represent the fronts of the real ocean. These observations can help guide the standard for observing submesoscale processes using ocean gliders.

An interesting result of this thesis is the similarities in the mean distribution of horizontal buoyancy gradients by the different sampling modes. This tells us that although the Southern Ocean is aligned into zonal bands separating different water masses, the submesoscale buoyancy gradients within the SAZ are primarily isotropic. However, characterizing the evolution of submesoscale mechanisms across these large-scale frontal boundaries would potentially be an avenue for future work.

Another potential for future work is the further investigation of these presence and variability of submesoscale mechanisms such MLI in regions of deep mixed layers where APE is likely to be enhanced such as the eastern South Pacific (Dong et al., 2008) and southeastern Indian Ocean (Sallée et al., 2006), where strong atmospheric forcing is expected to impact the presence of submesoscales indirectly.

Acronyms

ACC Antarctic Circumpolar Current

AAIW Antarctic Intermediate Water

APF Antarctic Polar Front

ASC Ageostrophic secondary circulation

CO_2 Carbon dioxide

EBF Ekman bouyancy flux

ERA European Centre for Medium-Range Weather Forecasts Re-Analysis Interim

KE Kinetic energy

MERRA Modern Era Retrospective-analysis for Research and Applications

MLD Mixed layer depth

MLE Mixed layer eddies

MLI Mixed layer instabilities

NCEP National Centers for Environmental Prediction

PWP Price Weller Pinkel

sACCf Southern Anatarctic Circumpolar Current Front

SAF Subantarctic Front

SAZ Subantarctic Zone

SAM Southern Annular Mode

SAMW Subantarctic Mode Water

SBdy Southern Boundary

SOSCEx Southern Ocean Seasonal Cycle Experiment

SST Sea Surface Temperature

STF Subtropical Front

Bibliography

Abernathey, R., Marshall, J., and Ferreira, D. (2011). The Dependence of Southern Ocean Meridional Overturning on Wind Stress. *Journal of Physical Oceanography*, 41(12):2261–2278.

Adams, K. A., Hosegood, P., Taylor, J. R., Sallée, J.-B., Bachman, S., Torres, R., and Stamper, M. (2017). Frontal Circulation and Submesoscale Variability during the Formation of a Southern Ocean Mesoscale Eddy. *Journal of Physical Oceanography*, 47(7):1737–1753.

Arhan, M., Speich, S., Messager, C., Dencausse, G., Fine, R., and Boye, M. (2011). Anticyclonic and cyclonic eddies of subtropical origin in the subantarctic zone south of Africa. *Journal of Geophysical Research: Oceans*, 116(11).

Arrigo, K. R., van Dijken, G. L., and Bushinsky, S. (2008). Primary production in the Southern Ocean, 1997-2006. *Journal of Geophysical Research: Oceans*, 113(8).

Arrigo, K. R., Worthen, D. L., Schnell, A., and Lizotte, M. P. (1998). Primary production in Southern Ocean waters. *Journal of Geophysical Research*, 103:15587–15600.

Babu, K. N., Sharma, R., Agarwal, N., Agarwal, V. K., and Weller, R. A. (2004). Study of the mixed layer depth variations within the north Indian Ocean using a 1-D model. *Journal of Geophysical Research: Oceans*, 109(C8):n/a–n/a.

Bachman, S., Taylor, J., Adams, K., Hosegood, P., Bachman, S., Taylor, J., Adams, K., and Hosegood, P. (2017). Mesoscale and Submesoscale Effects on Mixed Layer Depth in the Southern Ocean. *Journal of Physical Oceanography*, pages JPO–D–17–0034.1.

Baird, M. E. and Ridgway, K. R. (2012). The southward transport of sub-mesoscale lenses of Bass Strait Water in the centre of anti-cyclonic mesoscale eddies. *Geophysical Research Letters*, 39(2).

Banks, H. T., Wood, R. A., and Gregory, J. M. (2002). Changes to Indian Ocean subantarctic mode water in a coupled climate model as CO2 forcing increases. *Journal of Physical Oceanography*, 32(2000):2816–2827.

Belcher, S. E., Grant, A. L. M., Hanley, K. E., Fox-Kemper, B., Van Roekel, L., Sullivan, P. P., Large, W. G., Brown, A., Hines, A., Calvert, D., Rutgersson, A., Pettersson, H., Bidlot, J.-R., Janssen, P. A. E. M., and

Polton, J. A. (2012). A global perspective on Langmuir turbulence in the ocean surface boundary layer. *Geophys. Res. Lett.*, 39:L18605.

Berrisford, P., Dick, D., Paul, P., Roger, B., Keith, F., Manuel, F., Per, K., Shinya, K., Sakari, U., and Adrian, S. (2011). The ERA-Interim archive Version 2.0.

Boccaletti, G., Ferrari, R., and Fox-Kemper, B. (2007). Mixed layer instabilities and restratification. *Journal of Physical Oceanography*, 37:2228–2250.

Brainerd, K. E. and Gregg, M. C. (1995). Surface mixed and mixing layer depths. *Deep-Sea Research Part I*, 42(9):1521–1543.

Brannigan, L., Marshall, D. P., Naveira-Garabato, A., and George Nurser, A. J. (2015). The seasonal cycle of submesoscale flows. *Ocean Modelling*, 92:69–84.

Buckingham, C. E., Naveira Garabato, A. C., Thompson, A. F., Brannigan, L., Lazar, A., Marshall, D. P., George Nurser, A. J., Damerell, G., Heywood, K. J., and Belcher, S. E. (2016). Seasonality of submesoscale flows in the ocean surface boundary layer. *Geophysical Research Letters*, 43(5):2118–2126.

Callies, J., Ferrari, R., Klymak, J. M., and Gula, J. (2015). Seasonality in submesoscale turbulence. *Nature Communications*, 6.

Capet, X., Campos, E. J., and Paiva, A. M. (2008a). Submesoscale activity over the Argentinian shelf. *Geophysical Research Letters*, 35(15).

Capet, X., McWilliams, J. C., Molemaker, M. J., and Shchepetkin, a. F. (2008b). Mesoscale to Submesoscale Transition in the California Current System. Part I: Flow Structure, Eddy Flux, and Observational Tests. *Journal of Physical Oceanography*, 38(1):29–43.

Carranza, M. M. and Gille, S. T. (2015). Southern Ocean wind-driven entrainment enhances satellite chlorophyll-a through the summer. *Journal of Geophysical Research: Oceans*, 120(1):304–323.

Caulet, C., Swart, S., and Rouault, M. (2015). *Comparison of in-situ heat flux measurements with satellite re-analysis products of the Southern Ocean*. PhD thesis, University of Cape Tow.

Chelton, D. B., DeSzoeke, R. A., Schlax, M. G., El Naggar, K., and Siwertz, N. (1998). Geographical Variability of the First Baroclinic Rossby Radius of Deformation. *Journal of Physical Oceanography*, 28(3):433–460.

Cunningham, S. a., Alderson, S. G., King, B. a., and Brandon, M. a. (2003). Transport and variability of the Antarctic Circumpolar Current in Drake Passage. *Journal of Geophysical Research*, 108(C5):1–17.

D'Asaro, E., Lee, C., Rainville, L., Harcourt, R., and Thomas, L. (2011). Enhanced Turbulence and Energy Dissipation at Ocean Fronts. *Science*, 332(6027):318–322.

de Boyer Montégut, C., Madec, G., Fischer, A. S., Lazar, A., and Iudicone, D. (2004). Mixed layer depth over the global ocean: An examination of profile data and a profile-based climatology. *Journal of Geophysical Research C: Oceans*, 109(12):1–20.

Dencausse, G., Arhan, M., and Speich, S. (2011). Is there a continuous Subtropical Front south of Africa? *Journal of Geophysical Research: Oceans*, 116(2).

Domingues, R., Goni, G., Swart, S., and Dong, S. (2014). Wind forced variability of the Antarctic Circumpolar Current south of Africa between 1993 and 2010. *Journal of Geophysical Research: Oceans*, 119:1123–1145.

Dong, S., Gille, S. T., and Sprintall, J. (2007). An assessment of the Southern Ocean mixed layer heat budget. *Journal of Climate*, 20(17):4425–4442.

Dong, S., Sprintall, J., Gille, S. T., and Talley, L. (2008). Southern ocean mixed-layer depth from Argo float profiles. *Journal of Geophysical Research: Oceans*, 113(6):1–12.

du Plessis, M., Swart, S., Ansorge, I., and Mahadevan, A. (2017). Submesoscale processes promote seasonal restratification in the Subantarctic Ocean. *Journal of Geophysical Research-Oceans*, 122(4):2960–2975.

Dufour, C. O., Griffies, S. M., de Souza, G. F., Frenger, I., Morrison, A. K., Palter, J. B., Sarmiento, J. L., Galbraith, E. D., Dunne, J. P., Anderson, W. G., and Slater, R. D. (2015). Role of Mesoscale Eddies in Cross-Frontal Transport of Heat and Biogeochemical Tracers in the Southern Ocean. *Journal of Physical Oceanography*, 45(12):3057–3081.

Eady, E. (1949). Long waves and cyclone waves. *Tellus*, 1(3):33–52.

Erickson, Z. K., Thompson, A. F., Cassar, N., Sprintall, J., and Mazloff, M. R. (2016). An advective mechanism for deep chlorophyll maxima formation in southern Drake Passage. *Geophysical Research Letters*, 43(20):10,846–10,855.

Eriksen, C. C., Osse, T. J., Light, R. D., Wen, T., Lehman, T. W., Sabin, P. L., Ballard, J. W., and Chiodi, A. M. (2001). Seaglider: A long-range autonomous underwater vehicle for oceanographic research. *IEEE Journal of Oceanic Engineering*, 26(4):424–436.

Ertel, H. (1942). "Ein neuer hydrodynamischer Wirbelsatz. *Meteorol. Z.*, 59:277–281.

Faure, V., Arhan, M., Speich, S., and Gladyshev, S. (2011). Heat budget of the surface mixed layer south of Africa. *Ocean Dynamics*, 61(10):1441–1458.

Ferrari, R. (2011). A frontal challenge for climate models.

Forryan, A., Naveira Garabato, A. C., Polzin, K. L., and Waterman, S. (2015). Rapid injection of near-inertial shear into the stratified upper ocean at an Antarctic Circumpolar Current front. *Geophysical Research Letters*, 42(9):3431–3441.

Fox-Kemper, B., Danabasoglu, G., Ferrari, R., Griffies, S. M., Hallberg, R. W., Holland, M. M., Maltrud, M. E., Peacock, S., and Samuels, B. L. (2011). Parameterization of mixed layer eddies. III: Implementation and impact in global ocean climate simulations. *Ocean Modelling*, 39(1-2):61–78.

Fox-Kemper, B., Ferrari, R., Hallberg, R., Fox-Kemper, B., Ferrari, R., and Hallberg, R. (2008). Parameterization of Mixed Layer Eddies. Part I: Theory and Diagnosis. *Journal of Physical Oceanography*, 38(6):1145–1165.

Gille, S. T. (1994). Mean sea surface height of the Antarctic Circumpolar Current from Geosat data: Method and application. *Journal of Geophysical Research*, 99(C9):18255.

Gillett, N. P., Kell, T. D., and Jones, P. D. (2006). Regional climate impacts of the Southern Annular Mode. *Geophysical Research Letters*, 33(23).

Haine, T. W. N. and Marshall, J. (1998). Gravitational, Symmetric, and Baroclinic Instability of the Ocean Mixed Layer. *Journal of Physical Oceanography*, 28(4):634–658.

Hamlington, P. E., Van Roekel, L. P., Fox-Kemper, B., Julien, K., and Chini, G. P. (2014). Langmuir–Submesoscale Interactions: Descriptive Analysis of Multiscale Frontal Spindown Simulations. *Journal of Physical Oceanography*, 44(9):2249–2272.

Hanawa, K. and Talley, L. D. (2001). Mode waters. *Ocean Circulation and Climate: Observing and Modeling the Global Ocean*, pages 373–386 (736pp).

Haumann, A. F., Gruber, N., Münnich, M., Frenger, I., and Kern, S. (2016). Sea-ice transport driving Southern Ocean salinity and its recent trends. *Nature*, 537(7618):89–92.

Hendon, H. H., Lim, E. P., and Nguyen, H. (2014). Seasonal variations of subtropical precipitation associated with the southern annular mode. *Journal of Climate*, 27(9):3446–3460.

Hogg, A. M., Meredith, M., Blundell, J. R., and Wilson, C. (2008). Eddy heat flux in the Southern Ocean: response to variable wind forcing. *Journal of Climate*, 21(2006):608–620.

Hosegood, P. J., Gregg, M. C., and Alford, M. H. (2008). Restratification of the Surface Mixed Layer with Submesoscale Lateral Density Gradients: Diagnosing the Importance of the Horizontal Dimension. *Journal of Physical Oceanography*, 38:2438–2460.

Hoskins, B. J. (1974). The role of potential vorticity in symmetric stability and instability. *Quarterly Journal of the Royal Meteorological Society*, 100(425):480–482.

Hoskins, B. J. and Bretherton, F. P. (1972). Atmospheric Frontogenesis Models: Mathematical Formulation and Solution. *Journal of the Atmospheric Sciences*, 29(1):11–37.

Khatiwala, S., Primeau, F., and Hall, T. (2009). Reconstruction of the history of anthropogenic CO2 concentrations in the ocean. *Nature*, 462(7271):346–349.

Krug, M., Swart, S., and Gula, J. (2017). Submesoscale cyclones in the Agulhas current. *Geophysical Research Letters*, 44(1):346–354.

Langlais, C. E., Rintoul, S. R., and Zika, J. D. (2015). Sensitivity of Antarctic Circumpolar Current Transport and Eddy Activity to Wind Patterns in the Southern Ocean*. *Journal of Physical Oceanography*, 45(4):1051–1067.

Lapeyre, G. and Klein, P. (2006). Dynamics of the Upper Oceanic Layers in Terms of Surface Quasigeostrophy Theory. *Journal of Physical Oceanography*, 36(2):165–176.

Lapeyre, G., Klein, P., and Hua, B. L. (2006). Oceanic Restratification Forced by Surface Frontogenesis. *Journal of Physical Oceanography*, 36(8):1577–1590.

Large, W. G. and Pond, S. (1981). Open Ocean Momentum Flux Measurements in Moderate to Strong Winds. *Journal of Physical Oceanography*, 11(3):324–336.

Le Quéré, C., Andrew, R. M., Canadell, J. G., Sitch, S., Ivar Korsbakken, J., Peters, G. P., Manning, A. C., Boden, T. A., Tans, P. P., Houghton, R. A., Keeling, R. F., Alin, S., Andrews, O. D., Anthoni, P., Barbero, L., Bopp, L., Chevallier, F., Chini, L. P., Ciais, P., Currie, K., Delire, C., Doney, S. C., Friedlingstein, P., Gkritzalis, T., Harris, I., Hauck, J., Haverd, V., Hoppema, M., Klein Goldewijk, K., Jain, A. K., Kato, E., Körtzinger, A., Landschützer, P., Lefèvre, N., Lenton, A., Lienert, S., Lombardozzi, D., Melton, J. R., Metzl, N., Millero, F., Monteiro, P. M., Munro, D. R., Nabel, J. E., Nakaoka, S. I., O'Brien, K., Olsen, A., Omar, A. M., Ono, T., Pierrot, D., Poulter, B., Rödenbeck, C., Salisbury, J., Schuster, U., Schwinger, J., Séférian, R., Skjelvan, I., Stocker, B. D., Sutton, A. J., Takahashi, T., Tian, H., Tilbrook, B., Van Der Laan-Luijkx, I. T., Van Der Werf, G. R., Viovy, N., Walker, A. P., Wiltshire, A. J., and Zaehle, S. (2016). Global Carbon Budget 2016. *Earth System Science Data*, 8(2):605–649.

Lévy, M., Ferrari, R., Franks, P. J., Martin, A. P., and Rivière, P. (2012). Bringing physics to life at the submesoscale. *Geophysical Research Letters*, 39(14).

Lévy, M., Klein, P., and Treguier, A.-M. (2001). Impact of sub-mesoscale physics on production and subduction of phytoplankton in an oligotrophic regime. *Journal of Marine Research*, 59(4):535–565.

Little, H., Vichi, M., Thomalla, S., and Swart, S. (2018). Spatial and temporal scales of chlorophyll variability using high-resolution glider data. *Journal of Marine Systems*, doi:10.101.

Madec, G. (2008). NEMO Ocean Engine. *Note from the School of Modeling, Pierre-Simon Laplace Institute (IPSL)*, 27:No. 1288–1619.

Madec, G., Delecluse, P., Imbard, M., and Levy, C. (1998). OPA 8.1 Ocean General Circulation Model Reference Manual. *Notes du Pôle de Modélisation, IPSL*, (11):97pp.

Mahadevan, A. (2016). The Impact of Submesoscale Physics on Primary Productivity of Plankton. *Annual Review of Marine Science*, 8(1):161–184.

Mahadevan, A., D'Asaro, E., Lee, C., and Perry, M. J. (2012). Eddy-Driven Stratification Initiates North Atlantic Spring Phytoplankton Blooms. *Science*, 337(6090):54–58.

Mahadevan, A., Tandon, A., and Ferrari, R. (2010). Rapid changes in mixed layer stratification driven by submesoscale instabilities and winds. *Journal of Geophysical Research: Oceans*, 115(3).

Marshall, J. and Speer, K. (2012). Closure of the meridional overturning circulation through Southern Ocean upwelling.

Martin, J. P., Lee, C. M., Eriksen, C. C., Ladd, C., and Kachel, N. B. (2009). Glider observations of kinematics in a Gulf of Alaska eddy. *Journal of Geophysical Research: Oceans*, 114(12).

McCartney, M. S. (1977). Subantarctic Mode Water.

McWilliams, J. C. (2016). Submesoscale currents in the ocean. *Proceedings of the Royal Society A: Mathematical, Physical and Engineering Science*, 472(2189):20160117.

McWilliams, J. C. and Fox-Kemper, B. (2013). Oceanic wave-balanced surface fronts and filaments. *Journal of Fluid Mechanics*, 730:464–490.

Mensa, J. A., Garraffo, Z., Griffa, A., Özgökmen, T. M., Haza, A., and Veneziani, M. (2013). Seasonality of the submesoscale dynamics in the Gulf Stream region. *Ocean Dynamics*, 63(8):923–941.

Meredith, M. P. and Hogg, A. M. (2006). Circumpolar response of Southern Ocean eddy activity to a change in the Southern Annular Mode. *Geophysical Research Letters*, 33(16).

Miles, T., Lee, S. H., Wåhlin, A., Ha, H. K., Kim, T. W., Assmann, K. M., and Schofield, O. (2016). Glider observations of the Dotson Ice Shelf outflow. *Deep-Sea Research Part II: Topical Studies in Oceanography*, 123:16–29.

Molemaker, M. J., McWilliams, J. C., and Capet, X. (2010). Balanced and unbalanced routes to dissipation in an equilibrated Eady flow. *Journal of Fluid Mechanics*, 654:35–63.

Molemaker, M. J., McWilliams, J. C., and Yavneh, I. (2005). Baroclinic Instability and Loss of Balance. *Journal of Physical Oceanography*, 35(9):1505–1517.

Monteiro, P. M. S., Boyd, P., and Bellerby, R. (2011). Role of the seasonal cycle in coupling climate and carbon cycling in the Subantarctic Zone. In *Eos*, volume 92, pages 235–236.

Monteiro, P. M. S., Gregor, L., Lévy, M., Maenner, S., Sabine, C. L., and Swart, S. (2015). Intraseasonal variability linked to sampling alias in air-sea CO2 fluxes in the Southern Ocean. *Geophysical Research Letters*, 42(20):8507–8514.

Munk, W., Armi, L., Fischer, K., and Zachariasen, F. (2000). Spirals on the sea. *Proceedings of the Royal Society A: Mathematical, Physical and Engineering Sciences*, 456(1997):1217–1280.

Naveira Garabato, A. C., Polzin, K. L., King, B. A., Heywood, K. J., and Visbeck, M. (2004). Widespread Intense Turbulent Mixing in the Southern Ocean. *Science*, 303(5655):210–213.

Nicholson, S. A., Lévy, M., Llort, J., Swart, S., and Monteiro, P. M. S. (2016). Investigation into the impact of storms on sustaining summer primary productivity in the Sub-Antarctic Ocean. *Geophysical Research Letters*, 43(17):9192–9199.

Niiler, P. and Kraus, E. (1977). One-dimensional models of the upper-ocean. *Modeling and prediction of the upper layers of the ocean*, pages 143–172.

Nikurashin, M., Vallis, G. K., and Adcroft, A. (2012). Routes to energy dissipation for geostrophic flows in the Southern Ocean. *Nature Geoscience*, 6(1):48–51.

Oort, A. H., Anderson, L. A., and Peixoto, J. P. (1994). Estimates of the energy cycle of the oceans. *Journal of Geophysical Research*, 99(C4):7665–7688.

Orsi, A. H., Whitworth, T., and Nowlin, W. D. (1995). On the meridional extent and fronts of the Antarctic Circumpolar Current. *Deep Sea Research Part I: Oceanographic Research Papers*, 42(5):641–673.

Paulson, C. A. and Simpson, J. J. (1977). Irradiance Measurements in the Upper Ocean. *Journal of Physical Oceanography*, 7(6):952–956.

Pelland, N. A., Eriksen, C. C., and Lee, C. M. (2013). Subthermocline Eddies over the Washington Continental Slope as Observed by Seagliders, 2003–09. *Journal of Physical Oceanography*, 43(10):2025–2053.

Price, J. F., Mooers, C. N. K., and Van Leer, J. C. (1978). Observation and Simulation of Storm-Induced Mixed-Layer Deepening.

Price, J. F., Weller, R. A., and Pinkel, R. (1986). Diurnal cycling: Observations and models of the upper ocean response to diurnal heating, cooling, and wind mixing. *Journal of Geophysical Research*, 91(C7):8411.

Qiu, B., Chen, S., Klein, P., Sasaki, H., and Sasai, Y. (2014). Seasonal Mesoscale and Submesoscale Eddy Variability along the North Pacific Subtropical Countercurrent. *Journal of Physical Oceanography*, 44(12):3079–3098.

Rienecker, M. M., Suarez, M. J., Gelaro, R., Todling, R., Bacmeister, J., Liu, E., Bosilovich, M. G., Schubert, S. D., Takacs, L., Kim, G. K., Bloom, S., Chen, J., Collins, D., Conaty, A., Da Silva, A., Gu, W., Joiner, J., Koster, R. D., Lucchesi, R., Molod, A., Owens, T., Pawson, S., Pegion, P., Redder, C. R., Reichle, R., Robertson, F. R., Ruddick, A. G., Sienkiewicz, M., and Woollen, J. (2011). MERRA: NASA's modern-era retrospective analysis for research and applications. *Journal of Climate*, 24(14):3624–3648.

Rintoul, S., Hughes, C., and Olbers, D. (2001). *The Antarctic Circumpolar Current System*.

Rintoul, S. R. and England, M. H. (2002). Ekman Transport Dominates Local Air–Sea Fluxes in Driving Variability of Subantarctic Mode Water. *Journal of Physical Oceanography*, 32(5):1308–1321.

Rintoul, S. R. and Trull, T. (2001). Seasonal evolution of the mixed layer in the Subantarctic Zone south of Australia. *Journal of Geophysical Research, [Oceans]*, 106(C12):31447–31462.

Rocha, C. B., Chereskin, T. K., Gille, S. T., and Menemenlis, D. (2016). Mesoscale to Submesoscale Wavenumber Spectra in Drake Passage. *Journal of Physical Oceanography*, 46(2):601–620.

Rosso, I., Hogg, A. M., Strutton, P. G., Kiss, A. E., Matear, R., Klocker, A., and van Sebille, E. (2014). Vertical transport in the ocean due to sub-mesoscale structures: Impacts in the Kerguelen region. *Ocean Modelling*, 80:10–23.

Rosso, I., Hogg, A. M. C., Kiss, A. E., and Gayen, B. (2015). Topographic influence on submesoscale dynamics in the Southern Ocean. *Geophysical Research Letters*, 42(4):1139–1147.

Roullet, G. and Klein, P. (2010). Cyclone-anticyclone asymmetry in geophysical turbulence. *Physical Review Letters*, 104(21).

Rudnick, D. L. (2001). On the skewness of vorticity in the upper ocean. *Geophysical Research Letters*, 28(10):2045–2048.

Rudnick, D. L. and Cole, S. T. (2011). On sampling the ocean using underwater gliders. *Journal of Geophysical Research: Oceans*, 116(8).

Ruiz, S., Renault, L., Garau, B., and Tintoré, J. (2012). Underwater glider observations and modeling of an abrupt mixing event in the upper ocean. *Geophysical Research Letters*, 39(1).

Sabine, C. L., Feely, R. A., Gruber, N., Key, R. M., Lee, K., Bullister, J. L., Wanninkhof, R., Wong, C. S., Wallace, D. W. R., Tilbrook, B., Millero, F. J., Peng, T.-H. T.-H., Kozyr, A., Ono, T., Rios, A. F., A., F. R., Gruber, N., Key, R. M., Lee, K., Bullister, J. L., Wanninkhof, R., Wong, C. S., Wallace, D. W. R., Tilbrook, B., Millero, F. J., Peng, T.-H. T.-H., Kozyr, A., Ono, T., and Rios, A. F. (2004). The oceanic sink for anthropogenic CO2. *Science*, 305(5682):367–371.

Sallée, J. B., Morrow, R., and Speer, K. (2008). Eddy heat diffusion and Subantarctic Mode Water formation. *Geophysical Research Letters*, 35(5).

Sallée, J. B., Shuckburgh, E., Bruneau, N., Meijers, A. J. S., Bracegirdle, T. J., and Wang, Z. (2013a). Assessment of Southern Ocean mixed-layer depths in CMIP5 models: Historical bias and forcing response. *Journal of Geophysical Research: Oceans*, 118(4):1845–1862.

Sallée, J. B., Shuckburgh, E., Bruneau, N., Meijers, A. J. S., Bracegirdle, T. J., Wang, Z., and Roy, T. (2013b). Assessment of Southern Ocean water mass circulation and characteristics in CMIP5 models: Historical bias and forcing response. *Journal of Geophysical Research: Oceans*, 118(4):1830–1844.

Sallée, J.-B., Speer, K., Rintoul, S., and Wijffels, S. (2010a). Southern Ocean Thermocline Ventilation. *Journal of Physical Oceanography*, 40(3):509–529.

Sallée, J.-B., Speer, K. G., and Rintoul, S. R. (2010b). Zonally asymmetric response of the Southern Ocean mixed-layer depth to the Southern Annular Mode. *Nature Geoscience*, 3(4):273–279.

Sallée, J. B., Wienders, N., Speer, K., and Morrow, R. (2006). Formation of subantarctic mode water in the southeastern Indian Ocean. *Ocean Dynamics*, 56(5-6):525–542.

Sasaki, H., Klein, P., Qiu, B., and Sasai, Y. (2014). Impact of oceanic-scale interactions on the seasonal modulation of ocean dynamics by the atmosphere. *Nature Communications*, 5.

Schlitzer, R. (2002). Carbon export fluxes in the Southern Ocean: Results from inverse modeling and comparison with satellite-based estimates. *Deep-Sea Research Part II: Topical Studies in Oceanography*, 49(9-10):1623–1644.

Schmidt, K. M., Swart, S., Reason, C., and Nicholson, S. A. (2017). Evaluation of satellite and reanalysis wind products with in situ wave glider wind observations in the southern ocean. *Journal of Atmospheric and Oceanic Technology*, 34(12):2551–2568.

Schmidtko, S., Johnson, G. C., and Lyman, J. M. (2013). MIMOC: A global monthly isopycnal upper-ocean climatology with mixed layers. *Journal of Geophysical Research: Oceans*, 118(4):1658–1672.

Schofield, O., Ducklow, H. W., Martinson, D. G., Meredith, M. P., Moline, M. A., and Fraser, W. R. (2010). How do polar marine ecosystems respond to rapid climate change?

Schofield, O., Miles, T., Alderkamp, A.-C., Lee, S., Haskins, C., Rogalsky, E., Sipler, R., Sherrell, R. M., and Yager, P. L. (2015). In situ phytoplankton distributions in the Amundsen Sea Polynya measured by autonomous gliders. *Elementa: Science of the Anthropocene*, 3:000073.

Schulz, D. (2015). Synoptic Meteorology: Frontogenesis. In *Encyclopedia of Atmospheric Sciences (Second Edition)*, pages 353–358.

Scully-Power, P. (1986). Navy Oceanographer Shuttle observations. STS 41-G Mission Report. Naval Underwater Systems Center, NUSC Technical Document 7611. Technical report.

Shakespeare, C. J. and Taylor, J. R. (2013). A generalized mathematical model of geostrophic adjustment and frontogenesis: Uniform potential vorticity. *Journal of Fluid Mechanics*, 736:366–413.

Shcherbina, A. Y., D'Asaro, E. A., Lee, C. M., Klymak, J. M., Molemaker, M. J., and McWilliams, J. C. (2013). Statistics of vertical vorticity, divergence, and strain in a developed submesoscale turbulence field. *Geophysical Research Letters*, 40(17):4706–4711.

Sherman, J., Davis, R. E., Owens, W. B., and Valdes, J. (2001). The autonomous underwater glider "Spray". *IEEE Journal of Oceanic Engineering*, 26(4):437–446.

Sloyan, B. M. and Rintoul, S. R. (2001). The Southern Ocean Limb of the Global Deep Overturning Circulation*. *Journal of Physical Oceanography*, 31(1):143–173.

Sokolov, S. and Rintoul, S. R. (2007). Multiple Jets of the Antarctic Circumpolar Current South of Australia*. *Journal of Physical Oceanography*, 37(5):1394–1412.

Stammer, D. (1997). Global Characteristics of Ocean Variability Estimated from Regional TOPEX/POSEIDON Altimeter Measurements. *Journal of Physical Oceanography*, 27(8):1743–1769.

Stommel, H. (1989). The Slocum Mission. *Oceanography*, 2(1):22–25.

Stone, P. H. (1966). On Non-Geostrophic Baroclinic Stability.

Suzuki, N., Fox-Kemper, B., Hamlington, P. E., and Van Roekel, L. P. (2016). Surface waves affect frontogenesis. *Journal of Geophysical Research: Oceans*, 121(5):3597–3624.

Swart, S., Chang, N., Fauchereau, N., Joubert, W., Lucas, M., Mtshali, T., Roychoudhury, A., Tagliabue, A., Thomalla, S., Waldron, H., and Monteiro, P. M. (2012). Southern Ocean Seasonal Cycle Experiment 2012: Seasonal scale climate and carbon cycle links. *South African Journal of Science*, 108(3-4).

Swart, S. and Speich, S. (2010). An altimetry-based gravest empirical mode south of Africa: 2. Dynamic nature of the Antarctic circumpolar current fronts. *Journal of Geophysical Research: Oceans*, 115:1–22.

Swart, S., Speich, S., Ansorge, I. J., and Lutjeharms, J. R. E. (2010). An altimetry-based gravest empirical mode south of Africa: 1. Development and validation. *Journal of Geophysical Research*, 115(C3):C03002.

Swart, S., Thomalla, S., and Monteiro, P. (2015). The seasonal cycle of mixed layer dynamics and phytoplankton biomass in the Sub-Antarctic Zone: A high-resolution glider experiment. *Journal of Marine Systems*, 147:103–115.

Tagliabue, A., Sallée, J.-B., Bowie, A. R., Lévy, M., Swart, S., and Boyd, P. W. (2014). Surface-water iron supplies in the Southern Ocean sustained by deep winter mixing. *Nature Geoscience*, 7(March):314–320.

Taylor, J., Bachman, S., Stamper, M., Hosegood, P., Adams, K., Sallee, J.-B., and Torres, R. (2018). Submesoscale Rossby waves on the Antarctic circumpolar current. *Science Advances*, 4(3):1–8.

Taylor, J. R. and Ferrari, R. (2009). On the equilibration of a symmetrically unstable front via a secondary shear instability. *Journal of Fluid Mechanics*, 622:103.

Taylor, J. R. and Ferrari, R. (2010). Buoyancy and Wind-Driven Convection at Mixed Layer Density Fronts. *Journal of Physical Oceanography*, 40(6):1222–1242.

Taylor, J. R. and Ferrari, R. (2011). Shutdown of turbulent convection as a new criterion for the onset of spring phytoplankton blooms. *Limnology and Oceanography*, 56(6):2293–2307.

Thomalla, S. J., Fauchereau, N., Swart, S., and Monteiro, P. M. S. (2011). Regional scale characteristics of the seasonal cycle of chlorophyll in the Southern Ocean. *Biogeosciences*, 8(10):2849–2866.

Thomalla, S. J., Racault, M. F., Swart, S., and Monteiro, P. M. (2015). High-resolution view of the spring bloom initiation and net community production in the Subantarctic Southern Ocean using glider data. *ICES Journal of Marine Science*, 72(6):1999–2020.

Thomas, L. and Ferrari, R. (2008). Friction, Frontogenesis, and the Stratification of the Surface Mixed Layer. *Journal of Physical Oceanography*, 38(11):2501–2518.

Thomas, L. N. (2005). Destruction of Potential Vorticity by Winds. *Journal of Physical Oceanography*, 35(1994):2457–2466.

Thomas, L. N. and Lee, C. M. (2005). Intensification of Ocean Fronts by Down-Front Winds. *Bulletin of the American Meteorological Society*, 86(6):783.

Thomas, L. N., Tandon, A., and Mahadevan, A. (2008). Submesoscale processes and dynamics. In *Geophysical Monograph Series*, volume 177, pages 17–38.

Thomas, L. N. and Taylor, J. R. (2010). Reduction of the usable wind-work on the general circulation by forced symmetric instability. *Geophysical Research Letters*, 37(18).

Thomas, L. N., Taylor, J. R., D'Asaro, E. A., Lee, C. M., Klymak, J. M., Shcherbina, A., Thomas, L. N., Taylor, J. R., D'Asaro, E. A., Lee, C. M., Klymak, J. M., and Shcherbina, A. (2015). Symmetric Instability, Inertial Oscillations, and Turbulence at the Gulf Stream Front. *http://dx.doi.org/10.1175/JPO-D-15-0008.1*, pages 197–218.

Thomas, L. N., Taylor, J. R., Ferrari, R., and Joyce, T. M. (2013). Symmetric instability in the Gulf Stream. *Deep-Sea Research Part II: Topical Studies in Oceanography*, 91:96–110.

Thompson, A. F., Heywood, K. J., Schmidtko, S., and Stewart, A. L. (2014). Eddy transport as a key component of the Antarctic overturning circulation. *Nature Geoscience*, 7(12):879–884.

Thompson, A. F., Lazar, A., Buckingham, C., Naveira Garabato, A. C., Damerell, G. M., and Heywood, K. J. (2016). Open-ocean submesoscale motions: A full seasonal cycle of mixed layer instabilities from gliders. *Journal of Physical Oceanography*, 46(4):1285–1307.

Thomsen, S., Kanzow, T., Krahmann, G., Greatbatch, R. J., Dengler, M., and Lavik, G. (2016). The formation of a subsurface anticyclonic eddy in the Peru-Chile Undercurrent and its impact on the near-coastal salinity, oxygen, and nutrient distributions. *Journal of Geophysical Research: Oceans*, 121(1):476–501.

Thomson, J., Girton, J. B., Jha, R., and Trapani, A. (2018). Measurements of directional wave spectra and wind stress from a Wave Glider autonomous surface vehicle. *Journal of Atmospheric and Oceanic Technology*, 35(2):347–363.

Todd, R. E., Owens, W. B., and Rudnick, D. L. (2016). Potential Vorticity Structure in the North Atlantic Western Boundary Current from Underwater Glider Observations. *Journal of Physical Oceanography*, 46(1):327–348.

Todd, R. E., Rudnick, D. L., and Davis, R. E. (2009). Monitoring the greater San Pedro Bay region using autonomous underwater gliders during fall of 2006. *Journal of Geophysical Research*, 114(C6):C06001.

Trenberth, K. E. (1991). Storm tracks in the Southern Hemisphere.

Viglione, G. A., Thompson, A. F., Flexas, M. M., Sprintall, J., and Swart, S. (2018). Abrupt transitions in submesoscale structure in Southern Drake Passage: Glider observations and model results. *Journal of Physical Oceanography*, pages JPO–D–17–0192.1.

Waniek, J. J. (2003). The role of physical forcing in initiation of spring blooms in the northeast Atlantic. *Journal of Marine Systems*, 39(1-2):57–82.

Webb, D. C., Simonetti, P. J., and Jones, C. P. (2001). SLOCUM: An underwater glider propelled by environmental energy. *IEEE Journal of Oceanic Engineering*, 26(4):447–452.

Whitt, D. B. and Taylor, J. R. (2017). Energetic Submesoscales Maintain Strong Mixed Layer Stratification during an Autumn Storm. *Journal of Physical Oceanography*, 47(10):2419–2427.

Wunsch, C. (1998). The Work Done by the Wind on the Oceanic General Circulation. *Journal of Physical Oceanography*, 28(11):2332–2340.

Yuan, X., Patoux, J., and Li, C. (2009). Satellite-based midlatitude cyclone statistics over the Southern Ocean: 2. Tracks and surface fluxes. *Journal of Geophysical Research Atmospheres*, 114(4).